MULTI-PHOTON EXCITATION AND RELAXATION IN COLLOIDAL SEMICONDUCTOR QUANTUM DOTS

QU YINGLI

NATIONAL UNIVERSITY OF SINGAPORE

2009

MULTI-PHOTON EXCITATION AND RELAXATION IN COLLOIDAL SEMICONDUCTOR QUANTUM DOTS

QU YINGLI

(M. Eng. Shanghai Institute of Technical Physics,

Chinese Academy of Sciences)

A THESIS SUBMITTED

FOR THE DEGREE OF PHILOSOPHY

DEPARTMENT OF PHYSICS

NATIONAL UNIVERSITY OF SINGAPORE

2009

ACKNOWLEDGEMENTS

Firstly, I would like to express my deepest gratitude to my supervisor, Prof. Ji Wei, for his dedicated supervisions, patient guidance and valuable suggestions throughout my research project. At the same time, I would like to thank the National University of Singapore for awarding me a research scholarship so that I had the opportunity to complete my research.

Secondly, I would like to give my special thanks to my various colleagues: Dr. Zheng Yuangang in IBN, Mr. Mi Jun, Dr. He Jun, Dr. Hendry Izaac Elim, Mr. Xing Guichuan, Dr. Gu Bing, Mr. Mohan Singh Dhoni, Mr. Yang Hongzhi, and other group members for their kind helps and friendships during my stay in the Femtosecond Laser Spectroscopy Lab. I would also appreciate very much for kind helps and supports from the lab officers Mr. Wu Tong Meng Samuel and Mr. Foong Chee Kong during the years. Furthermore, I would like to express my thanks to Dr. Zhu Yanwu, Dr. Fan Haiming and Ms Yong Zhihua for their help and discussions.

Finally, I would like to thank my husband Hu Guojun, my parents, my parents-in-law, my sisters and brother as well as my son for their support, patience, encouragement, understanding and sacrifice during my PhD study.

CONTENTS

SUMMARY

Colloidal semiconductor quantum dots (QDs) have received increasing attention as promising two-photon absorbers for optical applications such as bio-imaging, optical limiting, stabilization, optical communication, optical information. As far as these applications are concerned, two-photon absorption (TPA) cross-sections as well as subsequent recombination processes following interband excitation are important aspects. In this thesis, we report the systematic experimental study on the TPA excitation and relaxation in colloidal CdSe QDs and CdTe QDs. Theoretical work has also been carried out to investigate the TPA spectra in strong confinement CdTe QDs.

For the experimental study, various techniques have been applied to investigate the characteristics of the above nanomaterials such as high-resolution transmission electron microscopy (HRTEM), UV-visible absorption spectroscopy, photoluminescence (PL) spectroscopy, etc. For the study of TPA in QDs, open-aperture Z-scans have been performed at different wavelengths with femtosecond laser pulses. The relaxation processes have been determined by time-resolved, frequency-degenerate pump-probe technique.

For the theoretical calculation, a TPA theory for QDs based on eight-band Pidgen and Brown (PB) model has been developed. Numerical calculations based on the theory have been performed to investigate the spectra of TPA in strong confinement CdTe QDs.

For colloidal CdSe QDs with 2 nm in radius, the TPA spectra have been measured with Z-scan from 750 nm to 950 nm and compared with published calculation results. The Auger process as well as intraband absorption, after TPA excitation, have been analyzed with frequency-degenerate, pump-probe technique and open-aperture Z-scan technique, respectively. For TPA spectra, the measured cross section is in the range from 10^{-47} to 10^{-46} cm^4s photon^{-1}, depending on the wavelength. These values are in the same range as the published computation result based on a simple four-band parabolic model. The Auger constant is revealed to be of the order of $\sim 10^{-30} cm^6 s^{-1}$, while the intraband absorption cross-sections are found to be in the range from 10^{-18} to 10^{-17} cm^2 from 680 to 780 nm. Our experimental evidence demonstrates that the Auger recombination or the intraband absorption takes place under the condition that the average electron-hole pair per quantum dot is greater than unity.

For the study on colloidal CdTe QDs, TPA spectra of three-different-sized QDs in very strong confinement regime have been investigated both experimentally and theoretically. The size-dependent TPA cross-section is unambiguously measured from 720 to 950 nm with Z-scan technique. the TPA cross-sections are measured to be on the order from 10^{-47} to 10^{-46} $cm^4 \cdot s \cdot photon^{-1}$, depending on the wavelength and the size of CdTe QDs. Based on the eight band PB model, calculation on the spectra of TPA in CdTe QDs has also been carried out. By taking into account of the conduction-valence band mixing and the complex structures of the valence bands, the theory can give more accurate prediction for TPA of CdTe QDs in the strong confinement regime. Both the

experiment and theory show that at a certain wavelength, the TPA in QDs rises un-monotonously with size. The increase of TPA for larger size is due to two factors: the increasing number of transitions for larger size and the red shift of the transitions of larger size. Another findings from the theory work is that, though the maximum peaks increases for larger size, the normalized maximum values of TPA by the QDs volume does not show size dependence.

The studies presented in this thesis will provide first-hand information for many applications based on two-photon absorption of QDs in strong confinement.

LIST OF FIGURES/TABLE

FIGURES

TABLE

LIST OF PUBLICAITONS

I. PUBLICATIONS ON INTERNATIONAL JOURNAL (in reverse chronological order)

1. **Y.L. Qu** and W. Ji,
   "Two-Photon Absorption of Quantum Dots in the Regime of Very Strong Confinement: Size and Wavelength Dependence",
   J. Opt. Soc. Am. B 26, 1897 (2009).

2. J. He, G. D. Scholes, **Y.L. Qu,** and W. Ji,
   "Upconversion photoluminescence of CdS nanocrystals in polymeric film",
   J. Appl. Phys. 104, 023110 (2008).

3. **Y.L. Qu**, W. Ji, Y.G. Zheng, and J. Y. Ying,
   "Auger Recombination and Intraband Absorption of Two-Photon-Excited Carriers in Colloidal CdSe Quantum Dots",
   App. Phys. Lett. 90, 133112 (2007).

4. P.H. Li, **Y.L. Qu,** X.J. Xu, Y.W. Zhu, T. Yu, K.C. Chin, J. Mi, X.Y. Gao, C.T. Lim, Z.X. Shen, A.T.S. Wee, W. Ji, and C.H. Sow,
   "Synthesis of "cactus" top-decorated aligned carbon nanotubes and their third-order nonlinear optical properties",
   JOURNAL OF NANOSCIENCE AND NANOTECHNOLOGY 6, 990 (2006).

5. J. He, **Y.L. Qu**, H.P. Li, J. Mi, and W. Ji,

   "Three-photon absorption in ZnO and ZnS crystals",

   OPTICS EXPRESS 13, 9235 (2005).

II. PAPERS PRESENTED AT INTERNATIONAL CONFERNECES (in reverse chronological order)

1. **Y.L. Qu** and W. Ji,

   "Two-Photon Absorption at Communication Wavelength and Auger Relaxation in Colloidal InGaP/ZnS Quantum Dots",

   ICMAT 2007, July 2007, Singapore.

2. **Y.L. Qu**, W. Ji, Yuangang Zheng, and Jackie Y. Ying,

   "Three-photon absorption in ZnO quantum dots",

   ICMAT 2005, July 2005, Singapore.

Chapter I

INTRODUCTION

1.1 Background

Nano-scale semiconductor materials have been investigated intensely over the past several decades as “molecular electronics” which incorporate the molecular-like behavior into semiconductor materials. Bulk lattice structure is conserved in these nano-scale materials. However, the spatial confinement makes the carrier movement quantized known as “quantum size effect”. The quantum size effect makes the electronic and optical properties of nano-scale materials tunable through changing in the size, shape, surface, among others. This new era of research on semiconducting materials started in 1974 when the first two dimensional structures (quantum wells) were created at AT & T Bell Laboratories [1.1] and IBM [1.2]. In a quantum well (QW) the electrons and holes are confined in a thin layer of a semiconductor material. The width of this layer is of the order of the bulk exciton Bohr radii, leading to quantized sub-bands. By the end of the1980s, the properties of the QWs were well understood, and research interest changed to lower dimensional structures such as quantum wire where the electrons and holes are confined in two dimensions [1.3]. A further reduction of dimensionality to quasi-zero dimensions was first achieved by a research group at Texas Instruments Inc., with the creation of quantum dots (QDs) by lithography [1.4]. The lateral

dimension of the QDs is 250 nm. In the last decade, QDs with dimensions of less than 10 nm have been successfully synthesized.

QDs represent a class of quasi-zero-dimensional object. The quantum size effect in QDs is the most dramatic compared with quantum-wells and quantum wires due to the complete confinement of charge carriers. QDs have been considered as promising candidates in many applications such as bio-imaging, identifying, optical switching, and lasing [1.5-1.18]. In these applications, the optical properties of QDs are the main concern and are critical to their performances.

In bio-imaging and bio-identifying, the fluorescent materials are dispersed into the internal structure of bio-samples. By exciting these fluorescent materials with laser beams, the image of the target internal structure can be obtained through photon-induced photoluminescence (PL) from the recombination of excited electrons and holes. A decade ago, organic dyes were widely accepted as ideal fluorescent materials. However, as the fabrication techniques of fluorescent QDs became mature, QDs have been found to be superior to traditional organic dyes, mainly due to following features: QDs are estimated to be 20 times brighter and 100 times more stable than traditional fluorescent organic dyes [1.19]; the emission wavelength of QDs is tunable; excitation wavelength is much wider and PL is much narrower, *etc*. These advantages of QDs over organic dyes make QDs very promising candidates in a large variety of fields.

In the excitation process, the number of photons needed for one transition depends on the band gap of the material as well as on the photon energy. Compared with one-photon absorption excitation, multi-photon absorption (MPA) excitation is preferred in order to have higher signal-to-noise ratio, deeper penetration depth as well as greater spatial resolution [1.20, 1.21].

In the MPA excitation of QDs, the MPA action cross-section is directly related to the brightness of the image. The MPA action cross-section is defined as the product of the fluorescence quantum efficiency and the MPA cross-section. The magnitude of the fluorescence quantum efficiency depends on many factors such as the passivation of QDs surfaces. Therefore there are some uncertainties in determining the real potential of the QDs. On the other hand, the MPA cross-section is an intrinsic parameter. The value of the MPA cross-section is related to the size, the structure and the materials involved in QDs. Thus, unambiguously determining the accurate value of MPA cross-section offers a direct guide in evaluating the real capacity of QDs for bio-imaging applications. Among the MPA excitation, two-photon absorption (TPA) is mostly applied in imaging due to both greater TPA value (compared to higher-order MPA) and availability of appropriate lasers.

As for the material of QDs, it has been widely accepted that QDs belonging to group II-VI are promising candidates in bioimaging due to the direct band gap and large Bohr exciton radius [1.13]. In this study, the TPA

spectra in CdSe and CdTe QDs as well as the size effect of TPA in CdTe QDs are studied, in particular, both experimentally and in theory. Furthermore, the relaxation of excited carriers in CdSe QDs following with two-photon excitation is scrutinized in detail.

In the following sections of Chapter 1, a general description will be made of the general properties of QDs as well as two-photon excitation and relaxation processes. A literature review will also be given on the published TPA studies in these two types of QDs followed by the objectives and scope of this thesis. In the final section of Chapter 1, the topics of this thesis are outlined.

1.2 General properties of quantum dots

As mentioned in the last section, semiconductor materials confined in one, two and three dimensions in the nano-scale are called quantum wells, quantum wires and quantum dots, respectively. In quantum wells and quantum wires, translational symmetry in two and one dimension respectively still exists and a statistically large number of electrons and holes can be created. However, for quantum dots, due to the totally confinement, the translational symmetry is broken in all directions, only a finite number of excitons can be created within one and the same dot. This difference between the QDs and quantum wells/wires can be explained from the differences of density of states (DOS). DOS plays an important role in the characterization of a physical system. It is

defined as the number of states of the system whose energies are in the range of E to $E + \delta E$. As can be seen from Fig. 1.1, though the DOS of the quantum wells and quantum wires have been quantized, a continuum part still exists which involves a large number of states in the range of E to $E + \delta E$. However, for QDs, the DOS is delta function just as in atoms. Only finite number of states exists for certain energy. Thus, QDs have a low optical density and could have gain saturation which makes it possible as mediums of lasers, memory devices and *etc*.

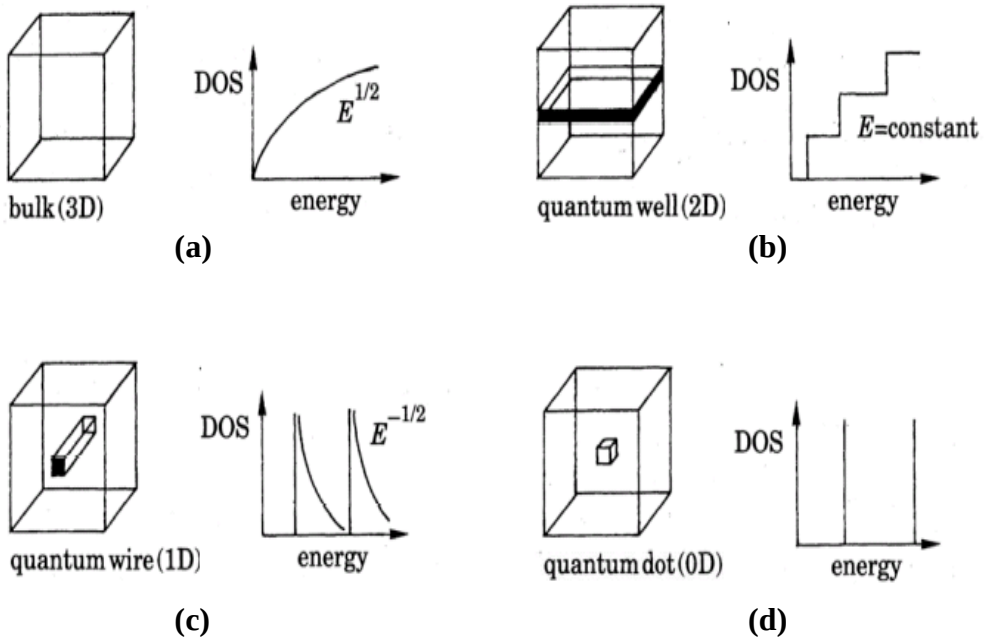

Fig. 1.1 Schematic image for the structure (left) and density of states (right) for (a) bulk semiconductor; (b) quantum well (c) quantum wire; (d) quantum dots.

Another important characteristic of QDs is that the discrete energy levels are tunable with tuning the size. As artificial, QDs exhibit many characteristics

resemble that of the atom: such as discrete energy levels, a limit number of exciton at certain energy level. Moreover, QDs have advantage of tunable electrical and optical properties through tuning the size. As shown in Fig. 1.2, as the size becomes smaller, the energy band-gap is going larger and the gap between the energy levels bigger. Thus the emission wavelength of QDs are tunable through tuning the size. As shown in Fig. 1.3, the fluorescence wavelength of QDs for the same material can be varied from red to blue by changing the sizes.

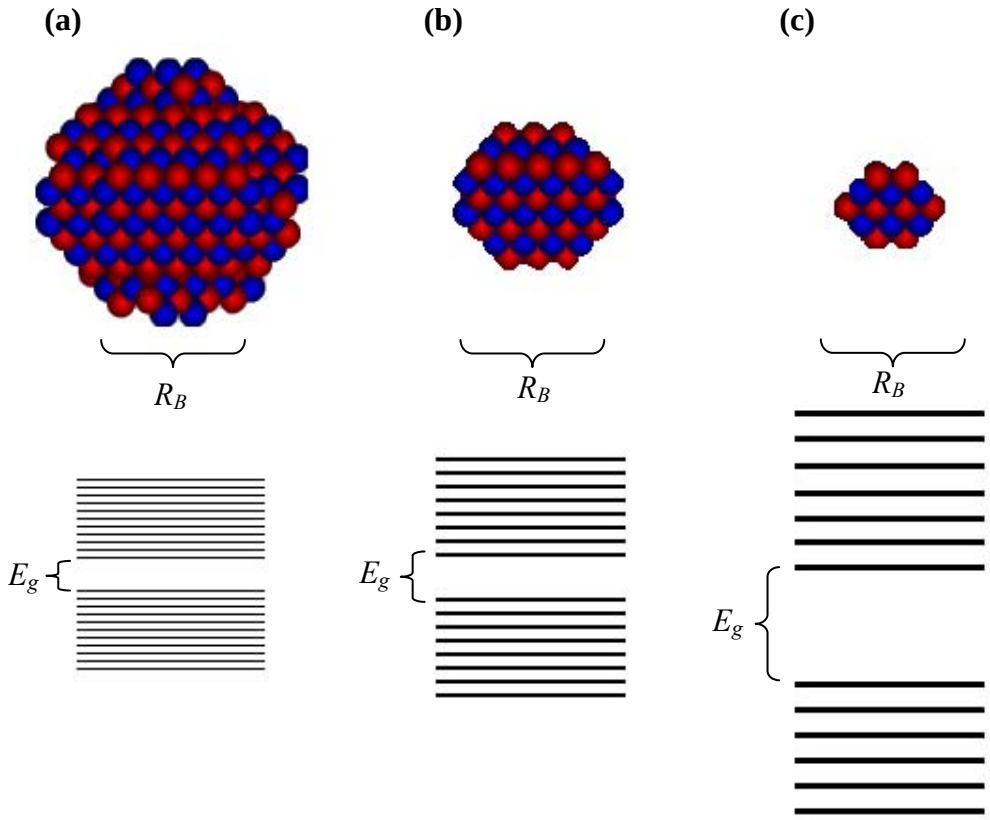

Fig. 1.2 Schematic diagram of the structure (upper) and the corresponding energy levels (below) of quantum dots for (a) weak confinement regime, (b) intermediate confinement regime, and (c) strong confinement regime.

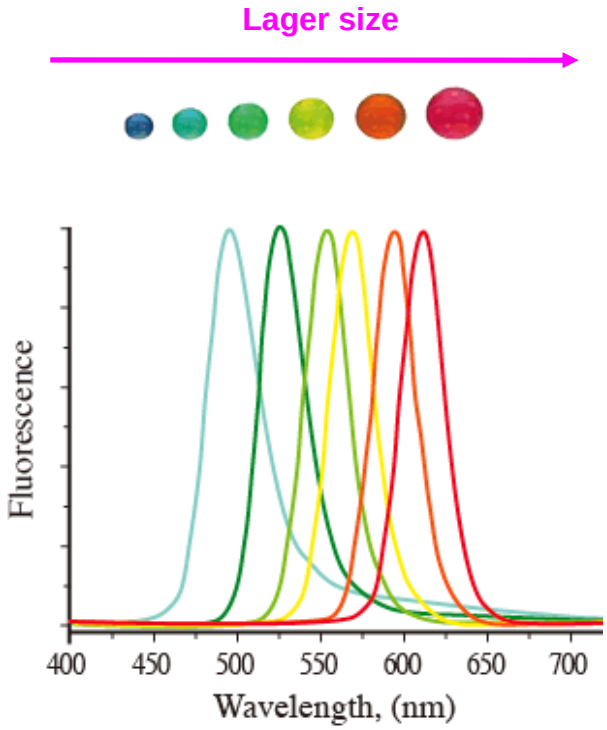

Fig. 1.3 Fluorescence of QDs with different size. The fluorescence peak is red shifted for larger size.

It has been shown by theoretical analysis that the optical properties of QDs are strongly dependent on the ratio of the nanocrystal radius, R, to the Bohr radius of the bulk exciton R_B, $R_B = \hbar^2 \kappa / \mu e^2$, where κ is the dielectric constant of the semiconductor and μ is the exciton reduced mass [1.22]. There are three different regimes defined by this ratio [1.23]: (1) the weak confinement regime: $R >> R_B$. In this regime, the confinement kinetic energy is smaller than the Coulomb interaction, the Coulomb interaction is more important than the quantization energies of the electrons; (2) the intermediate confinement regime: $R \sim R_B$. In this regime, the confinement energy is of the same order as the Coulomb interaction energy; and (3) strong confinement regime: $R << R_B$. In this regime both carriers (electrons and holes) are

independently confined, the Coulomb interaction is much smaller compared with the confinement energy.

In many applications, the QDs in the strong confinement regime are preferable. For example, in the applications of bio-imaging and bio-identifying, QDs in the strong confinement regime could provide a wider range of emission wavelengths with little changes in size. In addition, the QDs with diameter smaller than 5 nm can be easier in penetrating into cells and thus increase the labeling efficiency. In this thesis, the optical excitation and subsequent relaxation of carriers in QDs in the strong confinement regime are investigated with a total size smaller than 5 nm. This way, we hope to gain a comprehensive understanding for future applications in bio-imaging and bio-identifying.

1.3 Two-photon absorption (TPA) and relaxation

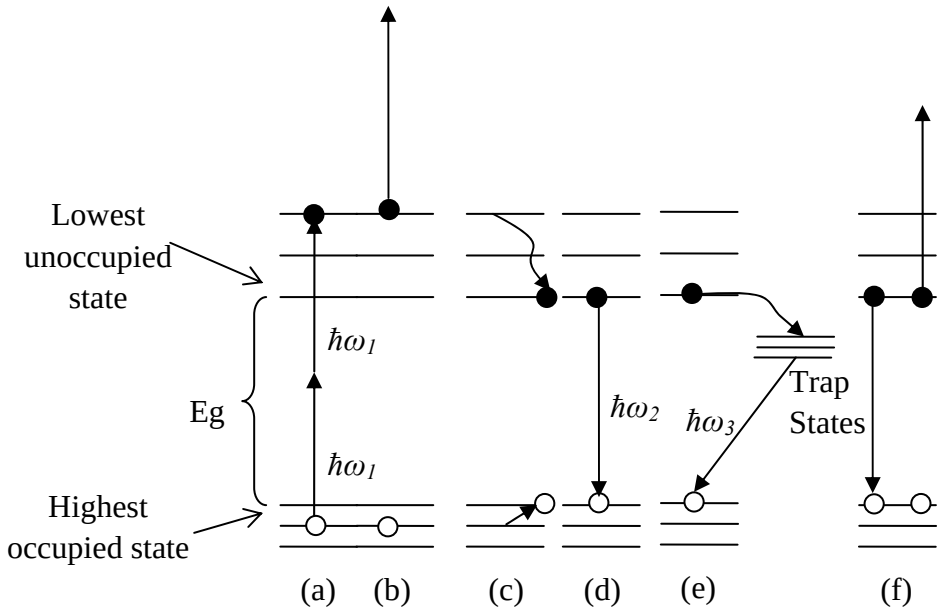

Fig. 1.4 Schematic diagram of two-photon excitation and possible relaxation pathways.

Two-photon absorption (TPA) is the simultaneously absorption of two photons with either identical or different frequencies, in order to excite a material from lower energy level to higher energy level. TPA is not an everyday phenomenon and is many orders of magnitude weaker than linear absorption. The strength of TPA depends on the square of the light intensity, thus it is a nonlinear optical process. The phenomenon was originally predicted by Maria Goeppert-Mayer in her doctoral dissertation in 1931 [1.24]. The first experimental verification came thirty years later, after the invention of the laser which permits the detection of two-photon-excited fluorescence in a europium-doped crystal [1.25]. In 1962, TPA was observed in vapor (cesium) by Isaac Abella [1.26].

TPA is a third-order nonlinear optical process. In particular, the imaginary part of the third-order nonlinear susceptibility $\chi^{(3)}$ is related to the TPA coefficient β through the following equation:

$$\mathrm{Im}\,\chi^{(3)} = \frac{n_0^2 \varepsilon_0 c^2}{\omega}\beta \tag{1.1}$$

As shown in Fig. 1.4 (a), upon the absorption of two photons, one electron-hole pair is generated. In this case, the total absorption coefficient α of the material is expressed as:

$$\alpha = \alpha_0 + \beta I \tag{1.2}$$

where α_0 is the linear absorption coefficient and *I* is the light intensity.

In the case of excitation light is very intense, the two-photon excited carrier may make further transition instantaneously with TPA to higher energy level by absorbing another incoming photon, as demonstrated in Fig. 1.4 (b). This process is called TPA-generated excited-state (or free-carrier) absorption. In this case, the total absorption coefficient α is written as:

$$\alpha = \alpha_0 + \beta I + \sigma_\alpha \Delta N \tag{1.3}$$

where σ_α is the excited-state cross section and ΔN is the density of TPA generated carriers, which is given by:

$$d\Delta N / dt = \beta I^2 / 2\hbar\omega - \Delta N / \tau \tag{1.4}$$

where, τ is the carrier recombination time. The second term at the right-hand of equation (1.4) is normally neglected since that the recombination time τ is much larger as compared with femtosecond excitation pulse.

After excitation, the excited electrons and holes relax to the respective lowest unoccupied and highest occupied states with the assistance of phonons and energy transfer between electrons and holes [1.27, 1.28], as shown in Fig. 1.4 (c). The time scale of this relaxation is determined by the energy structure of the material and is normally very fast in QDs on the femtosecond scale. The relaxed electron-hole pair then recombines through different pathways, as shown in Fig 1.4 (d) to Fig. 1.4 (f). In Fig 1.4 (d), when only electron-hole pair is generated, the energy released by the recombination emits a photon of a time scale of nanoseconds for many semiconductors.

On condition where there is a considerable amount of defects or interface states lying between the lowest unoccupied state (LUS) in the conduction band and highest occupied state (HOS) in the valence band, the excited electron-hole pair may have great chance being trapped by these states before they recombine, as shown in Fig.1.4 (e). (In order to shorten the writing, these states are termed as trap states in the rest of this thesis.)

The relaxation pathway becomes complex when more than one electron-hole pair are generated. As shown in Fig. 1.4 (f), when more than one electron-hole pairs are generated, the recombination energy of one pair are not released through emitting a photon but through exciting another excited carrier to a higher excited state. This process is called Auger processes. The Auger effect is a phenomenon initially found in atomic physics discovered in 1925 by Pierre Victor Auger upon analysis of a Wilson cloud chamber experiment

[1.29]. As shown in Fig. 1.5, when an electron is removed from a core level of an atom, leaving a vacancy, an electron from a higher energy level may fall into this vacancy, resulting in a release of energy. Although sometimes this energy is released in the form of an emitted photon, the energy can also be transferred to another electron, which is ejected from the atom. Auger processeses also occur in bulk semiconductors. However, the efficiency of Auger processes differs greatly between the atomic and bulk semiconductor due to the different Coulomb electron-electron interactions. In atomic systems, where the electron-electron coupling is much stronger than the electron-photon coupling, the rates of Auger transitions are significantly greater than the rates of the radiative transitions. As a result, the decay of the multi-electron states in atomic systems is dominated by Auger processes. On the other hand, in bulk materials, due to the reduced Coulomb electron-electron coupling and kinematic restrictions imposed by energy and momentum conservation, the efficiency of Auger effects is greatly reduced.

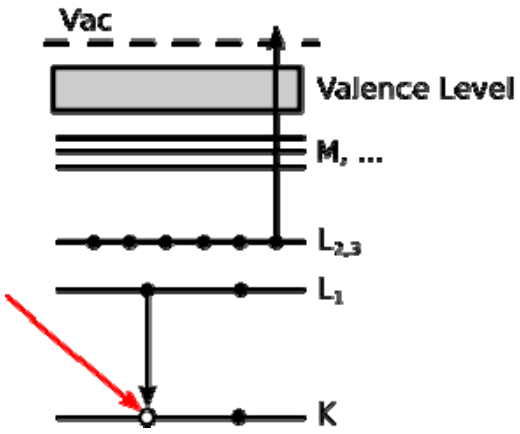

Fig. 1.5 Auger process in an atom. The energy released by an electron falling from a higher energy level into a vacancy in core level, is transferred to another electron which is then ejected from

In QDs, the situation for Auger processes becomes much complex compared with bulk and atom. On one hand, the three dimensional confinement increases the Coulomb interactions and should lead to increased Auger processes compared with the bulk. On the other hand, the confinement induced atomic like discrete energy levels decrease the possibility of the Auger processes due to the reduced availability of final states satisfying energy conservation. So, quite different properties of the Auger effects should be expected in QDs compared with those in the atom and in the bulk. Klimov et al. investigated the Auger processes in colloidal CdSe systematically [1.30]. The Auger rate was revealed to be quantized and have size dependence: the larger the size, the smaller the Auger transition rate. However, in their study, one photon excitation was used which is different from the conditions for bio-imaging. The study of two-photon excitation induced Auger effects in QDs thus needed for this purpose, is presented in this thesis.

In this thesis, the two-photon excitation, two-photon induced free-carrier (or excited-state) absorption, and Auger processes are investigated.

1.4 Literature review of TPA in colloidal CdSe and CdTe quantum dots

The first study of the nonlinear optical properties of QDs was carried out in 1989 by Cheng *et al*. on CdS QDs dissolved in organic solvents using two different sizes [1.31]. The experiments were done with the third harmonic generation method of time scale of nanosecond excitation at infrared at 1.91 μm. In this study, $\chi^{(3)}$ was found to increase with larger size. Only the magnitude and phase of $\chi^{(3)}$ was obtained while the TPA remained unknown. A more systematical study on the nonlinear optical properties of QDs was performed in 1992 by Cotter *et al*. on 25 different glasses containing Cd(S, Se) and Cd(S, Se, Te) QDs with radius ranging from 3.5 to 6 nm [1.32]. The imaginary and real parts of $\chi^{(3)}$ of the samples were investigated using the Z-scan method in pico-second time regime at 1.06 μm. It was revealed that the absolute value of both imaginary and real parts of $\chi^{(3)}$ increases with size, and the nonlinearity is predominantly refractive. In 1994, Banfi *et al*. reported a TPA study of $CdS_{1-x}Se_x$ QDs and CdTe QDs doped in glass [1.33]. The TPA coefficients have been determined through the nonlinear optical transmittance technique at 1.06 μm with pulse duration of 30 ps. In this work, Banfi, *et al*. normalized the TPA coefficient with volume fraction of QDs and drew the normalized TPA coefficient as a function of QDs' band gap. They

claimed that the TPA in these QDs was quite close to those in the bulk counterpart. However, no direct information could be obtained through these normalized TPA coefficients and so no other group in the world confirmed this observation till now.

There are three main drawbacks for the above three studies: Firstly, only one wavelength has been investigated while the TPA spectra remained unknown. Secondly, the pulse duration is in nanosecond or in picosecond regime. With such long laser pulses, other effects such as excited-state absorption and nonlinear scattering may occur and may affect the measurement. Finally, the qualities of the samples were poor because the density of trap state was large and so was the size dispersions. As a result, the measured values were wide scattered with a large degree of uncertainty.

With the fast revolutions in the laser systems as well as in the synthesis of QDs, the above drawbacks were quickly overcame. The laser pulse excitation moves from nanosecond to femtosecond with wavelengths tunable from ultraviolet to infrared. The qualities of QDs are also improved greatly: the size dispersion of QDs became narrower and densities of trap states in QDs were diminished. There has been a large amount of studies concerning TPA in various QDs. The review in this thesis will be focused on the experimental and theoretical TPA studies on CdSe QDs and CdTe QDs, which are belonging to II-VI group. CdSe QDs and CdTe QDs have once been considered as the proto-types for QDs due to their relative mature synthesis technique

comparing with those of other QDs. The PL of CdSe QDs and CdTe QDs could cover all the wavelength range from 500 to 750 nm. CdSe QDs and CdTe QDs thus have been intensely studied as promising candidates for bio-imaging.

As mentioned above, there existed discrepancies in the early TPA studies in QDs. Theoretical work was needed to deepen the understanding in this field. In 1996, Schmidt *et al*. reported their experimental work on the spectrum of TPA in CdSe QDs with different sizes and applied the model of spherically confined effective mass in TPA simulation [1.34]. At the same time, excitation spectra of two-photon fluorescence measurements at 5 K were performed with picosecond laser pulses. As a result, the first four dominant TPA transitions were assigned; fine exciton structures have been revealed to be blue shifted as compared to the bulk. However, the theoretical prediction of these exciton peaks strength was deviated with experimental results. In the same year, Fedorov *et al*. published their theoretical work on TPA transitions in II-VI systems based also on the spherically confined effective mass model where parabolic model was used to simplify the energy bands [1.35]. Different from Schmidt *et al*. who only presented a list of TPA transitions, Fedorov *et al*. gave analytical expressions for the TPA coefficients, taking the size distribution into account. This theoretical work proposed by Fedorov *et al*. has been adapted by Padilha *et al*. in 2005 [1.36]. Spectra dependence of scaling was obtained through the theory. The theory was compared with the

experimental measurement of the TPA spectra in CdTe QDs doped in glass. Their experimental work carried out with the femtosecond Z-scan method proved the theory of Fedorov, though, with some discrepancies [1.36]. In this paper, the authors concluded that TPA coefficients would increase with size at given wavelength, even after being normalized by the volume of QDs. In 2007, Padilha *et al*. reported experimental TPA study of CdSe QDs and CdTe QDs doped in glass and simulations based on k·p theory. They considered the band mixing between the heavy hole and the light hole [1.37]. The simulation shows an improvement in the fitting of the measured data. However, discrepancies still exist between the theoretical prediction and the experiment, especially in the higher energy region and for smaller size [1.37].

As summarized in the above paragraph, theoretical TPA QDs studies were conducted with the experimental support. Meanwhile, in the same period, many other experimental evidences have been published for the TPA in CdSe QDs and CdTe QDs using laser pulses at femtosecond regime. In 2003, Larson *et al*. published their experimental study on the TPA in water soluble CdSe/ZnS core/shell with different sizes [1.22]. In this study, the action cross-sections of CdSe/ZnS core/shell QDs were derived from two-photon microscopy and were compared with those of fluorescein in the wavelength range from 700 to 1000 nm. It was revealed that the action cross-sections of the CdSe/ZnS QDs are much larger than the ones of conventional labels and actually are the largest for any label ever used. Nevertheless, since the action

cross-section is the product of the TPA cross-section and fluorescence quantum efficiency, the contribution of the TPA cross-section can only be assumed and has not be accurately determined. Thus, TPA coefficients for CdSe QDs are still remained unknown.

In 2006, Pu *et al.* have studied colloidal CdTe QDs with six different sizes ranging from 4.4 to 5.4 nm in diameter. The TPA cross-sections have been found to be proportional to $R^{5.6}$, where R is the radius of QD [1.38]. In their study, however, TPA has been examined at only one wavelength. In the next year, He *et al.* have unambiguously measured the TPA spectra of colloidal CdTe QDs, but their average diameters are in the range from 6 to 8 nm with the size dependence remained unexamined [1.39].

In summary, TPA in CdSe and CdTe QDs has been investigated by many groups in theory and in experiments. However, the theoretical work still needs further improvement to predict TPA in very strong confinement where the band mixing between the conduction and valence bands cannot be neglected. For experimental studies, the action cross-sections of CdSe QDs were shown to be quite big but there were no experimental evidence to directly determine the spectrum of TPA coefficient of CdSe QDs. Furthermore, the intraband absorption in TPA generated carriers has not been studied systematically. This may contribute to the saturation of the photoluminescence. For CdTe QDs, a systematic study on both size- and wavelength-dependent TPA in colloidal CdTe QDs in very strong confinement regime is still in need.

1.5 Objectives and scope

The objectives of my PhD research project are four fold: i) to investigate the two-photon absorption (TPA) in colloidal CdSe QDs and CdTe QDs which belong to group II-VI by femtosecond Z-scan technique and by theoretical modeling. From this study, the TPA spectra of colloidal CdSe QDs and CdTe QDs in very strong confinement regime are to be obtained. The size-dependent TPA spectra of colloidal CdTe QDs in the very strong confinement regime are to be investigated by experiment as well as by theoretical simulation. The theory will consider both mixing between the conduction band and valence bands as well as the complex structure of the valence bands. Factors that contribute to the size effects are to be discussed; ii), relaxation dynamic of the QDs following TPA excitation is to be investigated using pump-probe spectroscopy; iii) the Auger effect following the TPA excitation is to be investigated; iv) the study in the excited-state absorption in CdSe QDs will also be presented in this thesis.

1.6 Layout of this thesis

Chapter 2 introduces the two-photon absorption theory in strong confinement QDs. To start with, several theories on the energy structure in QDs are reviewed briefly. Then the eight-band Pidgeon and Brown (PB) model, which has been applied in this thesis, is introduced in more detail. Energy levels as well as wave functions of CdTe QDs derived from this theory

are shown. For the last part in this chapter, the equations for the two-photon transition rate and the TPA coefficient are described. The calculations are based on the wave functions and energy levels obtained from the eight-band PB model.

Chapter 3 presents briefly the experimental techniques that are used in this thesis. It includes the description of experimental setups as well as the theoretical formula involved for the analysis of the experimental results. The laser systems used in this study are also described.

In Chapter 4, the TPA excitation and relaxation in colloidal CdSe QDs is studied with femtosecond Z-scans and transient absorption measurements is studied. The TPA spectra are investigated in a wavelength range from 720 to 950 nm. The spectra are then compared with previously published theoretical papers. Furthermore, the intraband absorption of two-photon-excited carriers has also been studied. For the ultrafast relaxation, the Auger recombination and quantized Auger rate are discussed in detail.

Chapter 5 reports on the experimental and theoretical study on the TPA in colloidal CdTe QDs with three different sizes in the very strong confinement regime. Experimental measurements of TPA cross-section in a wavelength range from 720 to 950 nm are conducted. A TPA theoretical simulation based on the spherical eight-band Pidgeon and Brown model which takes the band mixing into account is presented in this chapter. In this simulation, the potential barrier is taken as an infinite one. Then, comparison is made between

the experimental results and theoretical calculations. The factors that contribute to the increase in the TPA with dot size and the effects of size dispersion on the TPA are discussed.

In Chapter 6, all the important experimental and theoretical findings in this thesis are summarized. Further steps for future studies in this field are proposed.

REFERENCES

[1.1] R. Dingle, W. Wiegmann, and C. H. Henry, Phys. Rev. Lett. **33**, 827 (1974).

[1.2] L. L. Chang, L. Esaki, and R. Tsu, Appl. Phy. Lett. **24**, 593 (1974).

[1.3] P. M. Petroff, A. C. Gossard, R. A. Logan, and W. Wiegmann, Appl. Phys. Lett. **41**, 635 (1982).

[1.4] M. A. Reed, R.T. Bate, K. Bradshaw, W.M. Duncan, W.M. Frensley, J. W. Lee, and H. D. Smith, J Vacuum Sci.Technol. B, **4**, 358 (1986).

[1.5] S. Schmitt-Rink, D. A. B. Miller, and D. S. Chemla, Phys. Rev. B, **35**, 8113 (1987).

[1.6] A. P. Alivisatos, Science **271**, 933 (1996).

[1.7] M. E. Akerman, W. C. W. Chan, P. Laakkonen, S. N. Bhatia, and E. Ruoslahti, Proc. Nat. Acad. Sci. **99**, 12617 (2002).

[1.8] U. Woggon, *Optical Properties of Semiconductor Quantum Dots*, (Spring, Berlin, 1997).

[1.9] J. T. Seo, Q. Yang, S. Creekmore, D. Temple, L. Qu, W. Yu, A. Wang, X. Peng, A. Mott, M. Namkung, S. S. Jung, and J. H. Kim, Physica E **17**, 101 (2003)

[1.10] V. A. Fonoberov, and A. A. Balandin, Appl. Phys. Lett. **85**, 5579 (2004).

[1.11] V. I. Klimov, A. A. Mikhailovsky, Su Xu, A. Malko, J. A. Hollingsworth, C. A. Leatherdale, H. –J. Eisler, and M. G. Bawendi, Science **290,** 314 (2000)

[1.12] K. K. Kim, and N. Koguchi, Y. W. Ok, T. Y. Seong, and S. J. Park, Appl. Phys. Lett. **84**, 3810 (2004).

[1.13] X. Michalet, F. F. Pinaud, L. A. Bentolila, J. M. Tsay, S. Doose, J. J. Li, G. Sundaresan, A. M. Wu, S. S. Gambhir, and S. Weiss, Science, **307**, 538 (2005).

[1.14] B. L. Justus, R. J. Tonucci, and A. D. Berry, Appl. Phys. Lett. **61**, 3151 (1992).

[1.15] V. A. Fonoberov and A. A. Balandin, Phys. Rev. B, **70**, 195410 (2004).

[1.16] M. D. Dvorak, B. L. Justus, D. K. Gaskill, and D. G. Hendershot, Appl. Phys. Lett. **66**, 804 (1995).

[1.17] Paul Alivisatos, Nature Biotechnology **22**, 47 (2004).

[1.18] C. Cornet, C. Labbe, H. Folliot, P. Caroff, C. Levallois, O. Dehaese, J. Even, A. Le Corre, and Loualiche, Appl. Phys. Lett. **88**, 171542 (2006).

[1.19] W. C. W. Chan and S Nie, Science **281** 2016-2018 (1998).

[1.20] J. W. M. Chon, M. Gu, C. Bullen, and P. Mulvaney, Appl. Phys. Lett. **84**, 4472 (2004).

[1.21] R. Tommasi, M. Lepore, and I. M. Catalano, Solid State Comm. **85**, 539 (1993).

[1.22] D. R. Larson, W. R. Zipfel, R. M. Williams, S. W. Clark, M. P. Bruchez, F. W. Wise, and W. W. Webb, Science **300**, 1434 (2003).

[1.23] Al. L. Efros and M. Rosen, Annu. Rev. Mater. Sci. **30**, 475 (2000).

[1.24] Goeppert-Mayer M, Ann Phys **9**, 273 (1931).

[1.25] W. Kaiser and C.G.B. Garrett , Phy. Rev. Lett. **7**, 229 (1961).

[1.26] I. D. Abella, Phys. Rev. Lett. **9**, 453 (1962).

[1.27] V. I. Klimov, A. A. Mikhailovsky, and D. W. McBranch, C. A. Leatherdale and M. G. Bawendi, Phys. Rev. B **61**, R13 349 (2001).

[1.28] V. I. Klimov and D. W. McBranch, Phys. Rev. Lett. **80**, 4028 (1998)

[1.29] E. H. S. Burhop, *The Auger Effect and Other Radiationless Transitions*, (Cambridge, Cambridge University Press, 1952).

[1.30] V. I. Klimov, A. A. Mikhailovsky, D. W. McBranch, C. A. Leatherdale, and M. G. Bawendi, Science **287**, 1011 (2000).

[1.31] Lap-Tak Cheng, Norman Herron, and Ying Wang, J. Appl. Phys. **66** 3417 (1989).

[1.32] D. Cotter, M. G. Burt, and R. J. Manning, Phys. Rev. Lett. **68**, 1200 (1992).

[1.33] G. P. Banfi, V. Degiorgio, H. M. Tan, and A. Tomaselli, Phys. Rev. B **50**, 5699 (1994).

[1.34]. M. E. Schmidt, S. A. Blanton, M. A. Hines, and P. Guyot-Sionnest, Phys. Rev. B **53**, 12629 (1996).

[1.35] A. V. Fedorov, A. V. Baranov, and K. Inoue, Phys. Rev. B **54**, 8627 (1996).

[1.36]. L. A. Padilha, A. A. Neves, C. L. Cesar, L. C. Barbosa, and C. H. Brito Crus, Appl. Phys. Lett. **85**, 3256 (2004).

[1.37] L. A. Padilha, J. Fu, D. J. Hagan, E. W. Van Stryland, C. L. Cesar, L. C. Barbosa, C. H. B. Cruz, D. Buso, and A. Martucci, Phys. Rev. B **75**, 075325 (2007).

[1.38] S. C. Pu, M. J. Yang, C. C. Hsu, C. W. Lai, C. C. Hsieh, S. H. Lin, Y. M. Cheng, and P. T. Chou, Small **2**, 1308 (2006).

[1.39] G. H. He, Q. D. Zheng, K. T. Yong, and A. Urbus, Appl. Phys. Lett. **90**, 181108 (2007).

Chapter II

TPA THEORY FOR STRONG CONFINEMENT QUANTUM DOTS

2.1 Introduction

To calculate the two-photon absorption (TPA) in materials, we have to know the electronic structures including the band energies and the corresponding wave functions. The TPA absorption then can be calculated by applying Fermi's golden rule, with the known initial, intermediate, final states and the corresponding wave functions of these states. In order to calculate the band energies and the corresponding wave functions, various numerical methods thus have been developed, such as the tight binding method, the pseudo-potential method, and the orthogonalized plane wave method. These methods are suitable to calculate band diagrams in which the band energies E are functions of wave vector k. However, the above mentioned numerical methods suffer from their complexity and thus are time consuming, as have been discussed in detail in many textbooks on solid-state physics [2.1, 2.2]. On the other hand, for TPA, only the extremas (normally at $k = 0$) in the band diagram dominate the process due to the much higher transition rates than in other regions. Many assumptions thus can be made to simplify the calculation

such as the effective mass approximation (EMA) and the envelop function approximation (EFA).

In the EMA, the bands near the extremas are assumed to have simply parabolic forms. With such an approximation, the carriers (electrons and holes) in quantum dots (QDs) can be regarded as particles in a sphere with an 'effective mass' $m^*_{c,v}$ where *c* and *v* represent the conduction band and the valence band, respectively. The energy of the particle is then given by: $E^{c,v}(k) = E^{c,v} + \hbar^2 k^2 / (2m^*_{c,v})$, where $E^{c,v}$ is the conduction/valence band energy at $k = 0$. Despite its simplicity, EMA is found to be a powerful tool even for strong confinement QDs and is only invalid for QDs in an extreme small regime [2.3-2.12].

Whereas the EMA is concerned on the band energy, the other approximation EFA, refers to the wave function. As we know from bulk semiconductors, the electronic structure in a periodic potential can be derived from the Hamiltonian. The general theory is the Bloch theorem where we know that the eigen wave function $\psi_{nk}(r)$ of an electron in a periodic potential (called the Bloch function) is given by:

$$\psi_{nk}(r) = e^{ik \cdot r} u_{nk}(r) \tag{2.1}$$

where *n* refers to the ordinal number of the level with a given symmetry and *k* the wave vector of the electron. To satisfying the boundary condition in QDs, the wave function of electron/hole is then written as a linear combination of Bloch functions:

$$\psi_n^{QDs} = \sum_k C_{nk} u_{nk}(r) \exp(ik \cdot r) \tag{2.2}$$

where C_{nk} is the expansion coefficient. Here comes the envelop function approximation (EFA). In the EFA, the function $u_{nk}(r)$ is assumed to be weakly dependent on k (normally is true around k=0), Equation (2.2) can be rewritten as:

$$\psi_n^{QD} = u_{n0}(r) \sum_k C_{nk} \exp(ik \cdot r) = u_{n0}(r) f_n^{QD}(r) \tag{2.3}$$

where $f_n^{QD}(r)$ is the eigen single particle "envelop function". The wave functions of electron and hole in QDs are then represented as the product of the envelop function and the Bloch function of the conduction (electron) and valence (hole) bands. The Bloch functions are known from the bulk material and the QDs problem is reduced to determine the envelop eigen function of $f_n^{QD}(r)$. The wavefuncion of electron or hole then is represented as:

$$\psi^{QD} = \sum_n \psi_n^{QD} = \sum_n u_{n0}(r) f_n^{QD}(r) \tag{2.4}$$

Within EMA and EFA, many models have been proposed for the calculation of energy structure in QDs with different extent of assumption and simplicity. In the next parts of Section 2.1, the band structure of group II-VI will be introduced briefly followed by the description of three models: the parabolic model, the Luttinger and Kohn (LK) model, and the Pigeon and Brown (PB) model. In Section 2.2, the electron/hole structure of QDs based on the PB model will be described in more detail. The calculation on the two-photon transition in QDs will be explained in Section 2.3.

2.1.1 The band structure in group II-VI semiconductors

For the zinc blend or wurtzite structures, the lowest conduction minimum is formed from *S*-type orbitals and the valence band is formed from *P*-type orbitals [2.12]. By considering the electron spin, the lowest conduction band is two-fold degenerate whereas the valence band is six-fold degenerate. Furthermore, the spin-orbit interaction makes the valence band split further: a four-fold degenerate band with a total unit cell angular momentum $J=3/2$ and a two-fold degenerate band with $J=1/2$. The energy separation between these bands is determined by the strength of the spin-orbit interaction. The $J=3/2$ band is further split into light- and heavy-hole subbands with J projections $M_J=1/2$ and $M_J=3/2$, respectively. At the Γ-point of the Brillouin zone, the splitting is zero for diamond and zinc blend lattices and nonzero for the wurtzite structure. Fig. 2.1 shows the band structure of a typical semiconductor with Zinc Blend or wurtzite lattice symmetry.

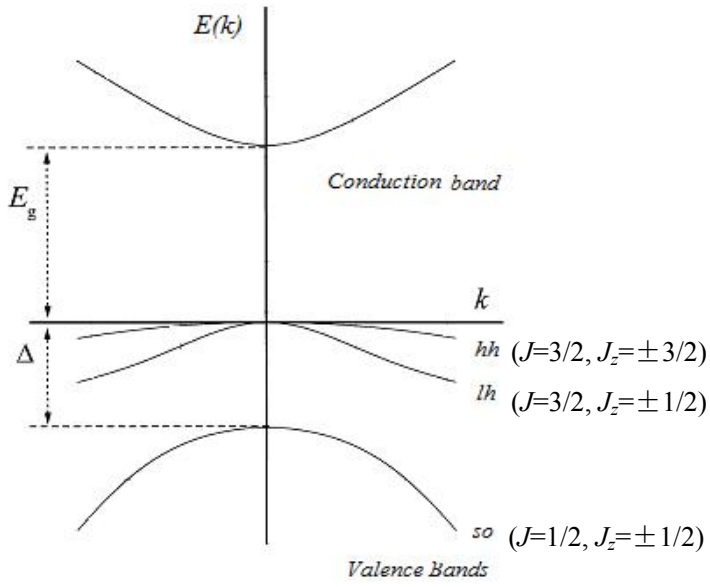

Fig. 2.1 Bulk band structure of a typical semiconductor with Zinc Blend or cubic lattice symmetry. Heavy, light, and spin orbit split-off valence subbands are denoted as "hh", "lh", and "so", respectively.

2.1.2 The parabolic & particle-in-a-sphere model

The first and simplest theoretical description of QDs was based on the parabolic band model combined with the "particle in a sphere" model [2.3-2.5]. There are two assumptions in this model. One is that the spherical nanocrystal is surrounded by an infinite potential barrier; and the other approximation in this parabolic model is that the coulomb interaction between the electron and hole is ignored. The latter approximation is also called the "strong confinement assumption" where the electron and hole can be treated as independent to each other and each can be described as "particle in a sphere". With these two assumptions, the energy bands of electron and hole are

parabolic in *k* space, and analytical solutions of the energy levels are obtained [2.3-2.5].

In parabolic model, the envelop functions can be expressed in terms of the spherical Bessel function (j_l) and the spherical harmonic functions ($Y_{l,m}$) [2.3]:

$$f_{n,l,m}^{e,h}(r) = \sqrt{\frac{2}{a^3}} \frac{j_l(\xi_{l,n} \cdot r)}{j_{l+1}(\xi_{l,n} \cdot a)} Y_{l,m}(\Omega) \tag{2.5}$$

where Ω is the solid angle of the vector *r*; $\xi_{l,n}^*$ is the *n*th root of the spherical Bessel function of order *l; l* is the orbital angular momentum (*l* = 0,1,2,…, corresponding to states with S, P, D,… symmetries), and *m* is the projection of the orbital angular momentum ($m = 0, \pm 1, \cdots \pm l$), , *n* is the quantum number *(n* = 1,2,3,…).

The quantized energy of the electron and hole can be written in parabolic approximation as :

$$E_{l,n}^{e,h} = \frac{\hbar^2 \xi_{l,n}^2}{2m_{e,h}^* R^2} \tag{2.6}$$

where $m_{e,h}^*$ is the effective mass of electron and hole respectively, *R* is the crystal radius. It can be seen from Equation (2.6) that the carrier energy in QDs increases with $1/R^2$, in contrast to the Coulomb energy of the electron-hole interaction which increase with *1/R*. From this simple relationship, we can see that for strong confinement QDs, the effect of Coulomb interaction between electron and hole becomes weaker and the confinement energy becomes stronger.

Fedorov *et al.* has applied this simple model in the calculation of the two-photon absorption (TPA) [2.13]. Analytical expressions have been derived. This work has been proved by Padilha *et al.* in CdTe QDs [2.14, 2.15]. However, for strong confinement QDs with size smaller than the Bohr radius, the TPA prediction based on this parabolic & particle-in-a-sphere model shows a large discrepancy to the experimental results, both in transition energy and in the profile of TPA spectrum [2.15, 2.16, 2.17].

2.1.3 $k \cdot p$ methods

Though the parabolic model gives a reasonable description on the QDs band, it can only provide a qualitative description and fails in describing the real band structure in QDs. The real band structure in QDs is much more complex: both the conduction and the valence bands are warped and are non-parabolic; there are couplings between the conduction and valence bands and there are couplings among the valences bands.

The real band structure requires a more complex theory. Among the different theories, the $k \cdot p$ method is often a sufficient and relatively simple approach giving an analytical description for QDs in strong confinement regime.

The $k \cdot p$ method was introduced by Bardeen [2.18] and Seitz [2.19]. It is a perturbation method where the eigen values and eigen functions are expanded as a function of k. In $k \cdot p$ theory, the non-parabolicity of the

conduction and valence bands as well as the mixing between the bands, can be considered. Depending on the complexity of the band structure, the $k \cdot p$ theory can be applied in many different ways [2.20]. When the interest is in the six valence bands ignoring their band mixing with the conduction bands, the mehod is called six-band model. When the mixing between the conduction band and valence bands, as well as the complex structure of valence band are considered, it is called eight-band model. Following the name of the theoreticians who developed these models, six-band and eight-band model are also recognized as "Luttinger and Kohn" model and the "Pigeon and Brown" model, respectively [2.8, 2.9]. All the above models within the $k \cdot p$ theory have also been called "multiband effective mass approximation model".

To introduce the $k \cdot p$ method, we should start with Bloch functions $\psi_{nk}(r)$ which are solutions of the Schrodinger equation for the single particle Hamiltonian. The single particle Hamiltonian is:

$$H_0 = \frac{p^2}{2m_0} + V(r) \tag{2.7}$$

where *V(r)* is the periodic potential of the crystal lattice. Take the Bloch functions (2.1) into Equation (2.7) gives:

$$\begin{aligned} & H_0 \Psi_{nk}(r) = E_{nk} \Psi_{nk}(r) \\ & \Rightarrow [\frac{p^2}{2m_0} + V(r)] u_{nk}(r) \exp(ik \cdot r) = E_{nk} u_{nk}(r) \exp(ik \cdot r) \\ & \Rightarrow \exp(ik \cdot r)[\frac{p^2}{2m_0} + V(x) + \frac{k \cdot p}{m_0} - \frac{\hbar^2 k^2}{2m_0}] u_{nk}(r) = E_{nk} u_{nk}(r) \exp(ik \cdot r) \end{aligned} \tag{2.8}$$

The term $\exp(ik \cdot r)$ can be taken off from both side of (2.8), and the equation becomes:

$$[\frac{p^2}{2m_0}+V(x)+\frac{\hbar}{m_0}k\cdot p]u_{nk}(r)=(E_{nk}-\frac{\hbar^2k^2}{2m_0})u_{nk}(r) \tag{2.9}$$

Equation (2.9) is the general Schrödinger equation in the $k\cdot p$ method. The band structure is expanded analytically around a particular point in *k*-space, typically *k*=0. The band energies and wave functions are then expressed in terms of the periodic functions u_{nk} and their energies E_{nk} around this particular point.

Assuming that u_{n0} and E_{n0} are known around $k = 0$, Eqn. (2.9) becomes:

$$[H_0+\frac{\hbar}{m_0}k\cdot p]u_{nk}(r)=(E_n(k)-\frac{\hbar^2k^2}{2m_0})u_{nk}(r) \tag{2.10}$$

where

$$H_0=\frac{p^2}{2m_0}+V(r) \tag{2.11 a}$$

$$H_0u_{n0}(r)=E_n(0)u_{n0}(r) \tag{2.11 b}$$

$$u_{nk}(r)=\sum_{n'}a_{n'}u_{n'0}(r) \tag{2.11 c}$$

The band-edge functions $u_{n0}(r)$ can be represented as following: for the conduction band: $|S\uparrow\rangle$, $|S\downarrow\rangle$; and for valence band: $|X\uparrow\rangle$, $|Y\downarrow\rangle$, $|Z\uparrow\rangle$, $|X\downarrow\rangle$, $|Y\uparrow\rangle$, $|Z\downarrow\rangle$. Here, *S, X, Y, Z* are similar to *S*-like and *P*-like atomic states (lowest order spherical harmonics Y_{00}, Y_{10}, Y_{11} etc.) The basic Bloch functions are usually chosen to be as the eigen functions of orbital angular momentum operators L^2 and L_z. It is convenient to choose the basis functions:

$$u_{10}=u^c_{-1/2}=|iS\downarrow\rangle$$

$$u_{30} = u^{v}_{3/2,3/2} = \left| \frac{1}{\sqrt{2}}(X + iY)\uparrow \right\rangle$$

$$u_{50} = u^{v}_{3/2,1/2} = \left| \frac{i}{\sqrt{6}}[(X + iY)\downarrow -2Z\uparrow] \right\rangle$$

$$u_{70} = u^{v}_{1/2,-1/2} = \left| \frac{i}{\sqrt{3}}[-(X - iY)\uparrow +Z\downarrow] \right\rangle \qquad (2.12\text{ a})$$

and

$$u_{20} = u^{c}_{1/2} = S\uparrow,$$

$$u_{40} = u^{v}_{3/2,-3/2} = \frac{i}{\sqrt{2}}(X - iY)\downarrow,$$

$$u_{60} = u^{v}_{3/2,-1/2} = \frac{1}{\sqrt{6}}[(X - iY)\uparrow +2Z\downarrow]$$

$$u_{80} = u^{v}_{1/2,1/2} = \frac{1}{\sqrt{3}}[(X + iY)\downarrow +Z\uparrow] \qquad (2.12\text{ b})$$

The first four basis functions (2.12a) are degenerate with the last four degenerate four basis functions (2.12b).

2.1.3.1 Luttinger and Kohn model

The Luttinger and Kohn (LK) model is a 6-band model: the heavy hole, light hole, and spin-orbit split-off bands, all doubly degenerate. The couplings between the valence bands to the two degenerate conduction bands are ignored. It is a good approach for wide-band-gap semiconductors where the band gap is bigger than the quantized energy levels. In the Luttinger and Kohn model, the valence bands can be described using three parameters: $\gamma_1 \gamma_2 \gamma_3$. For a cubic crystal lattice (such as Zinc blend structure), the parameter number is reduced

to 2 since $\gamma = \gamma_2 = \gamma_3$. The effective masses of heavy (m_{hh}^*) light (m_{lh}^*) and split-off (m_{so}^*) hole bands can be written in terms of the free electron masses as follows:

$$m_{hh}^* = m_0/(\gamma_1 - 2\gamma) \quad m_{lh}^* = m_0/(\gamma_1 + 2\gamma) \; m_{so}^* = m_0/\gamma_1 \tag{2.13}$$

The Luttinger and Kohn model is a starting point to obtain the hole eigen-states and the energies in quantum dots. It takes into account the spin-orbit interaction as well as the six valence bands. In general, in the LK model, the eigen-value equation below has to be solved:

$$\sum_{j'=1}^{6} H_{jj'}^{LK} a_{j'}(k) = E a_j(k) \tag{2.14}$$

where

$$H_{jj'} = < u_{j0} | H | u_{j'0} > \tag{2.15 a}$$

$$u_{nk}(r) = \sum_{j=1}^{6} a_j(k) u_{j0}(r) \tag{2.15 b}$$

$$H = \frac{p2}{2m0} + V(r) + \frac{\hbar}{4m_0^2 c^2} \nabla V \times p \cdot \sigma \tag{2.15 c}$$

The Luttinger and Kohn model treats the complex structure of the valence band but does not neglect the band mixing between the valence bands and the conduction bands. It works well for large-band-gap materials. However, for small and moderate semiconductors in strong confinement regime where the quantized energy is comparable or even larger than the band gap, the mixing between the conduction and valence band cannot be ignored.

2.1.3.2 Pidgeon and Brown (PB) model

Based on the Luttinger and Kohn model, Pidgeon and Brown (PB) proposed an 8-band model which takes into account both the complex structure of the valence band as well as the conduction-valence band mixing at the same time, in the vicinity of the Γ point of the Brillouin zone [2.9]. The importance of this model for the lowest symmetry QDs in spherical nanocrystals have been shown by many groups [2.21-2.22].

In general, in the PB model, the eigen-value equation below has to be solved:

$$\sum_{j'=1}^{8} H_{jj'}^{LK} a_{j'}(k) = E a_j(k) \tag{2.16}$$

where

$$H_{jj'} = < u_{j0} | H | u_{j'0} > \tag{2.17 a}$$

$$u_{nk}(r) = \sum_{j=1}^{8} a_j(k) u_{j0}(r) \tag{2.17 b}$$

$$H = \frac{p2}{2m0} + V(r) + \frac{\hbar}{4m_0^2 c^2} \nabla V \times p \cdot \sigma \tag{2.17 c}$$

In this model, the effects of non-parabolic behavior in the conduction and light hole bands, the warping of all the bands and the band coupling between the conduction and valence bands have been considered.

Efros *et al*. have given the analytical expressions for the band energy and wave-functions in QD by using this PB model as a basis [2.23]. Our calculation of the energy levels and the wave-functions are based on their work.

2.2 Electron structure of group II-VI quantum dots based on PB model

2.2.1 Band structure of group II-VI semiconductors

As mentioned above, the PB model is an eight-band LK model. The Hamiltonian of the PB model is as follows [2.23]:

	$u^c_{1/2}$	$u^c_{-1/2}$	$u^v_{3/2,3/2}$	$u^v_{3/2,1/2}$	$u^v_{3/2,-1/2}$	$u^v_{3/2,-3/2}$	$u^v_{1/2,1/2}$	$u^v_{1/2,-1/2}$
$u^c_{1/2}$	$E_g+\frac{\alpha}{2m_0}p^2$	0	$\frac{i}{\sqrt{2}}Vp_+$	$\sqrt{\frac{2}{3}}Vp_z$	$\frac{i}{\sqrt{6}}Vp_-$	0	$\frac{i}{\sqrt{3}}Vp_z$	$\frac{i}{\sqrt{3}}Vp_-$
$u^c_{-1/2}$	0	$E_g+\frac{\alpha}{2m_0}p^2$	0	$-\frac{1}{\sqrt{6}}Vp_+$	$i\sqrt{\frac{2}{3}}Vp_z$	$-\frac{1}{\sqrt{2}}Vp_-$	$\frac{i}{\sqrt{3}}Vp_+$	$-\frac{i}{\sqrt{3}}Vp_z$
$u^v_{3/2,3/2}$	$-\frac{i}{\sqrt{2}}Vp_-$	0	$-(P+Q)$	$-L$	-M	0	$-i\sqrt{\frac{1}{2}}L$	$i\sqrt{2}M$
$u^v_{3/2,-3/2}$	0	$-\frac{1}{\sqrt{2}}Vp_+$	0	$-M^*$	L^*	$-(P+Q)$	$i\sqrt{2}M^*$	$i\sqrt{1/2}L^*$
$u^v_{3/2,1/2}$	$\sqrt{3/2}Vp_z$	$-\frac{1}{\sqrt{6}}Vp_-$	$-L^*$	$-(P-Q)$	0	$-M$	$i\sqrt{2}Q$	$-i\sqrt{3/2}L$
$u^v_{3/2,-1/2}$	$-\frac{i}{\sqrt{6}}Vp_+$	$-i\sqrt{3/2}Vp_z$	$-M^*$	0	$-(P-Q)$	L	$i\sqrt{3/2}L^*$	$i\sqrt{2}Q$
$u^v_{1/2,1/2}$	$-\frac{i}{\sqrt{3}}Vp_z$	$-\frac{i}{\sqrt{3}}Vp_-$	$i\sqrt{1/2}L^*$	$-i\sqrt{2}Q$	$-i\sqrt{3/2}L$	$-i\sqrt{2}M$	$-\Delta-P$	0
$u^v_{1/2,-1/2}$	$\frac{1}{\sqrt{3}}Vp_+$	$-\frac{1}{\sqrt{3}}Vp_z$	$-i\sqrt{2}M^*$	$i\sqrt{3/2}L^*$	$-i\sqrt{2}Q$	$-i\sqrt{1/2}L$	0	$-\Delta-P$

(2.18)

The operators in the Hamiltonian are expressed in terms of the momentum operators:

$$p_{x,y,z}=-i\hbar\nabla_{x,y,z};\quad p_\pm=p_x\pm ip_y$$

$$p_\perp^2=p_x^2+p_y^2;\quad P=\frac{\gamma 1}{2m_0}p^2 \tag{2.19}$$

$$Q=\frac{\gamma}{2m_0}(p_\perp^2-2p_z^2);\quad L=\frac{-i\sqrt{3}\gamma}{m_0}p_zp_-;\quad M=\frac{\sqrt{3}\gamma}{2m_0}p_-^2$$

Kane matrix element $V=-i<S|\hat{p}_z|Z>/m_0$.

In spherical nanocrystals, each electron or hole state is characterized by its

parity ($\pm$), total angular momentum $j = J + L$, where L is the envelope angular momentum, and the projection of the total angular momentum $m = j_z$. The wave-function of these states can be written as a linear expansion in the eight Bloch functions:

$$\psi_{j,m}^{\pm}(r) = f_C(r)^{\pm} \sum_{\mu=-1/2}^{\mu=1/2} \Omega_{\mu}^{c} u_{\mu}^{c} + \sum_{i=1,2} f_{hi}^{\pm}(r) \times \sum_{\mu=-3/2}^{3/2} \Omega_{\mu}^{hi} u_{3/2,\mu}^{v} + f_s(r)^{\pm} \sum_{\mu=-1/2}^{1/2} \Omega_{\mu}^{s} u_{1/2,\mu}^{v} \tag{2.20}$$

An explicit analytical representation of the angular Ω function is given in Ref. [2.24].

2.2.2 Wave-functions of group II-VI semiconductors

The wave-functions of even states are given by [2.23]:

$$\begin{aligned}
f_{c,j}^{+} &= C_c^{+}(cp) j_{j-1/2}(k_c r) + C_c^{+}(h_-) j_{j-1/2}(k_- r) + C_c^{+} j_{j-1/2}(k_+ r) \\
f_{h1,j}^{+} &= \frac{v\sqrt{1+3\eta_j^{+}}}{\sqrt{6}} \left[\frac{k_c \Lambda_h(k_c) C_c^{+}(cp) j_{j+1/2}(k_c r)}{\Lambda_0(k)} + \frac{k_- \Lambda_k(k_-) C_{cp}^{+}(h_-) j_{j+1/2}(k_- r)}{\Lambda_0(k_-)} + \right. \\
&\quad \left. \frac{k_+ \Lambda_h(k_+) C_c^{+}(h_+) j_{j+1/2}(k_+ r)}{\Lambda_0(k_+)} \right] + \sqrt{3(1-\eta_j^{+})} C_{hh}^{+} j_{j+1/2}(k_h r) \\
f_{h2,j}^{+} &= -\frac{v\sqrt{1-\eta_j^{+}}}{2} \left[\frac{k_c \Lambda_h(k_c) C_c^{+}(cp) j_{j-3/2}(k_c r)}{\Lambda_0(k_c)} + \frac{k_- \Lambda_h(k_-) C_{cp}^{+}(h_-) j_{j-3/2}(k_- r)}{\Lambda_0(k_-)} \right. \\
&\quad \left. + \frac{k_+ \Lambda_h(k_+) C_c^{+}(h_+) j_{j-3/2}(k_+ r)}{\Lambda_0(k_+)} \right] + \sqrt{(1+3\eta_j^{+})} C_{hh}^{+} j_{j-3/2}(k_h r) \\
f_{s,j}^{+} &= \frac{v}{\sqrt{3}} \left[\frac{k_c \Lambda_s(k_c) C_c^{+}(cp) j_{j+1/2}(k_c r)}{\Lambda_0(k_c)} + \frac{k_- \Lambda_s(k_-) C_{cp}^{+}(h_-) j_{j+1/2}(k_- r)}{\Lambda_0(k_-)} \right. \\
&\quad \left. + \frac{k_+ \Lambda_s(k_+) C_c^{+}(h_+) j_{j+1/2}(k_+ r)}{\Lambda_0(k_+)} \right]
\end{aligned} \tag{2.21}$$

where

$$\Lambda_0(k) = (\gamma_1 k^2 + \delta + \varepsilon)[(\gamma_1 + 2\gamma)k^2 + \varepsilon] - 8\gamma^2 k^4$$

$$\Lambda_h(k) = \delta + \varepsilon + (\gamma_1 - 2\gamma)k^2$$

$$\Lambda_s(k) = \varepsilon + (\gamma_1 - 2\gamma)k^2$$

The wave-functions of odd states are given by [2.23]:

$$f_{c,j}^- = C_c^-(cp)\, j_{j+1/2}(k_c r) + C_c^-(h_-)\, j_{j+1/2}(k_- r) + C_c^{-+}\, j_{j+1/2}(k_+ r)$$

$$f_{h1,j}^- = \frac{v\sqrt{1-3\eta_j^-}}{\sqrt{6}}\left[\frac{k_c \Lambda_h(k_c) C_c^-(cp)\, j_{j-1/2}(k_c r)}{\Lambda_0(k)} + \frac{k_- \Lambda_k(k_-) C_{cp}^-(h_-)\, j_{j-1/2}(k_- r)}{\Lambda_0(k_-)} + \frac{k_+ \Lambda_h(k_+) C_c^-(h_+)\, j_{j-1/2}(k_+ r)}{\Lambda_0(k_+)}\right] + \sqrt{3(1+\eta_j^-)}\, C_{hh}^- j_{j-1/2}(k_h r)$$

$$f_{h2,j}^- = -\frac{v\sqrt{1+\eta_j^-}}{2}\left[\frac{k_c \Lambda_h(k_c) C_c^-(cp)\, j_{j+3/2}(k_c r)}{\Lambda_0(k_c)} + \frac{k_- \Lambda_h(k_-) C_{cp}^-(h_-)\, j_{j+3/2}(k_- r)}{\Lambda_0(k_-)} + \frac{k_+ \Lambda_h(k_+) C_c^-(h_+)\, j_{j+3/2}(k_+ r)}{\Lambda_0(k_+)}\right] + \sqrt{(1-3\eta_j^-)}\, C_{hh}^- j_{j+3/2}(k_h r)$$

$$f_{s,j}^- = \frac{v}{\sqrt{3}}\left[\frac{k_c \Lambda_s(k_c) C_c^-(cp)\, j_{j-1/2}(k_c r)}{\Lambda_0(k_c)} + \frac{k_- \Lambda_s(k_-) C_{cp}^+(h_-)\, j_{j-1/2}(k_+ r)}{\Lambda_0(k_-)} + \frac{k_+ \Lambda_s(k_+) C_c^-(h_+)\, j_{j-1/2}(k_+ r)}{\Lambda_0(k_+)}\right] \tag{2.22}$$

The energy levels of QDs are then determined by the boundary conditions that outside the radius of the QDs, the wave-functions vanish [2.23].

2.3 TPA in strong confinement quantum dots

With the above PB method, the wave functions and energy levels of electron/hole have been obtained by considering both the mixing between the conduction and valence bands as well as the complexity of the valence bands. In this section, the calculation of the two-photon absorption (TPA) in QDs will

be introduced. The wave functions and energies will be based on the PB model.

2.3.1 General information of TPA transition in quantum dots

The two-photon generation rate (TPGR) of electron-hole pairs by plane-polarized light with frequency ω can be represented in second-order perturbation theory with respect to the electron-photon interaction as (Fermi Golden Rule):

$$W^{(2)} = \frac{2\pi}{\hbar} \sum_{v1,v0} | M_{v1,v0} |^2 \ \delta(E_{v1} - E_{v0} - 2\hbar\omega) \tag{2.23}$$

where

$$M_{v1,v0} = \sum_{v2} \frac{V_{v1,v2} V_{v2,v0}}{E_{v2} - E_{v1} - \hbar\omega - i\hbar\gamma_{v2}} \tag{2.24}$$

where the subscripts, v_0, v_1, v_2 denote sets of quantum numbers for initial, final, and intermediate states of an electron subsystem, respectively, and the parameter of γ_v is the inverse lifetime of the state v [2.20].

As shown in Fig. 2.2, each TPA transition involves two processes: one is interband and the other is intraband. From Fig. 2.2 we can see that the interband is from the valence bands to conduction band. However there are two paths ways for the intraband transiton: from conduction band to conduction band or from valence band to valence bands.

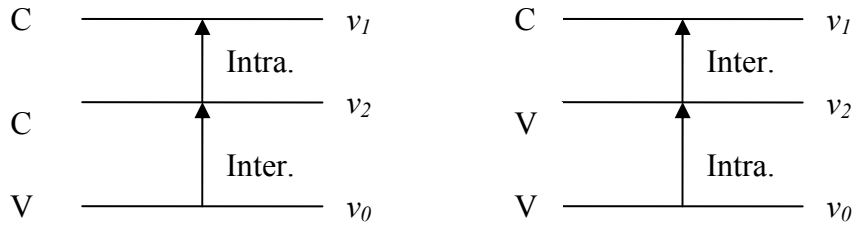

Fig. 2.2 Schematic diagram of the interband (inter.) and intraband (intra.) transitions involved in two-photon absorption.

The two-photon absorption coefficient β is defined such that for radiation intensity *I*, the rate at which energy is absorbed in an unit volume of the material is βI^2. The interband transition rate per unit volume associated with the simultaneous absorption of the two photons of frequency ω is given by [2.25]:

$$\beta = W^{(2)} 2\hbar\omega / I^2 \tag{2.25}$$

2.3.2 TPA transition in quantum dots considering band mixing

The parity of the wave functions for electron and hole can be classified as either even or odd. For wave function $\psi(x)$ in even state, there exists: $\psi(-x) = \psi(x)$, whereas in odd state: $\psi(-x) = -\psi(x)$. In this thesis, only the even state is used to illustrate the process of calculating the TPA transition. The procedure for the TPA transition of odd state is the same as for even state transition.

As mentioned in Section 2.2, the wave-functions of the conduction band of even states are given by:

$$\psi_{j,M}^{c+}(r) = f_C(r)^+(\sqrt{\frac{j+M}{2j}}Y_{j-1/2,M-1/2}(\theta,\varphi)u_{1/2}^c + \sqrt{\frac{j-M}{2j}}Y_{j-1/2,M+1/2}(\theta,\varphi)u_{-1/2}^c)$$
$$= f_C(r)^+(\sqrt{\frac{l+m+1}{2l+1}}Y_{l,m}(\theta,\varphi)u_{1/2}^c + \sqrt{\frac{l-m+1}{2l+1}}Y_{l,m}(\theta,\varphi)u_{-1/2}^c)$$
$$= f_C(r)^+(C_1 \cdot Y_{l,m}(\theta,\varphi)u_{1/2}^c + C_2 \cdot Y_{l,m}(\theta,\varphi)u_{-1/2}^c)$$

(2.26)

The wave-functions of the heavy-hole band of even states are as follows:

$$\psi_{j,M}^{hh+}(r) = f_{hh}^+(r)(A'\cdot Y_{j-3/2,M-3/2}\cdot u_{3/2,3/2}^v + B'\cdot Y_{j-3/2,M-1/2}\cdot u_{3/2,1/2}^v$$
$$+ C'\cdot Y_{j-3/2,M+1/2}\cdot u_{3/2,-1/2}^v + D'\cdot Y_{j-3/2,M+3/2}\cdot u_{3/2,-3/2}^v)$$
$$= f_{hh}^+(r)(HH_1\cdot Y_{l,m}\cdot u_{3/2,3/2}^v + HH_2\cdot Y_{l,m}\cdot u_{3/2,1/2}^v + HH_3\cdot Y_{l,m}\cdot u_{3/2,-1/2}^v + HH_4\cdot Y_{l,m}\cdot u_{3/2,-3/2}^v)$$

(2.27)

where:

$$HH_1 = \frac{-\sqrt{(l+m+3)(l+m+2)(l+m+1)}}{\sqrt{(2l+3)(2l+2)(2l+1)}}$$

$$HH_2 = \frac{i\sqrt{3(l-m+1)(l+m+2)(l+m+1)}}{\sqrt{(2l+3)(2l+2)(2l+1)}}$$

$$HH_3 = \frac{\sqrt{3(l+m+1)(l-m)(l-m+1)}}{\sqrt{(2l+3)(2l+2)(2l+1)}}$$

$$HH_4 = \frac{-i\sqrt{(l-m+3)(l-m+2)(l-m+1)}}{\sqrt{(2l+3)(2l+2)(2l+1)}} \qquad (2.28)$$

The wave-functions of the light-hole band of even states are given below:

$$\psi_{j,M}^{lh+}(r) = f_{lh}^+(r)(E'\cdot Y_{j+1/2,M-3/2}\cdot u_{3/2,3/2}^v + F'\cdot Y_{j+1/2,M-1/2}\cdot u_{3/2,1/2}^v$$
$$+ G'\cdot Y_{j+1/2,M+1/2}\cdot u_{3/2,-1/2}^v + H'\cdot Y_{j+1/2,M+3/2}\cdot u_{3/2,-3/2}^v)$$
$$= f_{lh}^+(r)(LH_1\cdot Y_{l,m}\cdot u_{3/2,3/2}^v + LH_2\cdot Y_{l,m}\cdot u_{3/2,1/2}^v + LH_3\cdot Y_{l,m}\cdot u_{3/2,-1/2}^v + LH_4\cdot Y_{l,m}\cdot u_{3/2,-3/2}^v)$$

(2.29)

where:

$$LH_1 = \sqrt{\frac{3(l+m+1)(l-m-1)(l-m)}{(2l-1)(2l+1)(2l+2)}}$$

$$LH_2 = i(l+3m+1)\sqrt{\frac{l-m}{(2l-1)(2l+1)(2l+2)}}$$

$$LH_3 = (l-3m+1)\sqrt{\frac{l+m}{(2l-1)(2l+1)(2l+2)}}$$

$$LH_4 = i\sqrt{\frac{3(l-m+1)(l+m-1)(l+m)}{(2l-1)(2l+1)(2l+2)}} \tag{2.30}$$

The wave-functions of the spin-split hole band of even states are as follows:

$$\begin{aligned}
&\psi_{j,M}^{sh+}(r) = f_{sh}(r)^+(\sqrt{\frac{j-M+1}{2j+1}}Y_{j+1/2,M-1/2}(\theta,\varphi)u_{1/2,1/2}^{sh} - i\sqrt{\frac{j+M+1}{2(j+1)}}Y_{j+1/2,M+1/2}(\theta,\varphi)u_{1/2,-1/2}^{sh}) \\
&= f_{sh}(r)^+(\sqrt{\frac{l-m}{2l+1}}Y_{l,m}(\theta,\varphi)u_{1/2,1/2} - i\sqrt{\frac{l+m}{2l+1}}Y_{l,m}(\theta,\varphi)u_{1/2,-1/2}) \\
&= f_{sh}(r)^+(SH_1 \cdot Y_{l,m}(\theta,\varphi)u_{1/2,1/2} + SH_2 \cdot Y_{l,m}(\theta,\varphi)u_{1/2,-1/2})
\end{aligned} \tag{2.31}$$

2.3.2.1 Interband transition matrix

For interband transitions under the dipole approximation, the transition is:

$$\begin{aligned}
&< c,b'|V|h,b > = < f_{n',l'}(r)Y_{l',m'}(\theta,\varphi)u^c \,|V|\, f_{n,l}(r)Y_{l,m}(\theta,\varphi)u^v > \\
&= < f_{n',l'}(r)Y_{l',m'}(\theta,\varphi)|\, f_{n,l}(r)Y_{l,m}(\theta,\varphi) >< u^c \,|V|\, u^v > \\
&+ < f_{n',l'}(r)Y_{l',m'}(\theta,\varphi)|V|\, f_{n,l}(r)Y_{l,m}(\theta,\varphi) >< u^c \,|\, u^v > \\
&= < f_{n',l'}(r)Y_{l',m'}(\theta,\varphi)|\, f_{n,l}(r)Y_{l,m}(\theta,\varphi) >< u^c \,|V|\, u^v >
\end{aligned} \tag{2.32}$$

where

$$\begin{aligned}
V &= \frac{A}{m_0 c}\hat{e}\cdot\hat{p} = (e_x p_x + e_y p_y + e_z p_z) \\
&= \frac{A}{m_0 c}\frac{1}{\sqrt{2}}(e_x + ie_y)\cdot\frac{1}{\sqrt{2}}(p_x - ip_y) + \frac{1}{\sqrt{2}}(e_x - ie_y)\cdot\frac{1}{\sqrt{2}}(p_x + ip_y) + e_z p_z \\
&= \frac{A}{m_0 c}(e_{+1}p_- + e_{-1}\cdot p_+ + e_z p_z)
\end{aligned}$$

where m_0 is the free electron mass, A is the amplitude of the light vector. The

matrix elements of interband transition are then determined by the following expression:

$$< c,b'|V|hh,b > = i < f_c^+ | f_{hh}^+ > \delta_{l',l}\delta_{m',m} \frac{P}{\sqrt{3}} \frac{eA}{\hbar c} \begin{pmatrix} C_1 \cdot HH_1 \cdot \sqrt{3}e_{+1} & 0 & C_1 \cdot HH_3 \cdot \sqrt{2}e_0 & C_1 \cdot HH_4 \cdot e_{-1} \\ 0 & C_2 \cdot HH_2 \cdot \sqrt{3}e_{-1} & C_2 \cdot HH_3 \cdot e_{+1} & C_2 \cdot HH_4 \cdot \sqrt{2}e_0 \end{pmatrix} \tag{2.33}$$

$$< c,b'|V|lh,b > = i < f_c^+ | f_{lh}^+ > \delta_{l',l}\delta_{m',m} \frac{P}{\sqrt{3}} \frac{eA}{\hbar c} \begin{pmatrix} C_1 \cdot lH_1 \cdot \sqrt{3}e_{+1} & 0 & C_1 \cdot lH_3 \cdot \sqrt{2}e_0 & C_1 \cdot lH_4 \cdot e_{-1} \\ 0 & C_2 \cdot lH_2 \cdot \sqrt{3}e_{-1} & C_2 \cdot lH_3 \cdot e_{+1} & C_2 \cdot lH_4 \cdot \sqrt{2}e_0 \end{pmatrix} \tag{2.34}$$

$$< c,b'|V|sh,b > = i < f_c^+ | f_{sh}^+ > \delta_{l',l}\delta_{m',m} \frac{P}{\sqrt{3}} \frac{eA}{\hbar c} \begin{pmatrix} C_1 \cdot SH_1 \cdot -e_0 & C_1 \cdot SH_2 - \sqrt{2}e_{-1} \\ C_2 \cdot SH_1 \sqrt{2}e_{+1} & C_2 \cdot SH_2 \cdot e_0 \end{pmatrix} \tag{2.35}$$

where $P = \hbar p_{ch} / m_0 = \hbar^2 < S | \partial / \partial z | Z > / m_0$, and p_{ch} is the interband matrix element of the electron momentum.

2.3.2.2 Intraband transition matrix

It is known from Equations (2.20) to (2.25) that the envelop wave function of conduction band is:

$$f_{nl}^C(r) = \sum_{t=1}^{3} CC_{tnl} j_l(k_t r) \tag{2.36}$$

where *CC* is a constant. So the intraband transition matrix for conduction band is given below:

$$
\begin{aligned}
&< c,b'|V|c,b > \\
&=< f_C^{'}(r)^{+}(C_1 \cdot Y_{l',m'}(\theta,\varphi)u_{1/2}^{c} + C_2 \cdot Y_{l',m'}(\theta,\varphi)u_{-1/2}^{c})\,|V|\, f_C(r)^{+}(C_1 \cdot Y_{l,m}(\theta,\varphi)u_{1/2}^{c} + C_2 \cdot Y_{l,m}(\theta,\varphi)u_{-1/2}^{c}) \\
&= (|C_1|^2 + |C_2|^2) < f_C^{'}(r)^{+} Y_{l',m'}(\theta,\varphi)\,|V|\, f_C(r)^{+} Y_{l,m}(\theta,\varphi) > \\
&= (|C_1|^2 + |C_2|^2)\sum_{t'=1}^{3}\sum_{t=1}^{3} < CC_{t'n'l'} j_{l'}(k_{t'}r)Y_{l'm'}\,|V|\, CC_{tnl} j_l(k_t r)Y_{lm} > \\
&= (|C_1|^2 + |C_2|^2)\sum_{t'=1}^{3}\sum_{t=1}^{3} CC_{t'n'l'} \cdot CC_{tnl} \cdot < j_{l'}(k_{t'}r)Y_{l'm'}\,|V|\, j_l(k_t r)Y_{lm} > \\
&= (|C_1|^2 + |C_2|^2)(-i\frac{e\hbar A}{cm_c})\sum_{t'=1}^{3}\sum_{t=1}^{3} CC_{t'n'l'} \cdot CC_{tnl} \cdot \sum_{p=0,\pm1}(-1)^p e_p V_{b'b}^{(p)}
\end{aligned}
\tag{2.37}
$$

$$
V_{b';b}^{(p)} = -\frac{2}{R}\frac{k_{t'} \cdot k_t \cdot D_{b';b}^{(p)}}{(k_{t'}^2 - k_t^2)\sqrt{(2l+1)(2l'+1)}}
$$

$$
D_{b';b}^{(\pm1)} = \frac{\delta_{m',m\pm1}}{\sqrt{2}}[\delta_{l',l+1}\sqrt{(l'\pm m)(l \pm m + 2)} - \delta_{l',l-1}\sqrt{(l'\mp m)(l \mp m)}]
$$

$$
D_{b';b}^{(0)} = \delta_{m',m\pm1}(\delta_{l',l+1}\sqrt{l'^2 - m^2} - \delta_{l',l-1}\sqrt{l^2 - m^2}) \tag{2.38}
$$

$$
\begin{aligned}
&\sum_{m,m'}|< c,b'|V|c,b >|^2 = (|C_1|^2 + |C_2|^2)^2(-\frac{e\hbar A}{cm_c})^2\frac{1}{3}\,|\sum_{t'=1}^{3}\sum_{t=1}^{3} CC_{t'n'l'} \cdot CC_{tnl} \cdot \{k_t \cdot \frac{a}{k_{t'}^2 - k_t^2} \cdot \\
&[k_{t'}J_{l'}(k_t a)J_{l'+1}(k_{t'}a) - k_t J_{l'}(k_{t'}a)J_{l'+1}(k_t a)]\cdot|^2 \cdot (l_1\delta_{l1,l0+1} + l_0\delta_{l1,l0+1})
\end{aligned}
\tag{2.39}
$$

For the same procedure, the intraband transition for heavy-hole, light-hole and spin-split-hole are given by Equation (2.33), (2.34), and (2.35) respectively:

$$
\begin{aligned}
&\sum_{m,m'}|< hh,b'|V|hh,b >|^2 = (|HH_1|^2 + |HH_2|^2 + |HH_3|^2 + |HH_4|^2)^2 \cdot \frac{-1}{3} \cdot (\frac{e\hbar A}{cm_{hh}})^2 \cdot \\
&|\sum_{t'=1}^{4}\sum_{t=1}^{4} CHH_{t'n'l'} \cdot CHH_{tnl} \cdot \{k_t \cdot \frac{a}{k_{t'}^2 - k_t^2} \cdot \\
&[k_{t'}J_{l'}(k_t a)J_{l'+1}(k_{t'}a) - k_t J_{l'}(k_{t'}a)J_{l'+1}(k_t a)]\cdot|^2 \cdot (l_1\delta_{l1,l0+1} + l_0\delta_{l1,l0+1})
\end{aligned}
\tag{2.40}
$$

$$\sum_{m,m'}|< lh,b'|V|lh,b>|^2=(|LH_1|^2+|LH_2|^2+|LH_3|^2+|LH_4|^2)^2\cdot\frac{-1}{3}\cdot(\frac{e\hbar A}{cm_{hh}})^2\cdot$$
$$|\sum_{t'=1}^{4}\sum_{t=1}^{4}CLH_{t'n'l'}\cdot CLH_{tnl}\cdot\{k_t\cdot\frac{a}{k_{t'}^2-k_t^2}\cdot$$
$$[k_{t'}J_{l'}(k_ta)J_{l'+1}(k_{t'}a)-k_tJ_{l'}(k_{t'}a)J_{l'+1}(k_ta)]\cdot|^2\cdot(l_1\delta_{l1,l0+1}+l_0\delta_{l1,l0+1})$$

(2.41)

$$\sum_{m,m'}|< sh,b'|V|sh,b>|^2=(|SH_1|^2+|SH_2|^2+|SH_3|^2+|SH_4|^2)^2\cdot\frac{-1}{3}(\frac{e\hbar A}{cm_{hh}})^2\cdot$$
$$|\sum_{t'=1}^{4}\sum_{t=1}^{4}CSH_{t'n'l'}\cdot CSH_{tnl}\cdot\{k_t\cdot\frac{a}{k_{t'}^2-k_t^2}\cdot$$
$$[k_{t'}J_{l'}(k_ta)J_{l'+1}(k_{t'}a)-k_tJ_{l'}(k_{t'}a)J_{l'+1}(k_ta)]\cdot|^2\cdot(l_1\delta_{l1,l0+1}+l_0\delta_{l1,l0+1})$$

(2.42)

Combining the interband transition and intraband transition matrix, the two-photon transition rate of heavy-hole to conduction band is given by Equation (2.43)

$$W_{hh}^{(2)}=\frac{16\pi P^2}{9\hbar}\cdot(\frac{eA}{c})^2\{(3\cdot C_1^2\cdot HH_1^2+3\cdot C_2^2\cdot HH_2^2+C_2^2\cdot HH_3^2+C_1^2\cdot HH_4^2)\cdot\frac{1}{4}\}$$
$$+(C_1^2\cdot HH_3^2+C_2^2\cdot HH_4^2)\cdot\frac{1}{6}\}\cdot\{(|HH_1|^2+|HH_2|^2+|HH_3|^2+|HH_4|^2)^2\cdot$$
$$|\sum_{t'=1}^{4}\sum_{t=1}^{4}CHH_{t'n'l'}\cdot CHH_{tnl}\cdot(k_t\cdot\frac{a}{k_{t'}^2-k_t^2}\cdot$$
$$(k_{t'}J_{l'}(k_ta)J_{l'+1}(k_{t'}a)-k_tJ_{l'}(k_{t'}a)J_{l'+1}(k_ta))\cdot|^2\cdot(l_1\delta_{l1,l0+1}+l_0\delta_{l1,l0+1})+|\sum_{t'=1}^{3}\sum_{t=1}^{3}CC_{t'n'l'}\cdot CC_{tnl}\cdot$$
$$(k_t\cdot\frac{a}{k_{t'}^2-k_t^2}\cdot(k_{t'}J_{l'}(k_ta)J_{l'+1}(k_{t'}a)-k_tJ_{l'}(k_{t'}a)J_{l'+1}(k_ta))\cdot|^2\cdot(l_1\delta_{l1,l0+1}+l_0\delta_{l1,l0+1})\}$$

(2.43)

The procedure will be the same for the two-photon transition of light-hole to conduction band $W_{lh}^{(2)}$, and spin-orbit split hole bands to the conduction band $W_{so}^{(2)}$. Then the two-photon absorption coefficient is given below:

$$\beta=\int\frac{2\hbar\omega}{I^2}(W_{hh}^{(2)}+W_{lh}^{(2)}+W_{so}^{(2)})dR \qquad (2.44)$$

Based on the above discussions, TPA coefficient, β, can be theorized quantitatively. The results will be presented in Chapter 5.

REFERENCES:

[2.1] N. W. Ashcroft and N. D. Mermin, *Solid State Physics*, (Holt, Rinehart & Winston, New York, 1976).

[2.2] F. Bassani and G. P. Parravicini, *Electronic States and Optical Transitions in Solids,* (Pergamon, Oxford, UK, 1975).

[2.3] A. L. Efros, and A. Efros, Sov. Phys. Semicond. **16**, 772 (1982).

[2.4] L. Brus, J. Chem. Phys. **79**, 5566 (1983).

[2.5] L. E. Brus, J. Chem. Phys. **80**, 4403 (1984).

[2.6] E. O. Kane, J. Phys. Chem. Solids **1**, 249 (1957).

[2.7] E. O. Kane, "The $k \cdot p$ method", Chapter 3, in R. K. Willardson and A. C. Beer, Eds., *Semiconductors and Semimetals, Vol. 1,* (Academic, New York, 1966).

[2.8] J. M. Luttinger and W. Kohn, Phys. Rev. **97**, 869 (1955).

[2.9] C. R. Pidgeon and R. N. Brown, Physical Review **146**, 575 (1966).

[2.10] J. B. Xia, Phys. Rev. **40**, 8500 (1989).

[2.11] Y. Z. Hu, S. W. Koch, and D. B. T.Thoai, Mod. Phys. Lett. B **4**, 1009 (1990).

[2.12] V. I. Klimov, "Linear and Nonlinear Optical spectraoscopy of Semiconductor Nanocrystals," in "*Handbook of Nanostructured Materials and Nanotechnology, vol. 4: Optical Properties,*" p563-p639 (Academic Press, Inc., 2000).

[2.13] A. V. Fedorov, A. V. Baranov, and K. Inoue, Phys. Rev. B **54**, 8627 (1996).

[2.14] L. A. Padilha, J. Fu, D. J. Hagan, and E. W. V. Stryland, Opt. Express **13**, 6460 (2005).

[2.15] L. A. Padilha, J. Fu, D. J. Hagan, E. W. Van Stryland, C. L. Cesar, L. C. Barbosa, C. H. B. Cruz, D. Buso, and A. Martucci, Phys. Rev. B **75**, 075325 (2007).

[2.16] K. I. Kang, B. P. McGinnis, Sandalphon, Y. Z. Hu, S. W. Koch, N. Peyghambarian, A. Mysyrowicz, L. C. Liu, and S. H. Risbud, Phys. Rev. B **45**, 3465 (1992).

[2.17] P. C. Sercel and K. J. Vahala, Phys. Rev. B **42**, 3690 (1990).

[2.18] J. Bardeen, J. Chem. Phys. **6**, 367 (1938).

[2.19] F. Seitz, The Modern Theory of Solids, p352. (McGraw Hill, New York, 1940).

[2.20] S. L. Chuang, *Physics of Optoelectronic Devices*, (John Wiley & Sons, Inc., 1995).

[2.21] P. C. Sercel and K. J. Vahala, Phys. Rev. B **42**, 3690 (1990).

[2.22] K. J. Vahala and P. C. Sercel, Phys. Rev. Lett. **65,** 239 (1990).

[2.23] Al. L. Efros and M. Rosen, Phys. Rev. B **58**, 7120 (1998).

[2.24] A. R. Edmonds, *Angular Momentum in Quantum Mechanics*, (Princeton NJ: Princeton Univ. Press, 1957).

[2.25] B. S. Wherrett, J. Opt. Soc. Am. B **1**, 67 (1984).

Chapter III

EXPERIMENTAL TECHNIQUES AND THEORETICAL ANALYSES

3.1 Introduction

A large number of experimental techniques have been applied to the research reported in this thesis. Among these techniques, two experimental techniques are essential and thus are described in detail in this chapter: the open-aperture Z-scan technique and the femtosecond time-resolved, frequency-degenerate, pump-probe technique (the latter is also referred as the transient absorption measurement technique). These two techniques have been applied to our study on the optical nonlinearity and ultrafast dynamics of quantum dots (QDs), respectively. In addition, many other techniques have also been applied to facilitate the investigation of the QDs. These techniques include steady-state UV-vis absorption spectroscopy, photoluminescence (PL) spectroscopy, high-resolution transmission electron microscopy (HRTEM), and energy dispersion X-ray (EDX) analysis. These techniques have been utilized to obtain the optical properties, PL position and width, QDs' lattice structure as well as dot size and size distribution, and the element ratio. The operational principles and working details of these techniques are well-developed and documented as in Ref. [3.1]. Therefore, they are not

described here, although they have been frequently employed in the research project presented in this thesis.

In the following sections, the Z-scan technique and the femosecond time-resolved, frequency-degenerate, pump-probe technique will be covered from their experimental set-up to their theoretical analyses. The laser systems used in the experiments are also described.

3.2 The Z-scan technique

3.2.1 Introduction to the Z-scan technique

The nonlinear optical properties of materials are important to many applications such as optical communications, optical information processing, bio-imaging and targeting. Thus, the characterization of these properties in materials has been a very active field for past decades. Many experimental techniques has been proposed and utilized. Among them are nonlinear interferometry [3.2, 3.3], degenerate four-wave mixing [3.4], nearly degenerate three-wave mixing [3.5], ellipse rotation [3.6], and beam distortion measurement [3.7]. These techniques, with different advantages, have the shortcoming of requiring either relatively complex apparatus or detailed wave propagation analysis.

The Z-scan technique was proposed by Van Stryland's group in 1990 [3.8]. It is a simple yet highly sensitive technique to measure the nonlinear optical coefficients based on the transmittance as a function of z position. In

this technique, the sample moves along the axis of a focused laser beam through its focal plane and the transmission of the sample is measured for each *z* position, this technique is called Z-scan technique. The diagram of the Z-scan set-up is shown in Fig. 3.1 (a). The incoming laser light is first split by a beam splitter. The reflected light is recorded by detector one (D_1) as a reference. The transmitted light is focused by a lens and the power of the transmitted light passing through the sample is measured by detector two (D_2). Then the information of the nonlinearity then can be derived from the ratio of D_2 to D_1 as a function of the position *z*. With or without an aperture in front of D_2, the nonlinear refraction or nonlinear absorption can be extracted by fitting the Z-scan theory to the measured data. This method is thus called open-aperture Z-scan and closed-aperture Z-scan for these two conditions, respectively. Despite the simplicity in its set-up and operation, this technique allows the determination of the sign and magnitude of nonlinear absorption and/or nonlinear refraction at the same time and thus has been widely accepted since its invention.

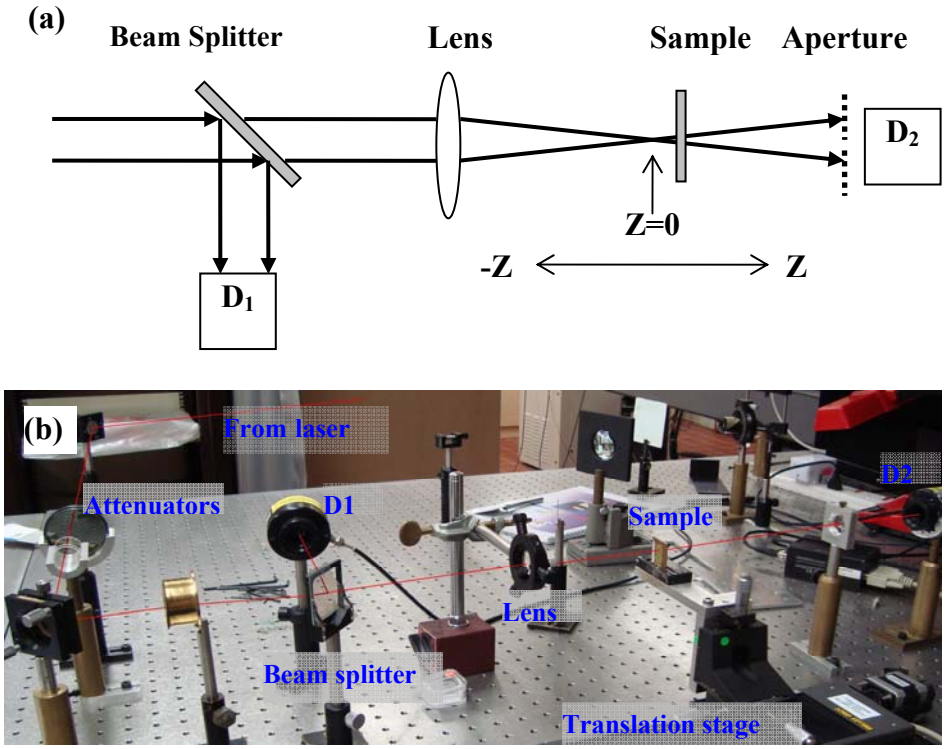

Fig. 3.1 (a) Schematic diagram of the Z-scan set-up. It is the open-aperture Z-scan set-up if there is no aperture in front of D2. It is the closed-aperture Z-scan set-up if there is an aperture in front of D2, as showed with the doted line. (b) Photograph of the Z-scan experimental set-up in our lab. The energy ratio of D_2/D_1 is recorded as a function of the sample position z. D_1 and D_2 are the detectors. The sample is mounted on a translation stage which is controlled by a computer. Note that the aperture is absent in our experiment and thus it is the open aperture Z-scan set-up.

Fig. 3.1 (b) shows the photograph of the open-aperture Z-scan set-up in our laboratory. The detectors in this set-up are silicon-based detectors (Model RKP465) which were purchased from Laser Probe Inc. The spectral sensitive range is from 200 nm to 1100 nm with a detection area of 10 mm x 10 mm.

In a third-order instantaneous nonlinear optical material, the nonlinear refraction and nonlinear absorption are related to the real part and imaginary part of the third- order nonlinear optical susceptibility $\chi^{(3)}$ respectively. The total refractive index and total absorption coefficient can be expressed by [3.8]:

$$n = n_0 + n_2 I \tag{3.1}$$

$$\alpha = \alpha_0 + \beta I \tag{3.2}$$

with the nonlinear absorption and refraction can be expressed by βI and $n_2 I$, respectively; I refers to the light irradiance; β is the third order nonlinear absorption (*TPA* coefficient); and n_2 is the third order nonlinear refractive index. Fig. 3.2 illustrates the normalized Z-scan curves for different conditions: Fig. 3.2 (a) and (b) show the open-aperture Z-scan and closed-aperture Z-scan with pure nonlinear absorption and pure nonlinear refraction, respectively. From Fig. 3.2 (a) it can be seen that the signal is a symmetric 'peak' or 'valley' with respect to the Z position for the open-aperture Z-scan. These two conditions correspond to the nonlinear bleaching (β<0) and nonlinear absorption (β >0) respectively. From Fig. 3.2 (b), the signal with pure nonlinear refraction has a peak followed a valley (n_2<0) or a valley followed by a peak (n_2>0). Figs. 3.2 (c) and (d) display the closed-aperture Z-scan curves with the coexistence of both nonlinear absorption and refraction. It can be seen that the sign of the nonlinear absorption and/or refraction can be

conveniently determined from the shape of the curve. Fig. 3.2 (c) demonstrates by the closed-aperture Z-scan curves coexistence of nonlinear absorption β >0 with nonlinear refractive index n_2>0 (solid line) and n_2<0 (dash-dot line), respectively; and Fig. 3.2 (d) exhibits the coexistence of nonlinear absorption β<0 and nonlinear refractive index, n_2>0 (solid line) and n_2<0 (dash-dot line), respectively.

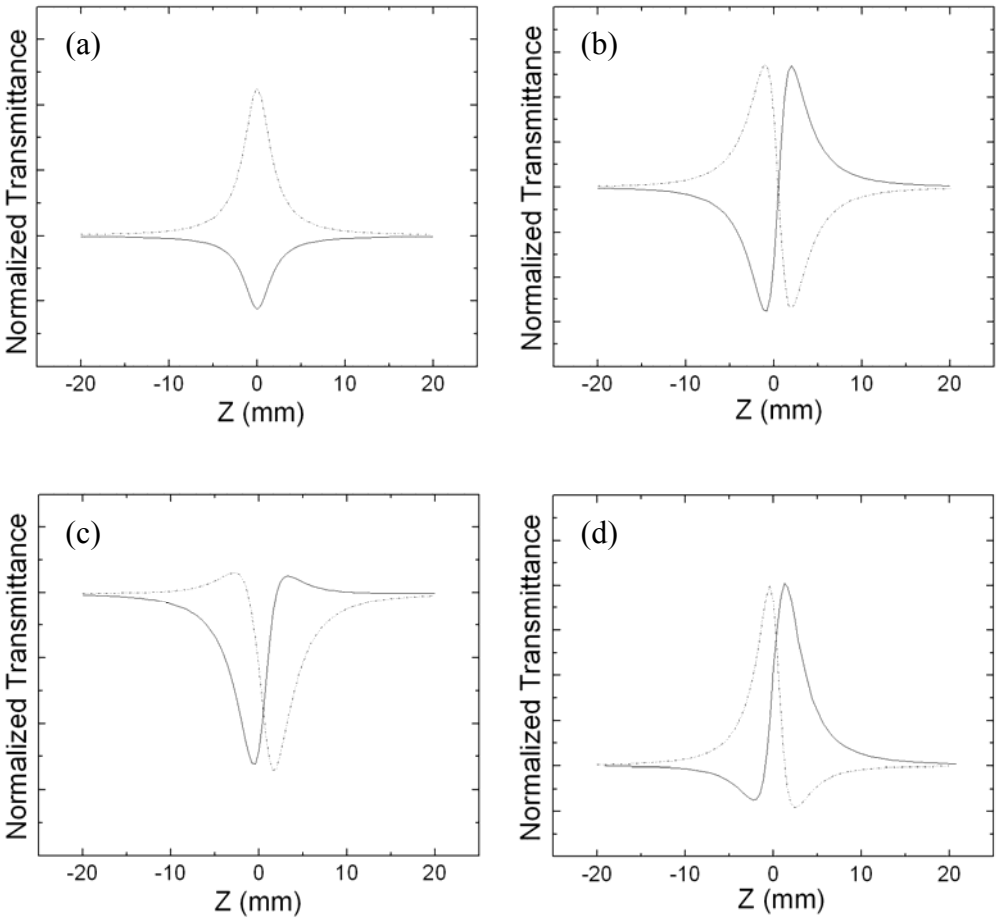

Fig. 3.2 Illustration of the normalized Z-scan transmittance curves for (a) pure nonlinear absorption: β>0 (solid line), β<0 (dash-dot line); (b) pure nonlinear refraction: n_2>0 (solid line), n_2<0 (dash-dot line); (c) β>0, n_2>0 (solid line); β>0, n_2<0 (dash-dot line); and (d) β<0, n_2>0 (solid line); β<0, n_2<0 (dash-dot line).

In this thesis, only the open-aperture Z-scan has been applied to investigate the imaginary part of third order nonlinearity especially related to two-photon absorption in the QDs.

It should be pointed out that the Z-scan set-up has to be calibrated before conducting the measurements on any samples. There are two purposes in this calibration: one is to check the alignment of the optical path; and the other is to assure the accuracy of the detectors. The pulse duration can be acquired through the autocorrelation method. In our study, the Z-scan set-up was calibrated by using bulk crystals such as CdS and CdTe as standard samples.

To illustrate the above calibration, Fig. 3.3 shows an example of using 0.5-mm-thick hexagonal CdS bulk crystal (Semiconductor Wafer, Inc.) to calibrate the open-aperture Z-scan set-up at 780 nm. Firstly, from Fig. 3.3 (a) we obtain that the signals are symmetric about the origin of the Z axis, which indicates a good alignment of the optical path. Secondly, from fitting the Z-scan curves with parameters of beam waist w_0, the pulsed duration τ_p, laser power, P, etc, the TPA coefficient can be derived. From the comparison between the TPA coefficients obtaining from fitting Z-scan curves and from theoretical prediction [3.9], the parameters of the Z-scan set-up can be confirmed.

As mentioned in Chapter I, there are two absorption processes at higher irradiance, that is, TPA and TPA-generated excited-state absorption. To distinguish the contributions from TPA and the TPA-generated excited-state absorption, the Z-scans have to be performed with several laser irradiances. At low laser irradiances where only TPA dominates, the measured TPA coefficients derived from the Z-scan curves should be independent of the irradiances. As can be seen from 3.3 (b) that at intensities below 1.4 $GWcm^{-2}$, the TPA coefficient remains the same and thus the TPA process should be the dominant process in the Z-scan curves in this intensity range. The TPA coefficient is then can be determined. The TPA-generated excited-state absorption should be considered only whenever the measured TPA coefficients show irradiance-dependence. Meanwhile, during the measurement, the sample may experience damage due to the strong laser pulse. The experiments have to be performed from lower irradiance to higher irradiance and to lower irradiance again. The signals should be repeatable to make sure that the sample is undamaged by the laser beam. Furthermore, for QDs dissolved in solvent, Z-scans should be conducted in a period of time in order to make sure that there is no measurable difference and to ensure the long-term stability.

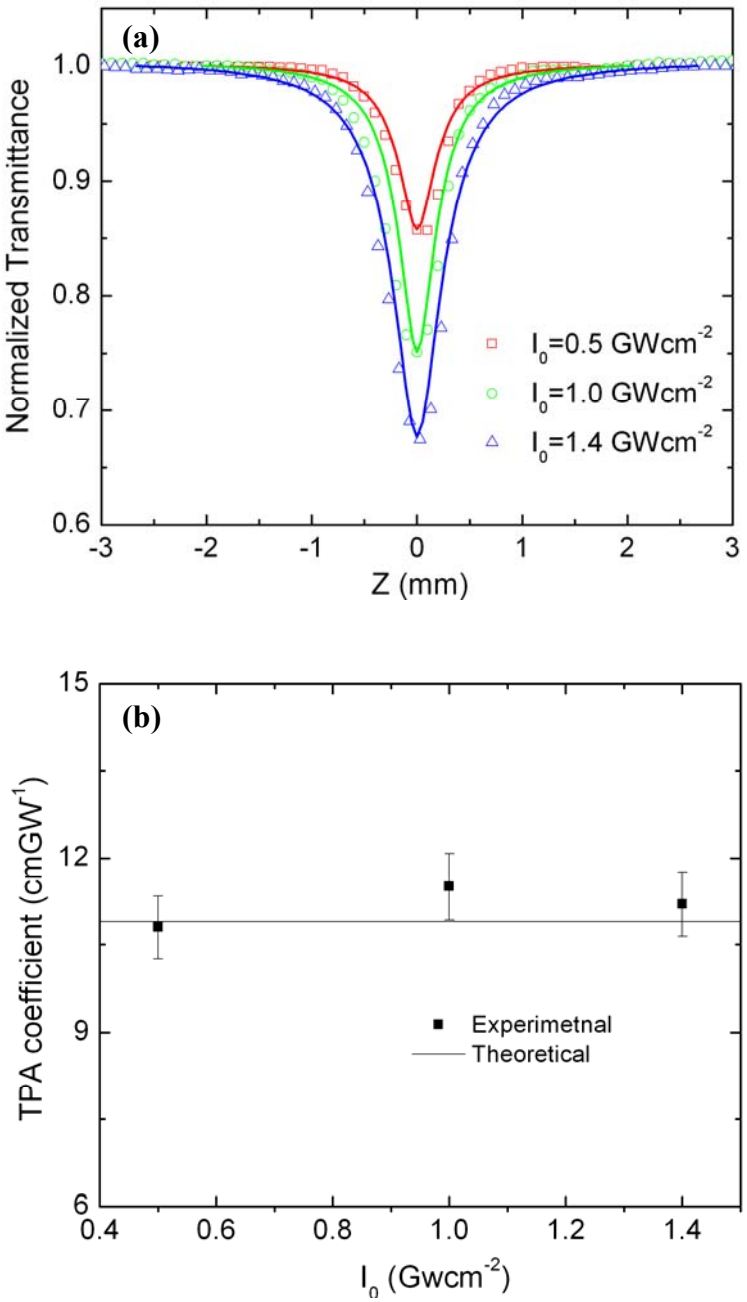

Fig. 3.3 (a) Open-aperture Z-scan curves for bulk CdS at 780 nm at different laser intensities. (b) The TPA coefficients vs laser intensity for bulk CdS at 780 nm. The solid square represents the experimental data whereas the line represents the theoretical calculation based on Ref. [3.9].

3.2.2 Theoretical analysis for TPA coefficient measured with open-aperture Z-scan technique

For the TPA process, the TPA coefficient can be derived by the following equation:

$$\frac{dI(r,t,z)}{dz} = -[\alpha_0 + \beta I(r,t,z)]I(r,t,z), \tag{3.3}$$

which describes losses in the laser beam due to the single- and two-photon absorption when it propagates within the two-photon absorber, α_0 is the single-photon absorption coefficient and β is the TPA coefficient. I is the laser irradiance, which is a function of the radial position, r, Z-position, z, and time, t. Considering the laser beam as Gaussian in both the temporal and spatial domain: $I(r,t,z) = I(z)\exp(-2r^2/w^2(z))\exp(-t^2/\tau_p^2)$, and by solving Eqn. (3.3), the open-aperture Z-scan curve *T(z)* is then given by:

$$T(z) = \frac{C}{\sqrt{\pi} q_0} \int_{-\infty}^{\infty} \ln(1 + q_0 \exp(-x^2))dx \tag{3.4}$$

where $q_0 = \beta I_0 L_{eff}/(1+z^2/z_0^2)$, I_0 is the laser beam intensity at the focus without the sample, z_0 is the diffraction length of the laser beam, defined by $z_0 = \pi\omega_0^2/\lambda$, where ω_0 denotes the beam waist at the focus and λ is the wavelength of the laser beam. L_{eff} is the effective thickness calculated according to: $L_{eff} = [1-\exp(-\alpha_0 L)]/\alpha_0$.

At low laser intensities, the TPA coefficient β obtained through Eqn. (3.4) can be regarded as being independent of the intensity of the laser beam. However, at high intensities, the contribution of intraband absorption cannot be neglected. As described in Chapter I, when the laser beam intensity is sufficiently large, the carriers excited by two-photon excitation may make transitions to higher excited states by absorbing more incoming photons simultaneously with the two-photon absorption. In this case, the reduction in the laser intensity *I*, is given by

$$\frac{dI(r,t,z)}{dz} = -[\alpha_0 + \beta I(r,t,z) + \sigma_\alpha N]I(r,t,z) \tag{3.5}$$

and

$$dN/dt = \beta I^2/(2\hbar\omega) - N/\tau_{eff} \tag{3.6}$$

where, σ_α is the intraband absorption cross-section of TPA-excited carriers; τ_{eff} is the effective lifetime for TPA-excited carriers which is normally much longer compared with the laser pulse duration and can be neglected. The Eqn. (3.5) and Eqn. (3.6) are solved with a numerical method [3.10].

3.3 The pump-probe technique

3.3.1 Introduction to the pump-probe technique

Another important technique used in this thesis is the femtosecond time-resolved, frequency-degenerate, pump-probe technique. For short, it is also called the pump-probe technique or transient absorption measurement.

Fig. 3.4 shows a photograph and the corresponding schematic diagram of the set-up. As can be seen, the laser pulses are firstly divided by a beam splitter into two parts. The first part is the stronger part, which is called pump beam, and it is delayed and chopped before being focused into the sample. Behind the sample, this particular beam is blocked. The second part is the weaker beam (probe beam), which is focused to the sample and its transmitted light is detected by a sensitive photodiode. In the pump-probe technique, the pump-induced absorption change is determined as a function of the time delay τ between the pump and probe pulses. The change in the pump intensity can be obtained through changing a number of attenuators, which are inserted in the way of the pump beam before being focused into the sample. Using this method, the ultrafast decay dynamics after excitation can be investigated. In Fig. 3.4, there is a zero-order $\lambda/2$ wave plate as well as a linear polarizer in the path of the probe. Both optical element are used to control and change the polarization of the probe light and make the probe light to be perpendicular with respect to the polarization of the pump light. In the crossed polarization of pump and probe, artificial signals from any coherent effects can be eliminated.

The wavelengths of the pump and the probe are the same for the experiments carried out in this thesis. The technique is thus called the frequency-degenerate pump-probe technique.

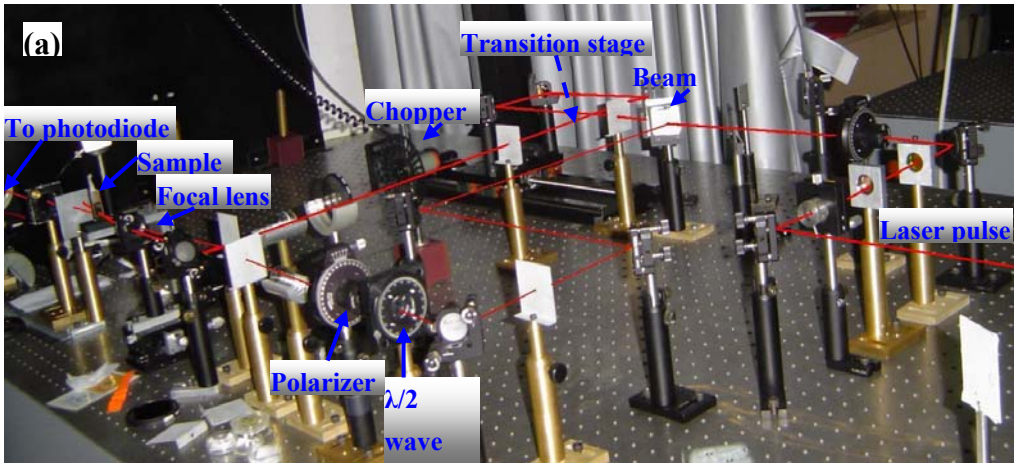

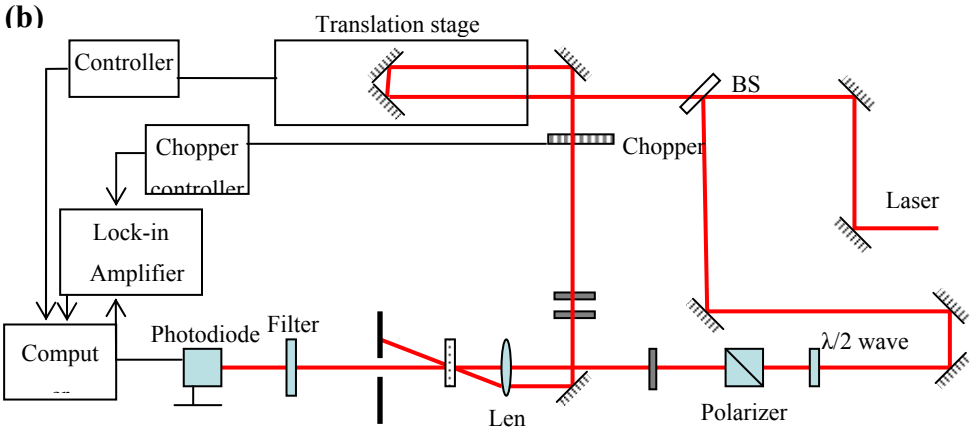

Fig. 3.4 (a) Photograph of the frequency-degenerate pump-probe set-up; (b) Diagram of the frequency-degenerate pump-probe set-up corresponds to the photo. The detector or photodiode after the sample measures the transmission of the probe pulse in the presence (T) and absence (T_0) of the pump pulse. The polarization of the probe pulse is rotated with respect to that of the pump pulse using a zero-order λ/2 plate and a linear polarizer.

As mentioned above, in the pump-probe set-up, the requirement on the two pulses are as follows: (1) the intensity of pump beam is so stronger than that of the probe beam that the influence of the latter onto the material can be neglected; (2) the polarizations of the two pulses are perpendicular to each other to get rid of the "coherent artifact" on the transient signal. It should be noted that the second requirement is not a "must" requirement; it is just for the convenience of the experimental analysis.

It should be noted that in all the experimental conditions here, we used the intra-band transitions to study the dynamics of the excited carriers. That is, the photon energy of the probe beam is not enough to excite the electrons from the ground states but can only excite the 'free carriers' excited by the pump beam through two-photon transition.

Fig. 3.5 demonstrates the schematic diagram of the process by the pump and probe beams. Fig. 3.5(a) shows the pump process with TPA to excite the material. After being excited by the pump pulses, the excited carriers are further excited by the probe beam through intra-band transitions. The process in (b) presents at $\tau = 0$ the free carriers excited through absorbing another photon. The process in (c) shows a very fast relaxation to the bottom of the conduction band through carrier-carrier collision or thermalization. The process in (d) illustrates the excited carriers are being excited by intra-band absorption of the probe pulse, whereby the probe is detected at $t > \tau_p$ with τ_p being the pulse width of the pump beam.

As the in Z-scan experiment, calibration has to be made with standard bulk materials before performing pump-probe measurements. Furthermore, cautions have also to be made to avoid laser-induced damage on the samples during the measurement.

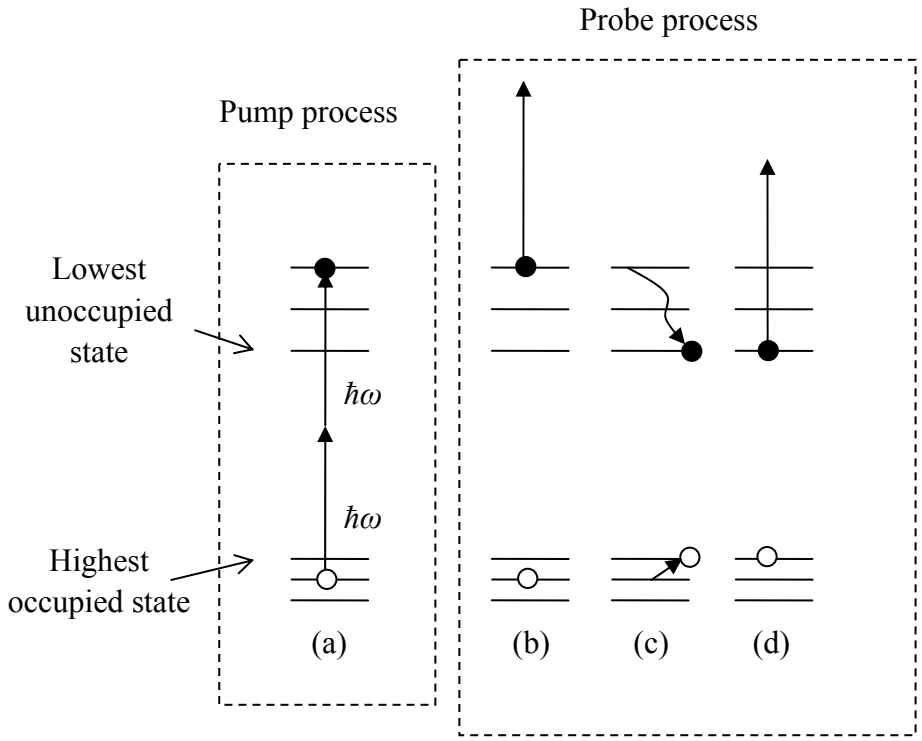

Fig.3.5 Schematic diagram of processes in frequency-degenerate pump-probe detection; (a) is the excitation with TPA to excite the material; (b) represents the condition at $\tau = 0$; (c) in a short time, the excited carriers relax down to the ground excitation states; and (d) the probe detection at $\tau > \tau_p$ with τ_p being the pulse width of the pump beam.

3.3.2 Theoretical analysis for the pump-probe technique

As mentioned above, the mechanism in the pump-probe detection in this thesis is the intraband absorption. After being excited by the pump pulses, the excited carriers can be further excited by the probe beam. The intensity of the probe beam I_{pr} can be expressed as:

$$\frac{dI_{pr}}{dz} = -\alpha_0 I_{pr} - \sigma_\alpha N(t) I_{pr} \tag{3.7}$$

where σ_α is the absorption cross-section of the excited carriers, *N(t)* is the number density of the excited carriers, α_0 is the linear absorption coefficient of the ground state of the material. In our frequency-degenerate pump-probe technique, the energy of one photon is not enough for the electron to be excited from the valence band to the conduction band. In this case, α_0 can be ignored. Eqn. (3.7) can be simplified as:

$$\frac{dI_{pr}}{dz} = -\sigma_\alpha N(t) I_{pr} \tag{3.8}$$

Considering the reflection on both sides of sample, the probe intensity after transmitting through the sample is:

$$I_{pr} = I_{pr0}(1-R)^2 \exp[-N(t)\sigma_\alpha L] \tag{3.9}$$

The transmittance of the probe beam without (T_0) and with (T) the presence of the pump beam is as follows:

$$T_0 = I_{pr} / I_{pr0} = (1-R)^2 \tag{3.10}$$

and

$$T = I_{pr} / I_{pr0} = (1-R)^2 \exp[-N(t)\sigma_\alpha L] \quad (3.11)$$

From the above two equations, it is easy to get the number density of the excited carriers *N(t)*:

$$N(t) = -\ln(T/T_0)/\sigma_\alpha L \quad (3.12)$$

From Eqn. (3.7) to (3.12), it is obvious that the dynamics of the carriers excited by the pump can be monitored by the probe beam through the term of $-\ln(T/T_0)$.

Frequently used method to analyze the pump-probe data is using the negative differential transmittance of peak (*NDTP*):

$$NDTP = \frac{T - T_0}{T_0} = \exp[-N(t)\sigma_\alpha L] - 1 \quad (3.13)$$

When $N(t)\sigma_\alpha L$ is small enough, the *NDTP* can be further expressed by Taylor expansion:

$$NDTP = -\Delta T / T_0 = -N(t)\sigma_\alpha L \quad (3.14)$$

From Eqn. (3.14), the excited carrier density *N(t)* is proportional to $-\Delta T / T_0$. In this thesis, Eqn. (3.14) has been applied for analyzing the pump-probe signal in dynamics study.

3.4 The laser systems

In this thesis, all the experiments were performed with two femtosecond laser systems. The first one was the Quantronix laser system which includes three parts: (1) a pump laser (Quantronix, Darwin) at 527 nm; (2) an amplifier laser: a Ti: Sapphire regenerative amplifier (Quantronix, Titan), with the oscillator inside and being pumped by the Darwin laser. The output is at 780 nm with a repetition rate of 1-kHz, the full width at half maximum pulse width is around 230 fs; and (3) an optical parametric amplifier (Quantronix, TOPAS) pumped by the Ti: Sapphire regenerative amplifier (Quantronix, Titan) at 1-kHz repetition rate. The TOPAS generates the tunable wavelength laser pulses from 500 nm to 1550 nm. The intensity or power of the laser output is controlled by transmitting through a set of neutral density filters. Fig. 3.6 shows a photograph of this Quantronix laser system.

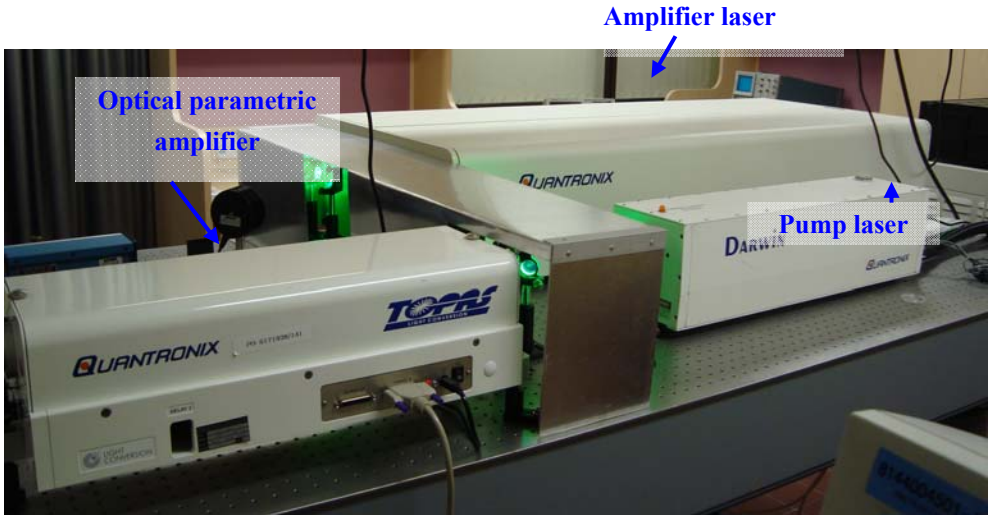

Fig. 3.6 Photograph of Quantronix laser system.

The second laser system is a mode-locked Ti: Sapphire laser (Coherent, Chameleon) operated at 86-MHz repetition rate. The wavelength is tunable from 720 nm to 950 nm. The pulse duration of laser pulses in full width at half maximum varied from 150 to 98 fs, depending on the laser wavelength.

REFERENCES

[3.1] Stanley L. Flegler, John W. Heckman, Jr. Karen L. Klomparens, *Scanning and transmission electron microscopy: an introduction*, (New York: W. H. Freeman 1993).

[3.2] M. J. Weber, D. Milam, and W. L. Smith, Opt. Eng. **17**, 463 (1978).

[3.3] M. J. Moran, C. Y. She, and R. L. Carman, IEEE J. Quantum Electron. **OE-11**, 259 (1975).

[3.4] S. R. Friberg and P. W. Smith, IEEE J. Quantum Electron. **23**, 2089 (1987).

[3.5] R. Adair, L. L. Chase, and S. A. Payne, J. Opt. Soc. AM. B **4**, 875 (1987).

[3.6] A. Owyoung, IEEE J. Quantum Electron. **QE-9**, 1064 (1973).

[3.7] W. E. Williams, M. J. Soileau, and E. W. Van Stryland, Opt. Commun. **50**, 256 (1984).

[3.8] M. Sheik-Bahae, A. A. Said, T. H. Wei, D. J. Hagan, E. W. V. Styland, IEEE, J. Quantum Electronics **26**, 760 (1990).

[3.9] E. W. V. Styland, M. A. Woodall, H. Vanherzeele, and M. J. Soileau, Optics Letter **10,** 490 (1985).

[3.10] R. L. Sutherland, *Handbook of Nonlinear Optics*, p542, p528, p530 (Marcel Dekker, Inc., New York, 1996).

Chapter IV

TWO-PHOTON EXCITATION AND RELAXATION IN CdSe QUANTUM DOTS

4.1 Introduction

Recently, fluorescent semiconductor nanocrystal quantum dots (QDs) have received tremendous attention due to their applications to two-photon microscopy [4.1-4.4]. In such applications, radiative recombination of electron-hole (e-h) pairs, that are created by two-photon absorption (TPA), is leading in three-dimensional imaging, which has been reported to revolutionize bio-imaging technology. A better understanding of two-photon excitation and relaxation processes therefore has important technological implications. In particular, studies should be carried out to gain insights into dynamical mechanisms which lead to a saturation in the overall efficiency of TPA-excited fluorescence (*i.e.* the ratio of the number of fluorescent photons to the total number of incoming photons). Such saturation has been observed [4.4]. Here a systematical study is presented of both Auger recombination and intraband absorption of TPA-excited carriers in colloidal CdSe QDs, which contribute to saturation of TPA-excited fluorescence at high laser intensities.

Auger recombination, quantized Auger rate, and intraband absorption of two-photon-excited carriers in colloidal CdSe QDs have been investigated systematically with femtosecond Z-scans and transient absorption measurements. The Auger constant is revealed to be of the order of $\sim 10^{-30} cm^6 s^{-1}$, while the intraband absorption cross-sections are found to be in the range from 10^{-18} to 10^{-17} cm^2. Our experimental evidence demonstrates that the Auger recombination or the intraband absorption takes place under the condition that the average electron-hole pair per quantum dot is larger than unity.

Furthermore, we have also analyzed the intraband absorption of TPA-excited carriers in colloidal QDs. Following two-photon excitation, an excited carrier (electron or hole) may undergo as transition to a higher energy state by absorbing another incoming photon, a similar process to the so-called free-carrier absorption in bulk semiconductors. This process makes no contribution to the generation of e-h pairs in QDs yet consumes a large fraction of incoming photons, providing another channel for deteriorating the overall efficiency of TPA-excited fluorescence at high laser intensities. Though the intraband absorption of TPA-excited carriers has been investigated in bulk semiconductors, similar effects in colloidal QDs have been largely overlooked.

As illustrated in Fig. 4.1, the Auger process, in which an e-h pair is annihilated and another carrier (electron or hole) is excited to a higher energy level, may take place after two-photon excitation. The Auger process is more efficient due to enhanced carrier-carrier interaction in the confined space of QDs in comparison with bulk materials [4.5-4.7]. Auger recombination occurs as excited e-h pairs in a QD exceed unity; and the energy released is not emitted as a photon, but is used to excite another carrier to a higher energy level. As a result, a reduction in the overall efficiency of TPA-excited fluorescence becomes considerably large at high excitation. Although Auger recombination of one-photon-excited carriers in colloidal QDs has been studied intensively, no report is available in the literature for the case of two-photon excitation, where the laser intensity is much larger than that used for one-photon excitation.

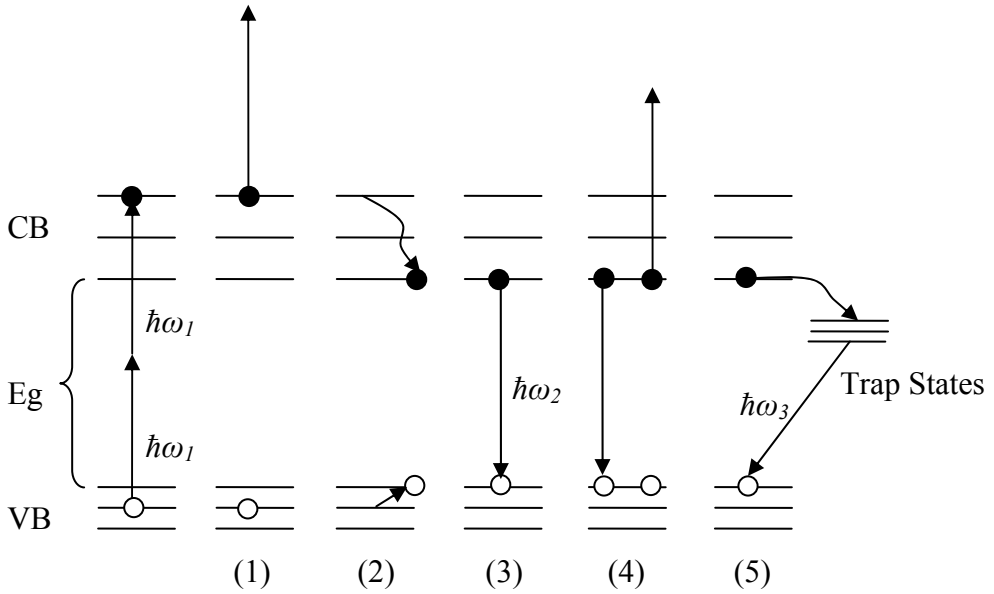

Fig. 4.1 Relaxation pathways of electron-hole pairs in QDs. The excited electrons and holes may experience several pathways: (1) the absorption of another photon, called intraband absorption; (2) firstly relax to the lowest excited exciting states in a very quick time scale, and the excited electron-hole pair may then recombine together, the energy released may either (3) emit as a photon, or, (4) excite another electron or hole to even higher states (Auger process). (5) the excited electron may also be trapped to trap states before recombining with the hole.

In the following experiments, the colloidal CdSe QDs in water enclosed in a 1-mm-thick quartz cuvette were investigated with 120-fs laser pulses. The wavelength tunable laser pulses were generated by an optical parametric amplifier (Quantronix, TOPS), which was pumped by a Ti: Sapphire regenerative amplifier (Quantronix, Titan) at 1-kHz repetition rate. The laser pulse energy was controlled via transmission through a set of neutral density filters.

4.2 Synthesis and characterization of CdSe quantum dots

The QDs studied here are semiconductor nanocrystal CdSe QDs coated with a layer of glutathione (GSH). The synthesis of GSH-capped CdSe QDs was based on the reaction of cadmium chloride with sodium hydroselenide (NaHSe). NaHSe was prepared by the reduction of selenium powder with sodium borohydride. Freshly generated NaHSe was injected into a solution containing $CdCl_2$ and glutathione at pH 11.5 with vigorous stirring. The amounts of Cd, Se and GSH were 5, 2 and 6 mmol, respectively, in a total volume of 500 ml. The resulting light yellow mixture was heated to 95^{o}C for 6 hours, and the growth of GSH-capped CdSe QDs was stopped when the fluorescence of the QDs changed to green. The prepared QDs were precipitated with an equivalent amount of 2-propanol, then redissolved in water and precipitated with 2-propanol for three more times. The pellet of QDs was dried at room temperature in vacuum overnight, and the final product in the powder form could be re-dissolved in water.

Fig. 4.2 (a) shows the schematic representation of the synthesis process of CdSe/GSH QDs and Fig. 4.2 (b) is an anatomic indication of the structure of this sample.

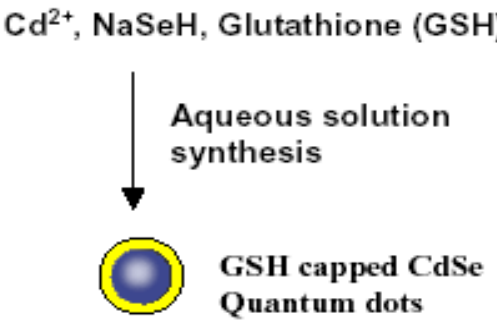

(a)

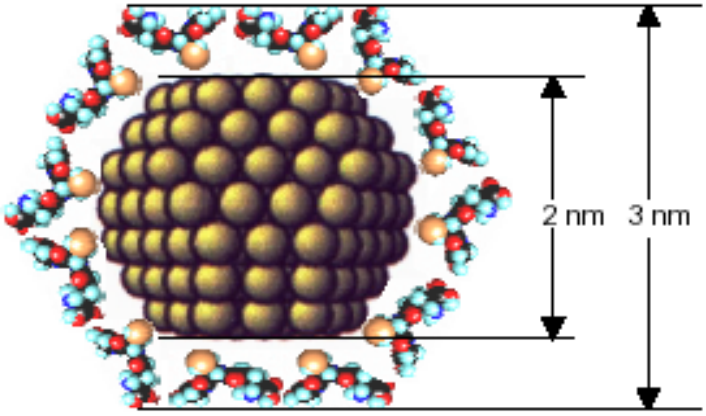

(b)

Fig. 4.2 (a) Schematic indication of the synthesis process of CdSe/GSH QDs; and (b) anatomic indication of the structure of CdSe/GSH QDs.

The high-resolution TEM (HRTEM) image in Fig. 4.3 (a) shows both the dimension and crystalline structure of the QDs, which are 2.2 nm in diameter on average. Fig 4.3 (b) shows the size distribution. The size deviation is revealed to be 18 % with a Gaussian fitting to the size distribution.

To investigate the structure of these CdSe/GSH QDs, the XRD spectrum was recorded as shown in Fig. 4.4 (solid line). In order to figure out the position of peaks, the XRD spectrum was fitted with Gaussian curves as shown with the dashed lines. From the fitting of the XRD data in Fig. 4.4, the CdSe core is revealed to have the zinc blend cubic structure.

Fig. 4.5 displays the spectra of one-photon absorption and one-photon-excited photoluminescence (PL) for the CdSe QDs in aqueous solution. In the absorption spectrum, there is a clear presence of several excitonic transitions. The electronic structures of CdSe QDs have been investigated extensively, and there are several theories available in the literature [4.8, 4.9]. Based on the theoretical calculation reported in Ref. 4.9, we find that our measured absorption spectrum can be fitted well by accounting of several excitonic transitions with Gaussian broadening which correspond to the size dispersion mentioned above. The details of the excitonic transitions involved in the calculation are specified in Fig. 4.5. The lowest excitonic transition is at 2.45 eV for CdSe QDs of 2.2-nm diameter, consistent with the experimental finding of Ref. 4.10. A blue shift of 750-meV is found in when compared to the band-gap energy of CdSe bulk crystal. The PL

spectrum shows that the band-edge emission is centered at 2.36 eV with a full width at half maximum of ~200 meV.

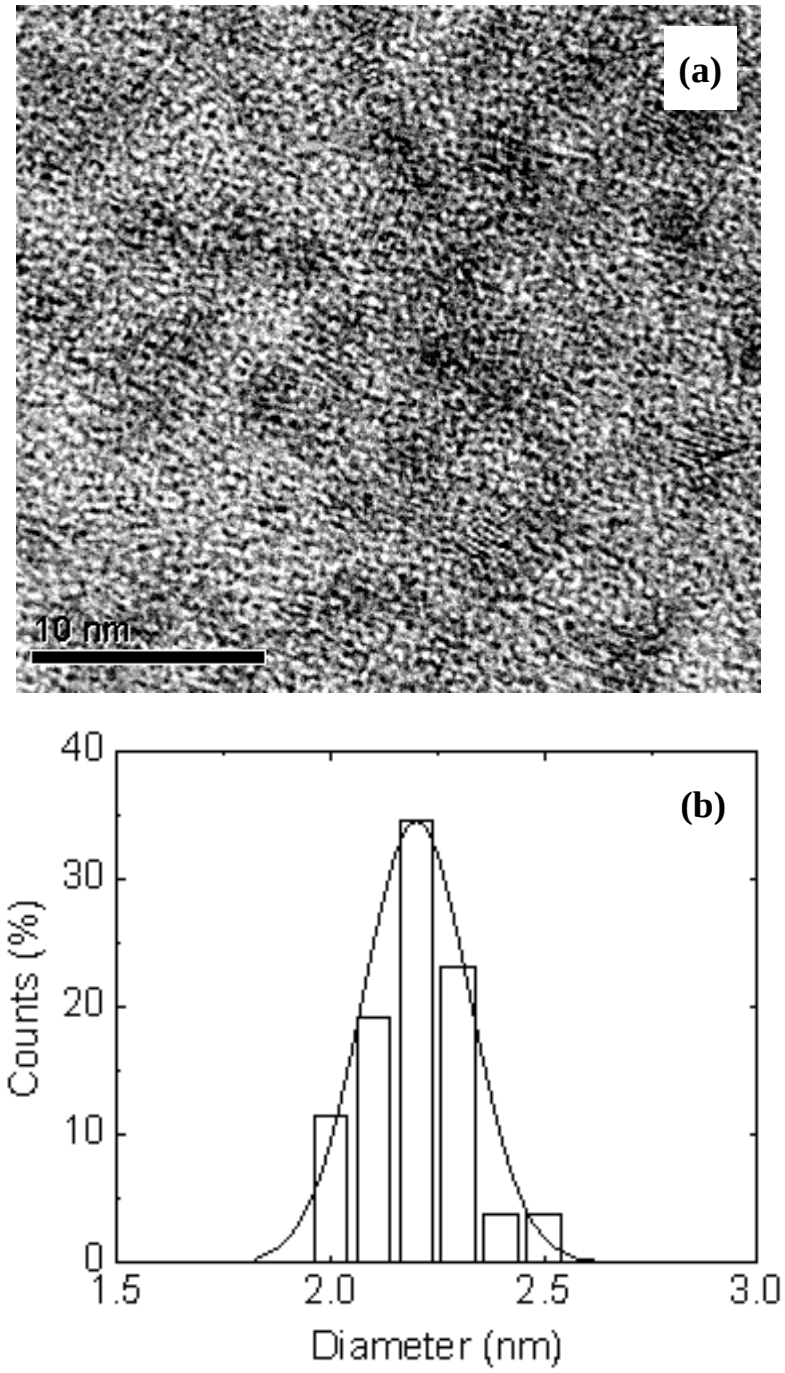

Fig. 4.3 (a) High-resolution TEM image of GSH-capped CdSe/GSH Quantum Dots; and (b) Size distribution of CdSe/GSH. The solid line is a Gaussian fitting to the size distribution.

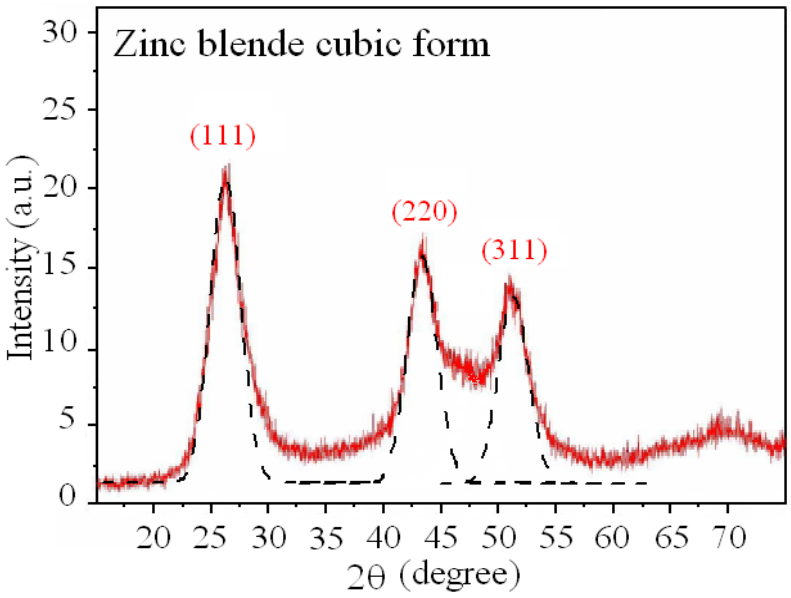

Fig. 4.4 XRD spectrum (solid line) of the quantum dots. The dashed line is the fitting with Gaussian curves.

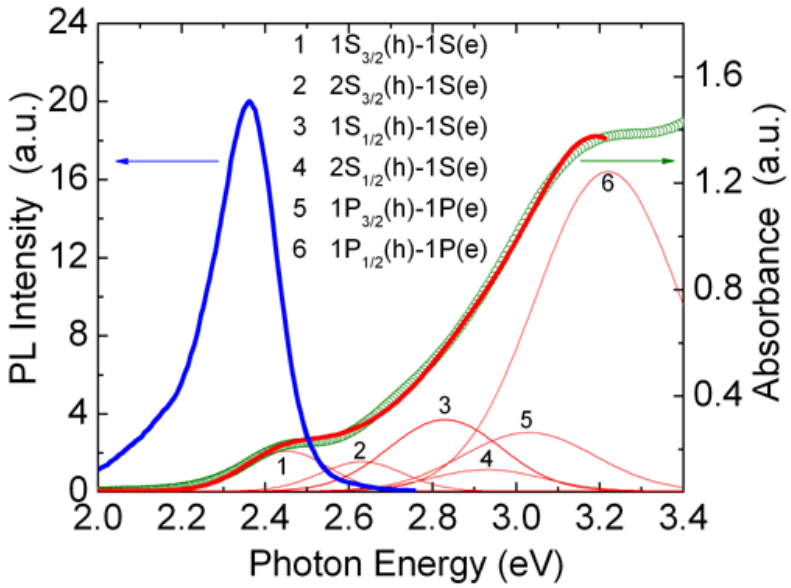

Fig. 4.5 Spectra of the one-photon absorption (circle) and one-photon- excited photoluminescence excited at 350 nm (solid line) for the quantum dots in aqueous solution. The dashed curves are the theoretical fits.

4.3 TPA coefficients in CdSe quantum dots.

For our open-aperture Z-scans, the laser pulses were focused with a minimum beam waist of 12 ~ 16 μm, depending on the laser wavelength. With 120-fs pulse duration and low pulse repetition rate (1 *K*Hz), nonlinear absorption resulting from laser heating was found to be insignificant. All the measurements discussed below were conducted at room temperature.

As mentioned in the beginning of this chapter, there maybe many dynamic processes following high laser excitation. To exclude the effect of intraband absorption, the transient absorption measurement was performed to reveal the laser intensity range where only the TPA is pre-dominant.

In our transient absorption measurement, a cross-polarized, pump-probe configuration was utilized. With the cross-polarized configuration, any "coherent artifact" on the transient absorption was eliminated. The pump-probe measurements in Fig. 4.6 demonstrate transient absorption signals with different intensities, the solid curves are the decay fitting curves whereas the dashed curve is the autocorrelation between the pump and probe pulses with the magnitude dominated by the TPA and intraband absorption. The TPA is present only with the presence of the pump pulses. At time scales much larger than the duration of pump pulse, the intraband absorption manifests itself on the long 'tail'. From Fig. 4.6, we can see that the intraband absorption effect of TPA-excited carriers is negligible at low pump intensities ($\leq$ 30

$GWcm^{-2}$). Hence, the magnitude of TPA can be determined unambiguously from Z-scans measured under 30 GW/cm^2.

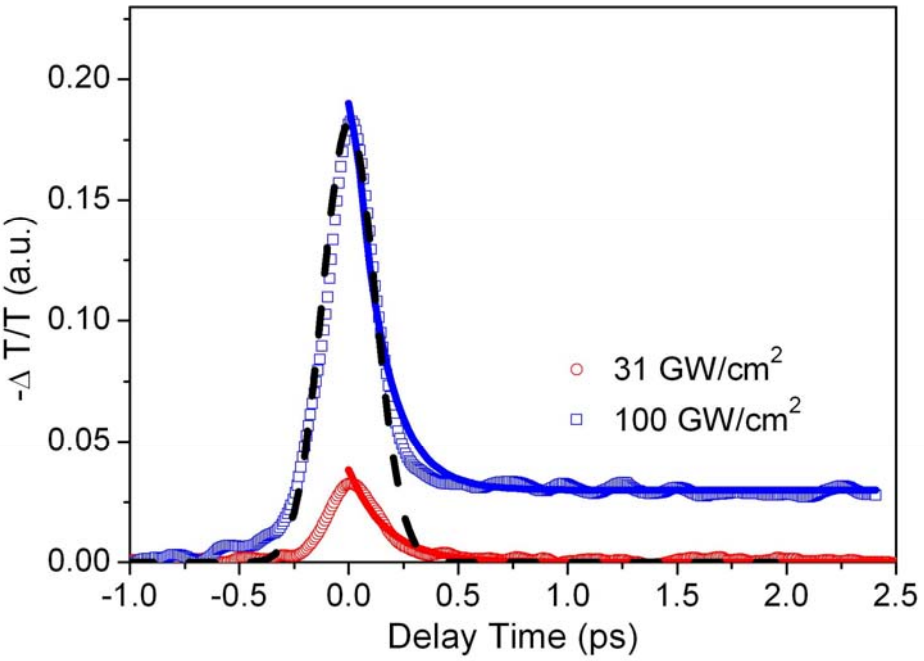

Fig. 4.6 Transient absorption in aqueous solution of GSH-capped CdSe Quantum Dots measured with 120-fs laser pulses at 780-nm wavelength at different intensities. The dashed curve is the autocorrelation between the pump and probe pulse. It can be seen that the intraband absorption can be ignored when the intensity is below 30 $GWcm^{-2}$.

Fig. 4.7 (a) shows the Z-scan curves measured at various wavelengths with laser intensities of 25 GWcm^{-2} or less. With the standard Z-scan theory for pure TPA [4.11], we extract the TPA coefficient of the CdSe QD solution from the best fit between the theoretical simulation and the Z-scan curves. From the TPA coefficient, which is denoted as β, we infer the TPA cross-section by $\sigma_{2PA} = \beta\hbar\omega / N$, where N is the number of QDs per cubic centimeter, and $\hbar\omega$ is the photon energy. We plot σ_{2PA} as a function of $\hbar\omega / E_g$ in Fig. 4.7 (b), showing that σ_{2PA} values are in the range from 3×10^{-47} to $2\times10^{-46} cm^4 s / photon$ with an overall increase as the photon energy increases. The TPA cross-sections of CdSe QDs measured here are comparable to those of ZnS QDs [4.12], and are an order of magnitude larger than those of CdS QDs [4.13]. With two-photon-excitation PL spectroscopy, Larson *et al.* [4.4]. determined the action cross-sections $\phi_f \sigma_{TPA}$ to be of the order of 10^{-47} $cm^4 s / photon$ for colloidal CdSe QDs. If the fluorescence quantum efficiency, ϕ_f, is taken to be 40%, their TPA cross-sections are in agreement with our findings. Theoretical work has performed to calculate the *TPA* cross-sections of CdSe QDs [4.14, 4.15]. The measured TPA spectrum in Fig. 4.7 (b) approaches the theoretical values of Fedorov *et al.* [4.15], but its amplitude is five times smaller than the ones predicted by Schmidt *et al.* [4.14]. It should be emphasized that there is no ambiguity in our measurements, different from previously reported data [4.4, 4.13] which rely on ambiguous values of the fluorescence quantum efficiency.

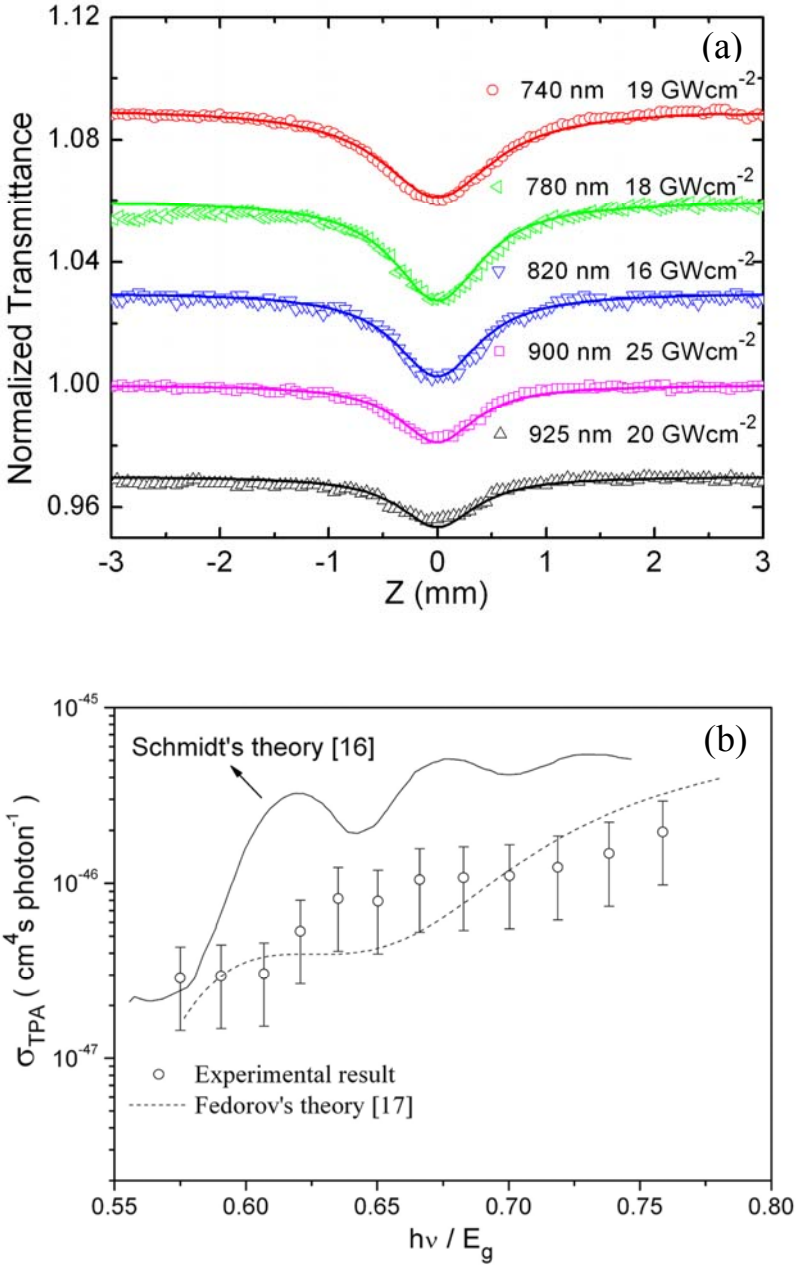

Fig. 4.7 (a) The Z-scans measured at various wavelengths with laser intensities of 25 $GWcm^{-2}$ or less. The solid curves are the fitting curves. (b) Dispersion of the TPA cross-section for GSH-capped CdSe QDs. The solid and dashed curves are the theoretical results.

4.4 Auger process following TPA excitation in CdSe Quantum Dots

With the accurate determination of the TPA coefficient discussed above, we can now precisely calculate the e-h pairs per QD. TPA-excited carrier density, $N_{e\sim h}$, is given by

$$dN_{e\sim h} / dt = \beta I^2 /(2\hbar\omega) - N_{e\sim h} / \tau_{eff} \tag{4.1}$$

where τ_{eff} is the effective lifetime for TPA-excited carriers and can be ignored since it is much longer than the pulse duration discussed later. The density of TPA-excited carriers is given below with assumption that the temporal and spatial profiles of laser pulse are Gaussian functions,

$$N_{e\sim h} = \frac{\beta}{2\hbar\omega}\frac{I_0^2 \tau_G \sqrt{\pi}}{2} \tag{4.2}$$

where τ_G is the half width at 1/e maximum for the pulse duration, and I_0 is on-axis intensity at focus point of the Gaussian beam. With Eqn. (4.2), we can accurately evaluate the average e-h pairs per QD, $< N_0 >= N_{e-h} / N$, for a given pump intensity.

The effects of TPA-excited carriers in the CdSe QDs manifest themselves at pump intensities in excess of 50 GWcm^{-2} ($< N_0 >$ = 0.5). As illustrated in Fig. 4.6, it is evident that, at 100 GWcm^{-2}, a long tail appears in the transient signal, which is attributed to the presence of a significant density of TPA-excited carriers. To study more details, Fig. 4.8 displays the relaxation part of transient absorption signal at different pump intensities. The relaxation process may be described quantitatively by using a three-exponential fitting:

$A_0 e^{-t/\tau_0} + A_1 e^{-t/\tau_1} + A_2 e^{-t/\tau_A}$, where the fastest component, τ_0 , about 0.13 ps, is found to be independent of the pump intensity; and is interpreted as the autocorrelation between the pump and probe pulse [4.16]. The slowest component, τ_1 , on the nanosecond scale is attributed to radiative, band-to-band recombination [4.17]. Note that the third time component τ_A is extremely sensitive to the pump intensity or the average e-h pairs in the QD. As shown in Fig. 4.9, τ_A is 13.5 ps, 25 ps, and 76 ps as $< N_0 >$= 5.4, 2.6 and 1.1, respectively. If $< N_0 >$ is less than 1, it disappears. This is consistent with the quantization of Auger recombination in QDs, which was first observed by Klimov *et al.* [4.5] with one-photon excitation. To quantify it, Klimov *et al.* also developed a model of multiple e-h state decay through quantized step: $dn_N / dt = -n_N / \tau_N$, $dn_{N-1} / dt = -n_{N-1} / \tau_{N-1} + n_N / \tau_N$,…, with the initial conditions for $n_N, n_{N-1}, \ldots n_1$ following Poisson distribution. With this model and the relationship [4.18] of $\tau_i / \tau_2 = (2/i)^2$ (i>2), we extract $\tau_6 = 1.2 ps$, $\tau_5 = 1.7 ps$, $\tau_4 = 2.7 ps$, $\tau_3 = 4.8 ps$, and $\tau_2 = 10.8 ps$ from the decay curves for $< N_0 >$= 5.4, 2.6 and 1.1; and then conclude the Auger constant to be $\sim 1 \times 10^{-30} cm^6 s^{-1}$ which is in the same order of magnitude as the result obtained by Klimov *et al.* with one-photon excitation [4.5].

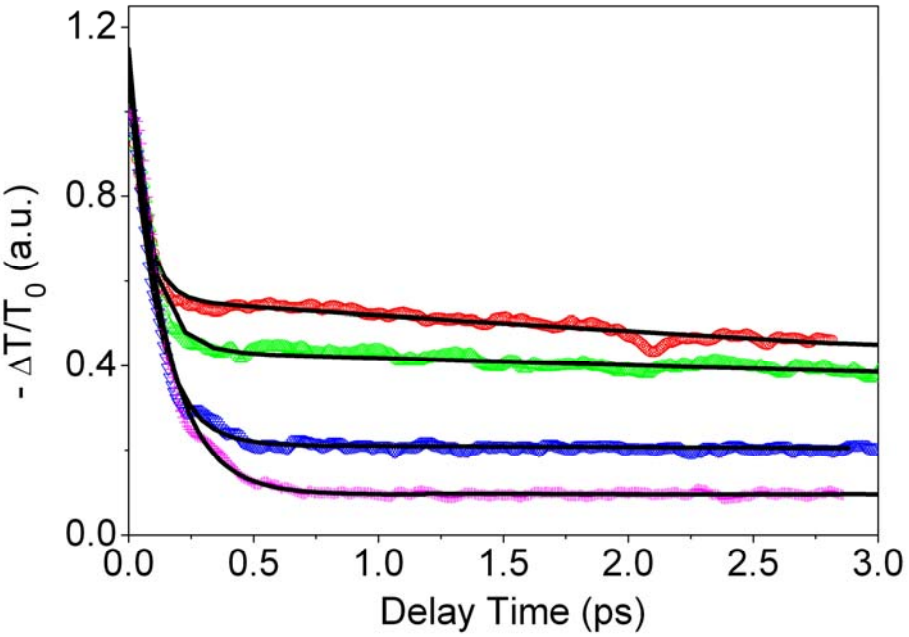

Fig. 4.8 Transient absorption in aqueous solution of GSH-capped CdSe QDs measured with 120-fs laser pulses at 780-nm wavelength. The relaxation processes measured at various pump intensities of 180 GWcm^{-2}, 130 GWcm^{-2}, 80 GWcm^{-2}, and 65 GWcm^{-2} (from the top down). At these pump intensities, two-photon-excited e-h pairs per QD are $\langle N_0 \rangle$ = 5.4, 2.6, 1.1, and 0.7, correspondingly. The solid lines for $\langle N_0 \rangle < 1$ are two-exponential fitting curves with τ_0 = 0.13 ps and τ_1 > 300 ps. The solid lines for $\langle N_0 \rangle > 1$ are fitted using the model of quantized decay step and Poisson distribution for initial states.

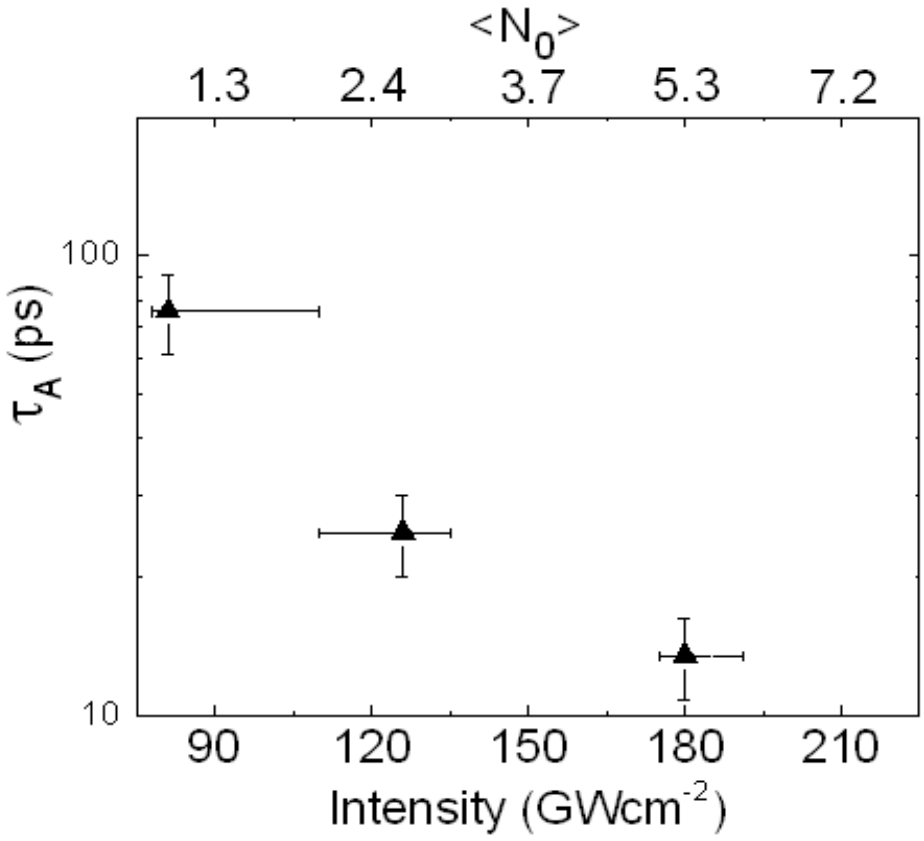

Fig. 4.9 Effective Auger relaxation time *vs*. pump intensity or $\langle N_0 \rangle$. The triangles are the symbols for τ_A.

4.5 Intraband absorption following TPA in CdSe Quantum Dots

In addition to the TPA, the intraband absorption of TPA-excited carriers is also observable by using Z-scans in the regime of high laser intensities. After two-photon excitation, an excited carrier may make transition to higher energy states by absorbing another incoming photon. In this case, the reduction in the laser intensity, *I*, is given by:

$$dI / dz = -(\alpha_0 + \beta I + \sigma_\alpha N_{e\sim h})I \tag{4.3}$$

where α_0 is the linear absorption coefficient, and σ_α is the intraband absorption cross-section of TPA-excited carriers. Since $N_{e\sim h}$ is proportional to the square of the laser intensity, we derive an effective TPA coefficient, which comprises two parts: $\beta_{eff} = \beta + \Delta\beta$ and $\Delta\beta$ is linearly dependent on the laser intensity. Indeed, our Z-scans at high intensities in the Fig. 4.10 (a) permit us to extract the β_{eff} values, and then the plot of β_{eff} vs. I_0 confirms the linear dependence, as illustrated in Fig. 4.10 (b). When $< N_0 > < 1$, the intraband absorption is insignificant and thus β_{eff} is the intrinsic value for the TPA coefficient. By utilizing the Z-scan theory [4.11] with both Eqn. (4.1) and Eqn. (4.3), we simulate the Z-scan data measured at high intensities with σ_α being treated as one free parameter. The best fits allow us to unambiguously determine σ_α to be $\sim 10^{-17} cm^2$ at 780 nm. Similar analytical procedures have been applied to the Z-scans measured at wavelengths ranging from 680 to 760 nm. The wavelength dependence of σ_α is displayed in Fig. 4.11. In general, the intraband absorption increases at longer wavelength. Such a trend is similar to that predicted by Drude's model, but we also observed some discrepancy. Auger processes or surface state trappings occur in the time scale of a few picoseconds or longer. In our Z-scan experiments, we have measured the intraband absorption within 120 fs. Hence, Auger processes, or surface state trappings have little effect on our measurements.

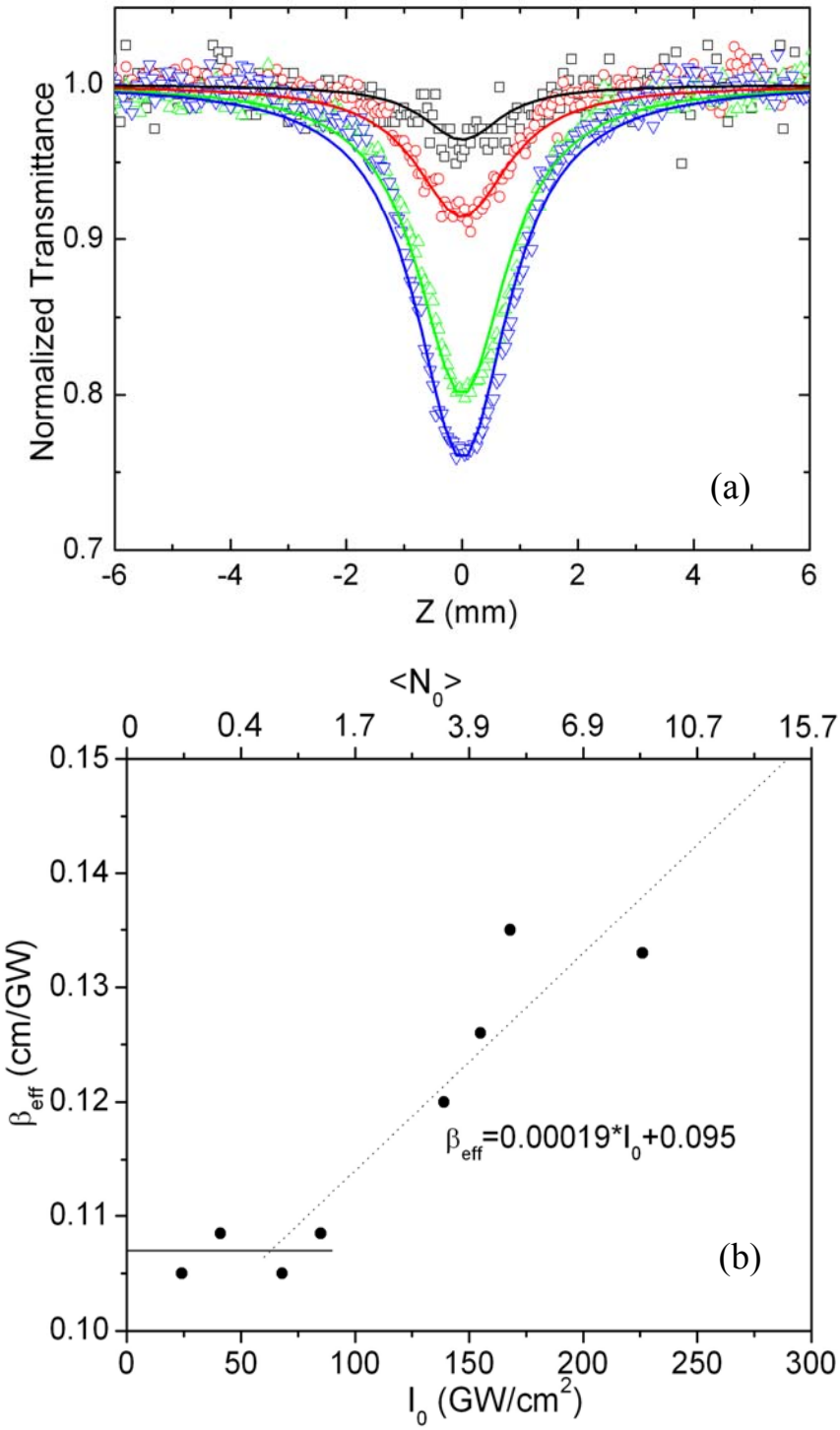

Fig. 4.10 (a) Several Z-scans examples at 780 nm with laser intensities: 24 ; 68 ; 139 ; and 168 $GWcm^{-2}$ (from up down). The solid curves are the fitting curves. (b) Effective TPA coefficient β_{eff} *vs*. laser intensity or $\langle N_0 \rangle$. The filled circles are the extracted β_{eff} values from the Z-scans.

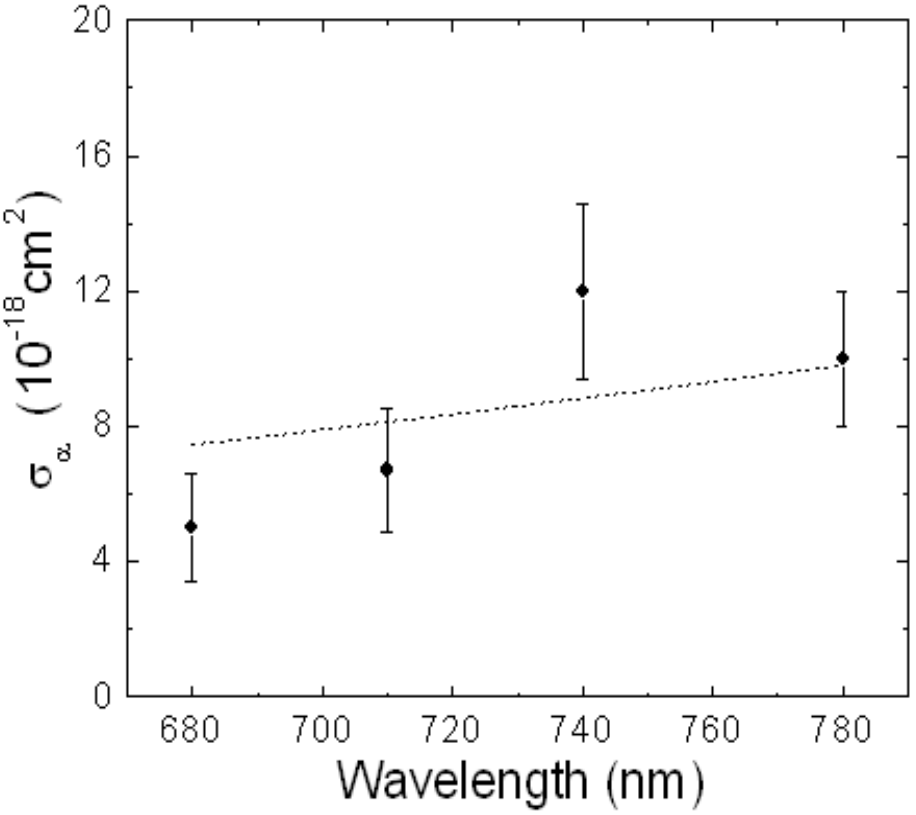

Fig. 4.11 σ_α vs. laser wavelength. The dotted line is the guideline for square dependence on wavelength.

4.6 Conclusions

In summary, Auger recombination, quantized Auger rate, and intraband absorption of TPA-induced carriers in colloidal CdSe QDs have been investigated systematically. Our experimental evidence demonstrates that the Auger recombination or the intraband absorption becomes significant on the condition that the average e-h pair per QD is larger than unity ($< N_0 >=1$). This finding has profound implication to multiphoton microscopic bio-imaging with high pump intensities.

REFERENCES

[4.1] X. Michalet, F. F. Pinaud, L. A. Bentolila, J. M. Tsay, S. Doose, J. J. Li, G. Sundaresan, A. M. Wu, S. S. Gambhir, and S. Weiss, Science **307**, 538 (2005).

[4.2] W. C. W. Chan and S. Nie, Science **281**, 2016 (1998).

[4.3] B. Dubertret, P. Skourides, D. J. Norris, V. Noireaux, A. H. Brivanlou, and A. Libchaber, Science **298**, 1759 (2002).

[4.4] D. R. Larson, W. R. Zipfel, R. M. Williams, S. W. Clark, M. P. Bruchez, F. W. Wise, and W. W. Webb, Science **300**, 1434 (2003).

[4.5] V. I. Klimov, A. A. Mikhailovsky, D. W. McBranch,C. A. Leatherdale, and M. G. Bawendi, Science **287**, 1011 (2000).

[4.6] M. Califano, A. Zunger, and A. Franceschetti, Appl. Phys. Lett. **84**, 2409 (2004).

[4.7] L. W. Wang, M. Califano, A. Zunger, and A. Franceschetti, Phys. Rev. Lett. **91**, 056404 (2003).

[4.8] A. D. Yoffe, Adv in Phys. **50,** 1 (2001) and references therein.

[4.9] A. L. Efros and M. Rosen, Ann. Rev. Mater. Scie. **30**, 475 (2000).

[4.10] V. I. Klimov, J. Phys. Chem. B **104**, 6112 (2000).

[4.11] M. Sheik-Bahae, A. A. Said, T. H. Wei, D. J. Hagan, and E. W. V. Stryland, IEEE, J. Quant. Elect. **26**, 760 (1990).

[4.12] V. V. Nikesh, A. Dharmadhikari, H. Ono, S. Nozaki, G. R. Kumar, and S. Mahamuni, Appl. Phys. Lett. **84**, 4602 (2004).

[4.13] J. W. M. Chon, M. Gu, C. Bullen, and P. Mulvaney, Appl. Phys. Lett. **84**, 4472 (2004).

[4.14] M. E. Schmidt, S. A. Blanton, M. A. Hines, and P. Guyot-Sionnest, Phys. Rev. B **53**, 12629 (1996).

[4.15] A. V. Fedorov, A. V. Baranov, and K. Inoue, Phys. Rev. B **54**, 8627 (1996).

[4.16] E. P. Ippen and C. V. Shank, "*Technique for Measurement*" in "*Ultrashort Light Pulses, Picosecond Techniques and Applications*", edited by S. L. Shapiro, P83-P122 (Spring-Verlag, Berlin, Heidelberg, New York, 1977).

[4.17] C. de Mello Donegá, M. Bode, and A. Meijerink, Phys. Rev. B **74**, 085320 (2006).

[4.18] R. M. Kraus, P. G. Lagoudakis, J. Mü1ller, A. L. Rogach, J. M. Lupton, and J. Feldmann, J. Phys. Chem. B **109**, 18214 (2005).

[4.19] A. A. Said, M. Sheik-Bahae, D. J. Hagan, T. H. Wei, J. Wang, J. Young, and E. W Van Stryland, J. Opt. Soc. Amer. B **9**, 405 (1992).

Chapter V

TPA OF QUANTUM DOTS IN THE REGIME OF VERY STRONG CONFINEMENT: SIZE AND WAVELENGTH DEPENDENCE

5.1 Introduction

Colloidal semiconductor quantum dots (QDs) have received much attention due to their potential applications in two-photon microscopy for bio-imaging, bio-labeling, and *etc*. [5.1, 5.2]. Compared with conventionally used organic dyes, colloidal QDs show many advantages such as greater photo-stability, brighter fluorescence, and less photo bleaching. In these applications, semiconductor QDs are normally required to be capped with a layer of organic ligand in order to be dissolved in water and smaller QDs are preferred for easy accessing to cells and increasing the labeling efficiency. The overall size of QDs can be smaller by reducing the layer thickness of the capping ligand as well as by carefully selecting the types of semiconductors.

Towards the above targets, CdTe QDs have been investigated extensively in a wide laser wavelength range from 750 nm to 1500 nm [5.1]. Frequency-degenerate two-photon absorption (TPA) of CdTe QDs has been measured and analyzed [5.4-5.7]. Padilha *et al.* have measured the TPA spectra of CdTe QDs doped in glass at two different sizes with diameters larger than 4 nm using the Z-scan technique [5.4, 5.5]. To interpret their TPA measurements, they have carried out TPA simulation based on a $k \cdot p$ model which includes the band mixing between the heavy hole and light hole. The simulation shows an

improvement in fitting the measured data as compared to the simple parabolic model [5.5]. However, discrepancies still exist between the theory prediction and the experiment, especially in the higher energy region [5.5]. Furthermore, QDs doped in glass are expected to be different from colloidal QDs due to different surrounding conditions. Pu *et al.* have studied colloidal CdTe QDs with six different sizes ranging from 4.4 to 5.4 nm in diameter. The TPA cross-sections have been found to be proportional to $R^{5.6}$, where R is the radius of QD [5.5, 5.6]. In their study, however, TPA has been examined at only one wavelength. Recently, He *et al.* have unambiguously measured the TPA spectra of colloidal CdTe QDs, but their average diameters are in the range from 6 to 8 nm with the size dependence remained unexamined [5.7]. Therefore, there is no systematic study on both size- and wavelength-dependent TPA in colloidal CdTe QDs with diameters less than 4 nm.

Here we report a systematical investigation into the TPA in aqueous solutions of glutathione-capped colloidal CdTe QDs with a core diameter equal to or less than 4 nm and a 0.5-nm-thick layer of capping ligand. This range of QD sizes implies that strong quantum confinement should play an important role since the sizes are much less than the Bohr radius (a_B = 7.5 nm). By the employment of femtosecond Z-scan technique at laser wavelengths ranging from 720 to 950 nm, the size-dependent TPA cross-sections are unambiguously measured. In order to gain a better understanding of the relationships between TPA and light wavelength as well as dot size for QDs in this strong confinement regime, the measurements are compared to theoretical modeling based on the eight-band, effective-mass model developed by Pidgeon and Brown [5.8, 5.9]. This model considers both the mixing between

the conduction and valence bands as well as the complex structure of the valence bands [5.8, 5.9].

5.2 Synthesis and characterization of CdTe quantum dots

The CdTe QDs studied here were prepared in accordance with a synthesis method reported elsewhere [5.3]. Briefly, it was based on the reaction of cadmium chloride with hydrogen telluride. With this synthesis method, glutathione (GSH) was utilized as capping ligand. The quantum yield of fluorescence could be as high as 45%, comparable to that of prevalent TOPO/TOP capping. However, the GSH capping agent made the QDs much smaller in the overall size, highly desirable in two-photon microscopic imaging. Three samples of different core sizes were synthesized; and their aqueous solutions in 1-mm-thick quartz cuvette were studied as described below. Table 1 summarizes the core diameter, bandgap energy, peak position of photoluminescence (PL), bandwidth of PL, volume fraction and QD density. Here, the bandgap energy, E_g, is taken as the lowest lying excitonic peak of QDs. The X-ray diffraction measurements confirmed that the QDs possess the zinc-blend, crystalline structure.

Table 5.1 Structural and optical parameters of CdTe QDs

	CdTe510	CdTe555	CdTe615
Radius, R (nm)	1.5±0.05	1.75±0.07	2.0±0.08
Band gap, E_g (eV)	2.53	2.31	2.10
PL peak position (nm)	510	555	615
$\Delta\lambda_{FWHM}$ (nm) of PL	36	45	50
Volume fraction (f_v)	0.66%	0.82%	2.47%
QD density, N (cm^{-3})	4.4×10^{17}	3.6×10^{17}	7.1×10^{17}

To determine both sizes and structures of the QDs investigated here, we carried out high-resolution transmission electron microscopic (HRTEM) studies. The core diameters of the three samples were found to be 3.0, 3.5, and 4.0 nm; denoted as CdTe 510, CdTe 555, and CdTe 615 , respectively, corresponding to their PL peak wavelengths. Fig. 5.1 (a) shows a HRTEM picture of sample CdTe 510. Clear lattice structures indicate that the QDs should be well crystallized. Size dispersions can be obtained from the HRTEM as shown in Fig. 5.1(b) for CdTe 510. Size dispersions of the three samples are determined to be ~7 %, which qualify them as nearly mono-dispersive. Fig. 5.2 shows both UV-VIS absorption and PL spectra of the three samples. The dependence of the emission wavelength on the dot radius is consistent with the published data [5.1]. Revealed from the UV absorption spectra, the band-gap energies of the three samples, or the lowest transitions $[1S_{3/2}(h)-1S_{1/2}(e)]$, are 2.53, 2.31, and 2.10 eV, respectively. Such a considerable variation in the band-gap energy with dot size suggests that strong size dependence should be expected for TPA. This strong dependence is attributed to the following two factors: namely (1) smaller electron effective mass for CdTe; and (2) significantly smaller QD radius than the Bohr radius (7.5 nm). As a result, the QDs investigated here are in the regime of very strong confinement.

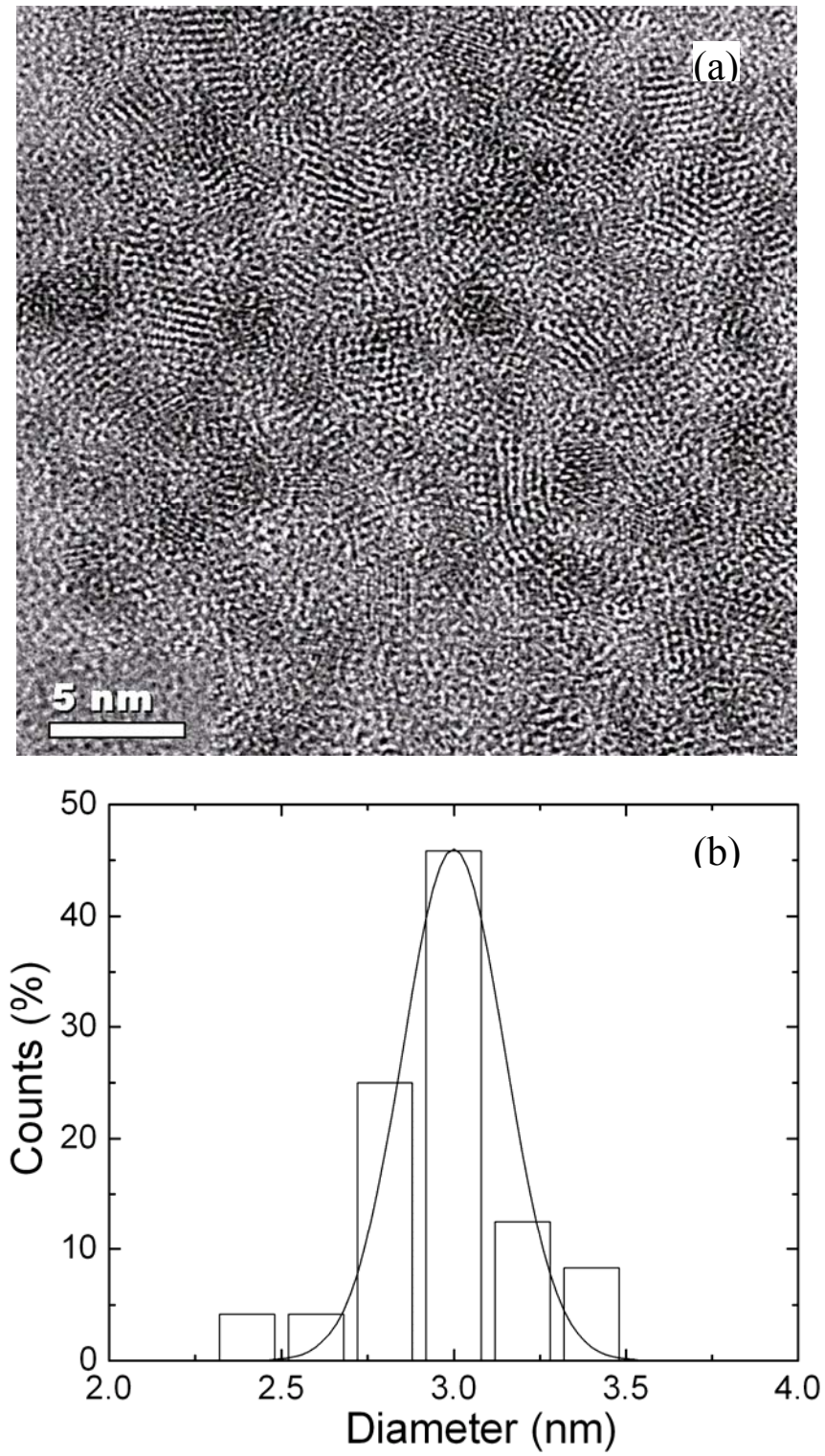

Fig. 5.1 (a) High-resolution transmission electron microscopic (HRTEM) photograph for the smallest size sample. (b) Size distribution for the smallest size sample obtained through the HRTEM.

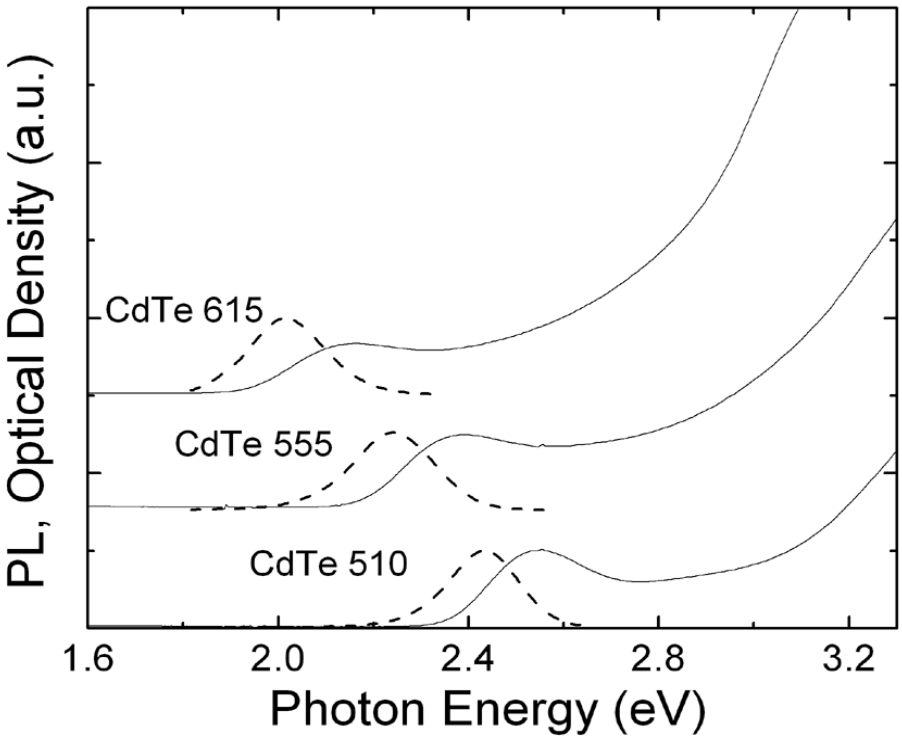

Fig. 5.2 Optical density (solid line) as well as photoluminescence (PL) (dashed line) of the three samples. The samples are denoted as CdTe 615, CdTe 555 and CdTe 510, respectively, corresponding to the PL peaks of the three samples.

5.3 Experimental study on the TPA in CdTe quantum dots

Open-aperture Z-scans were employed for the TPA measurements. The laser pulses were provided by a mode-locked Ti:Sapphire laser (Coherent, Chameleon) operated at 86-MHz repetition rate. The full width at half maximum (FWHM) of the laser pulses was from 98 to 150 fs, depending on the laser wavelength. The Z-scan setup was calibrated by using bulk CdS and CdTe polycrystals as standard samples. These calibrations showed that the measured TPA coefficients were in agreement with the theoretical values [5.10] within an experimental error of ~20%. The maximum laser intensity was limited to 25 $GWcm^{-2}$. Within this laser intensity range, the two-photon-excited electron-hole pairs per QD were estimated to be much less than the unity. As such, two-photo-excited carrier absorption should be insignificant [5.11]. This was further confirmed by the Z-scans carried out with several laser irradiances, from which the measured TPA coefficients were found to be independent of the laser irradiances. (Note that the laser irradiance was defined as the maximum on-axis laser irradiance within the sample. The loss in the laser irradiance due to the Fresnel reflection at the sample surface was taken into account). It should also be pointed out that the absorption spectra, PL spectra and Z-scans were conducted in a period of several weeks and no measurable difference was found, which provided the evidence that the samples were stable and suffered no laser-induced damage.) To assess the effects of high repetition rate on the TPA measurements, we also conducted open-aperture Z-scans with another Ti:Sapphire laser (Quantronix, Titan) at 780 nm operated at 1 KHz. The difference between the TPA measurements by the two different repetition rates was found to be less than 10%, indicating that

the effects induced by the high-repetition rate should be negligible. In addition, the capping agent (glutathione) in water was also Z-scanned under the same experiment, which confirmed that there was no significant nonlinear absorption from both glutathione and water.

Fig. 5.3 displays typical open-aperture Z-scans for sample CdTe 615. Following the standard analytical procedure [5.12], one can extract the TPA coefficient, β, from the best fit as shown by the solid lines Fig. 5.3. For two-photon microscopic applications, however, the TPA cross-section, σ_{TPA}, is more interested. It is obtained by $\sigma_{TPA} = \beta\hbar\omega/(\rho N)$, where N is the number density of QDs, ρ is the local field correction factor [5.13], and $\hbar\omega$ is the photon energy. The local field factor here is calculated to be 0.2. However, since the local field is reduced considerably in realistic situation [5.5], it is treated as unity in our calculation of σ_{TPA}. Fig. 5.4 shows that σ_{TPA} are measured to be on the orders of 10^3 *GM* (or $10^{-47} cm^4 s$) or higher. TPA in a piece of bulk polycrystal CdTe (10 x 10 x 0.5 mm in size, Semiconductor Wafer Inc.) was measured to be in the range between 20 and 25 cm/GW under the same experimental conditions, in agreement with the theoretical prediction in Ref. [5.10]. The σ_{TPA} values in the bulk CdTe are then calculated by $\sigma_{TPA} = \beta\hbar\omega / N_{CdTe}$ with N_{CdTe} being the CdTe molecular density. They are found to be in the order $\sim 10^{-49}\ cm^4 \cdot s \cdot photon^{-1}$ in the whole spectral range of interest. Thus, the σ_{TPA} values in QDs are at least two orders greater compared with bulk CdTe. Such an enhancement is similar to the findings for σ_{TPA} of CdS QDs that are two orders greater than its bulk counterpart [5.14].

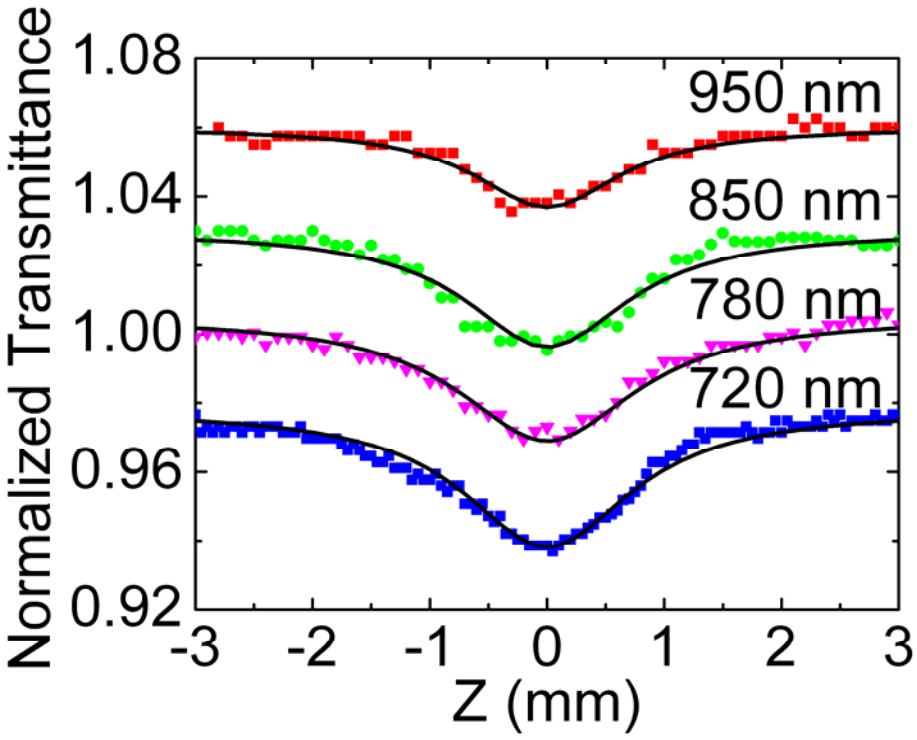

Fig. 5.3 Typical open-aperture Z-scans for CdTe 615. The solid curves are the fitting results. The laser intensities are 5.2 $GWcm^{-2}$, 4.8 $GWcm^{-2}$, 7.0 $GWcm^{-2}$ and 20 $GWcm^{-2}$ at 720 nm, 780 nm, 850 nm and 950 nm, respectively.

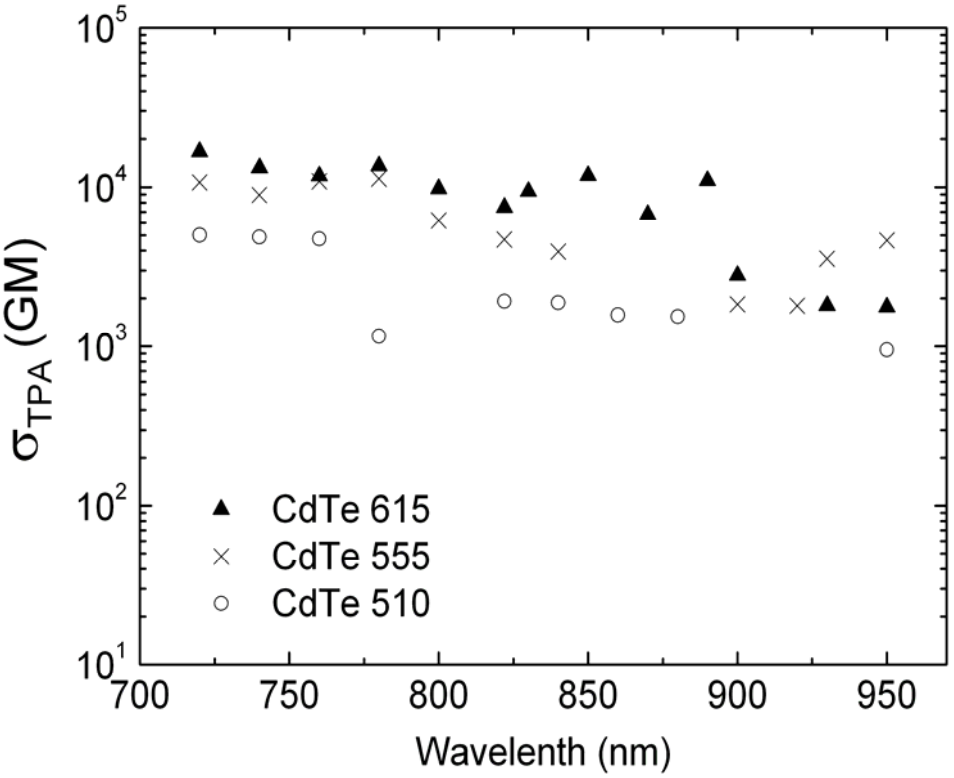

Fig. 5.4 Measured TPA cross-section spectra of the CdTe QDs. For all the sizes, the TPA cross-section is increased with the size of QD except for a few wavelengths.

It should be emphasized that the σ_{TPA} values reported here are determined unambiguously, without prior knowledge of the quantum efficiency of two-photon-excited PL. If the quantum efficiency of two-photon-excited PL is presumed to be between 20% and 45% [5.3], one may compute the action cross-section to be greater than 10^2 GM. Such magnitudes are comparable to CdSe QDs with similar sizes [5.2], at least one order greater than CdS QDs [5.14], and about two orders bigger than fluoresce in [5.2]. Furthermore, as shown in Fig. 5.4, the TPA cross-section is increased with the size of QDs except for a few wavelengths at which σ_{TPA} arises un-monotonously. Such a size dependence is in agreement with the previous reports for CdTe QDs [5.4-5.6] and CdSSe QDs [5.15, 5.16].

5.4 Theoretical study on the TPA in CdTe quantum dots

In order to gain deeper insight into the size-dependent TPA spectra of QDs in the very strong confinement, we have carried out theoretical studies. Several theoretical models have been employed to predict the frequency-degenerate TPA of QDs [5.4, 5.5, 5.17, 5.18]. Fedorov *et al.* have derived analytical expressions for TPA in QDs under the parabolic band approximation in which one conduction band and three valence bands are simply considered as parabolic and all couplings are ignored [5.17]. Their results are in agreement with the experiments for QD sizes close to or larger than the Bohr radius [5.4, 5.5]. However, for QDs in the strong confinement regime where the radius is much smaller than the Bohr radius, the discrepancy can be found [5.5, 5.18, 5.19]. Padilha *et al.* have modeled the TPA of CdTe QDs based on a so-called $k \cdot p$ theory which includes the mixing among the

heavy-hole band and light-hole band, while the mixing between the conduction and valence bands is ignored [5.5]. Their simulation fitted the experiments better than the parabolic approximation model. However, in the higher-energy region, discrepancies still exist [5.5]. The band mixing between the conduction and valence bands is important when the confinement energy is comparable or greater than the bulk band-gap energy. This mixing has to be considered in order to get the quantitative description of the energy levels in narrow band-gap semiconductors as well as in moderate-gap semiconductors such as CdTe. Efros *et al.* [5.9] have published an analytical theory of energy levels with a reformulation $k \cdot p$ theory based on a spherical eight-band Pidgeon and Brown (PB) model where the mixing between the conduction and valence bands as well as the complex structure of the valence bands were taken into account. The size dependence of the electronic spectra of InAs and InP nanocrystals gives more explicit evidence of the importance of using this so-called PB model in calculation of energy levels [5.20, 5.21].

5.4.1 Wave functions and energy levels in CdTe quantum dots

As mentioned in Chapter II, to calculate the two-photon absorption (TPA) in materials due to the electronic transitions, we have to know the electronic structures including the band energy and the corresponding wave functions. The TPA absorption then can be calculated by applying the Fermi's golden rule, with known initial, intermediate, final states and the corresponding wave functions of these states.

The wave functions of electron and hole in PB model are represented by:

$$\psi^{\pm}(r) = \sum_{i=1}^{4} C^{\pm}(k_i) j_l(k_i r) \sum_{\mu=-a}^{a} \Omega_{\mu}^{\pm} u_{a,\mu}^{c,v}$$

(5.1)

where $a = 1/2$ for the electron and spin split-off hole bands; and $a = 3/2$ for the heavy- and light-hole bands. the + and – signs represent even states and odd states, respectively, $\Omega_{\mu}^{\pm}$ is the angular function, and $u_{a,\mu}^{c,v}$ is the Bloch function [5.9]. Here, the barrier around each QD is assumed to be infinite, *that is*, the wave functions should vanish outside the QD. The wave functions and the energy levels are calculated by applying the analytical expressions based on the eight-band effective-mass PB model [5.9]. Fig. 5.5 shows the energy levels of electron (Fig. 5.5 (a)) and holes (Fig. 5.5 (b)). From Fig. 5.5 we can see that the energy levels are much complex than in the parabolic model. Fig. 5.6 to Fig. 5.8 shows the examples of band structures of electron and heavy hole states.

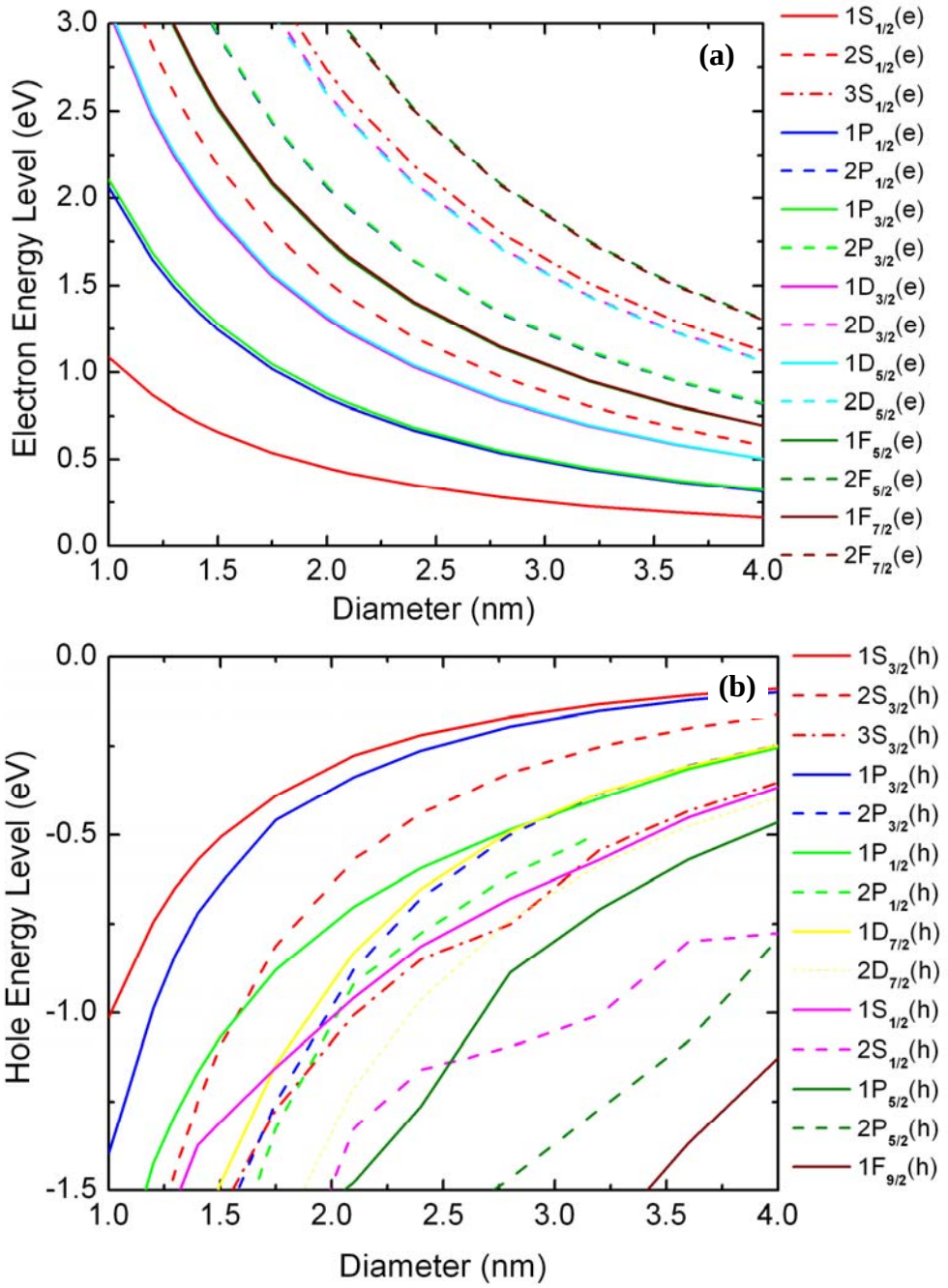

Fig. 5.5 Size dependent lowest energy levels of (a) electron and (b) hole in CdTe nanocrystals.

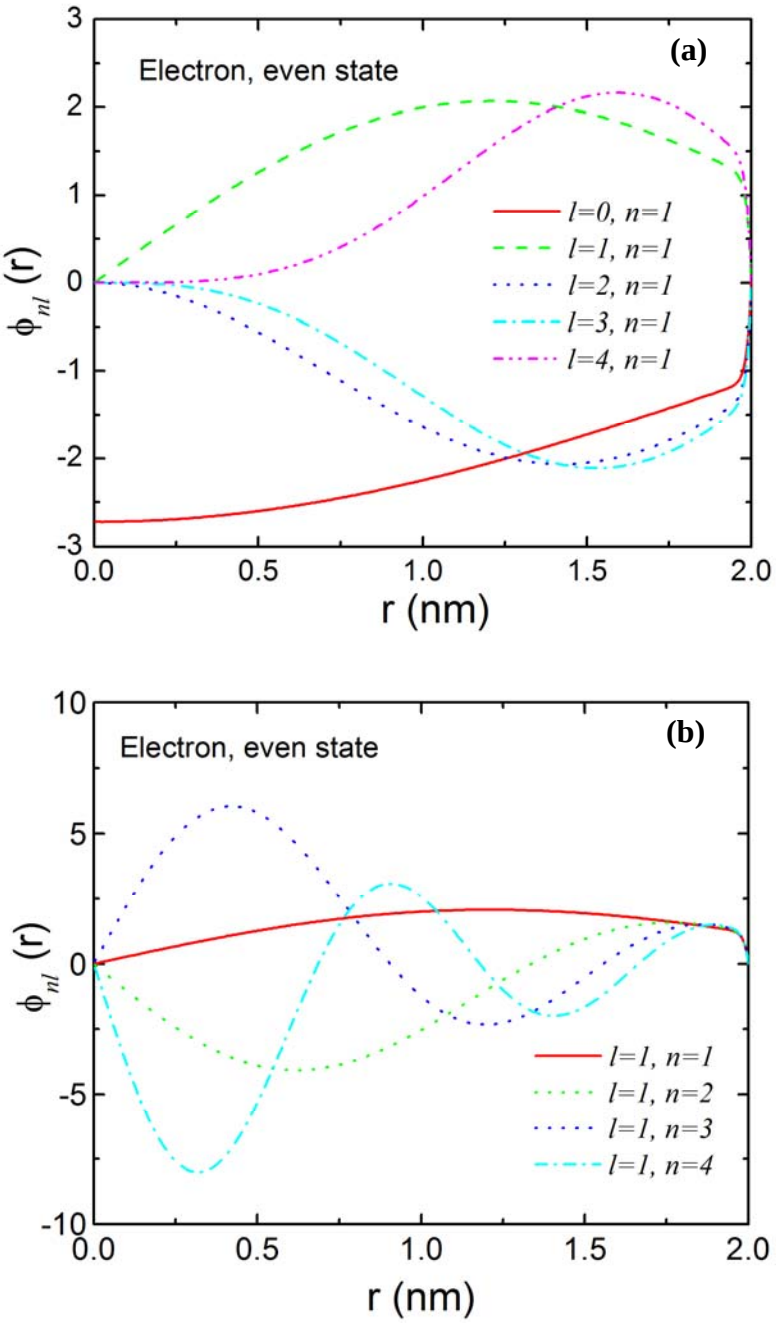

Fig. 5.6 Wave functions of even state electron with (a) *n=1,l=1* to *6*; (b) *l=1, n=1* to 4.

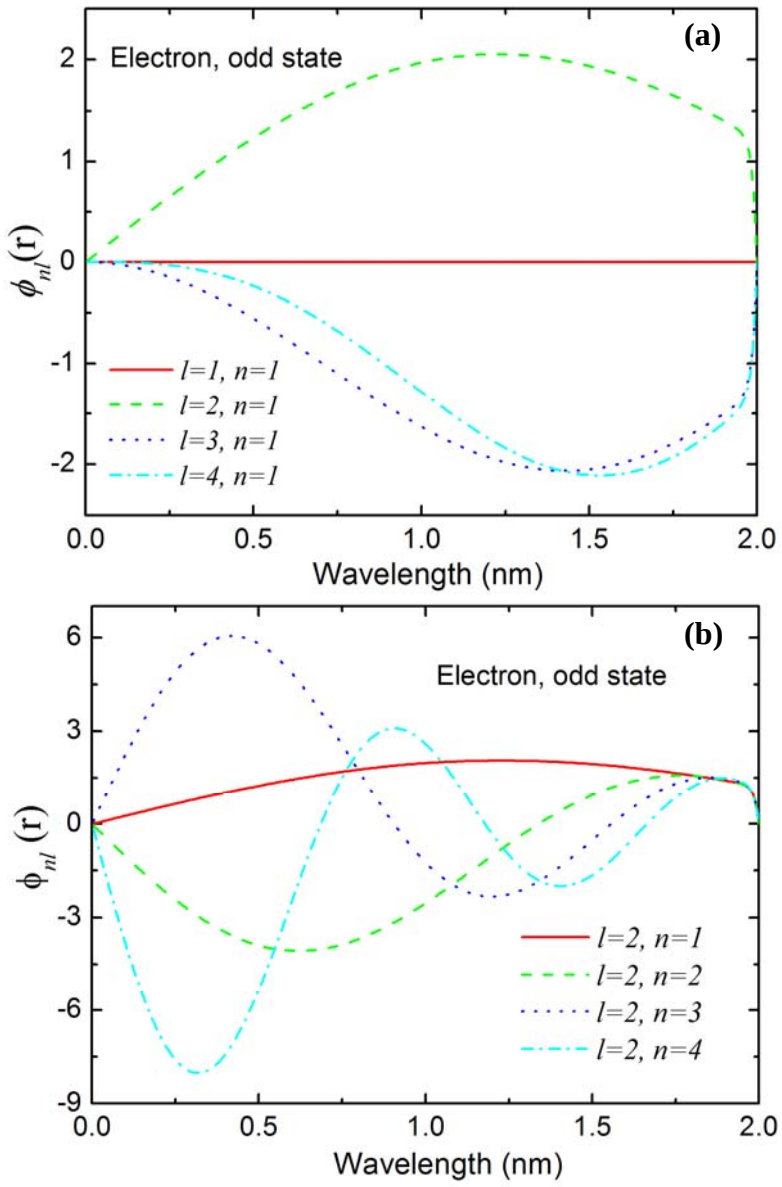

Fig. 5.7 Wave functions of odd state electron with (a) *n=1,,l=1* to *4*; (b) *n=1* to 4, *l=2*.

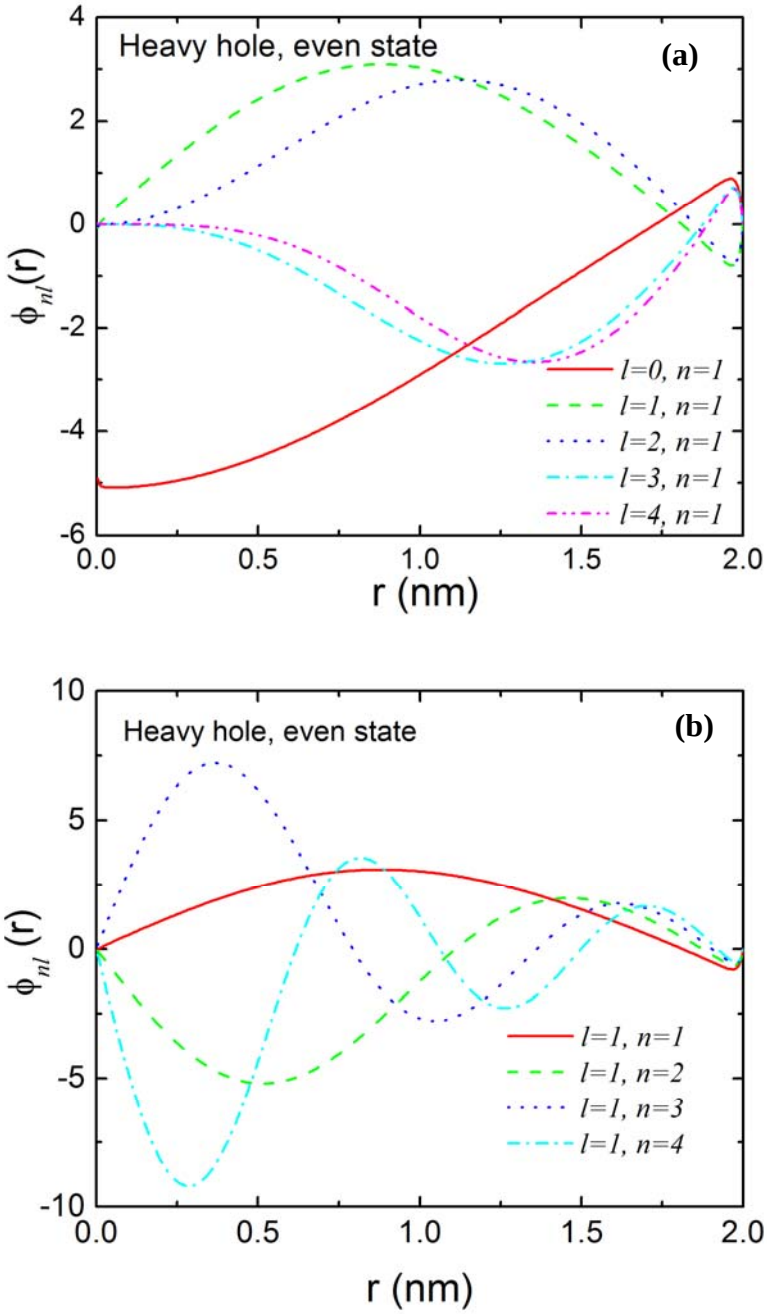

Fig. 5.8 Wave functions of even state heavy hole with (a) n=1; l=0 to 4; (b) l=1, n=1 to 4.

To ascertain the necessity of including the conduction-valence band coupling in the calculation of TPA for CdTe QDs in the strong confinement regime, we first calculate the band-gap energy of CdTe QDs based on the two models: namely (1) the parabolic model and (2) the eight-band effective-mass PB model. Here, we define the band-gap energy as the energy difference between the states of $1S_{1/2}(e)$ and $1S_{3/2}(h)$ adding the coulomb correction in the first-order perturbation. Fig. 5.9 shows the two curves for the size dependence of the band-gap energy, which are compared to the measurements obtained from the UV-visible absorption spectra. It demonstrates that the band-gap energy calculated by the eight-band effective-mass PB model predicts lower value under stronger confinement, whereas the two models produce similar results for dot radii larger than 4 nm. Furthermore, we find that the band-gap energy calculated by the eight-band effective-mass PB model fits perfectly to our experimental data and the data reported in Ref. [5.6, 5.22], as shown in Fig. 5.9.

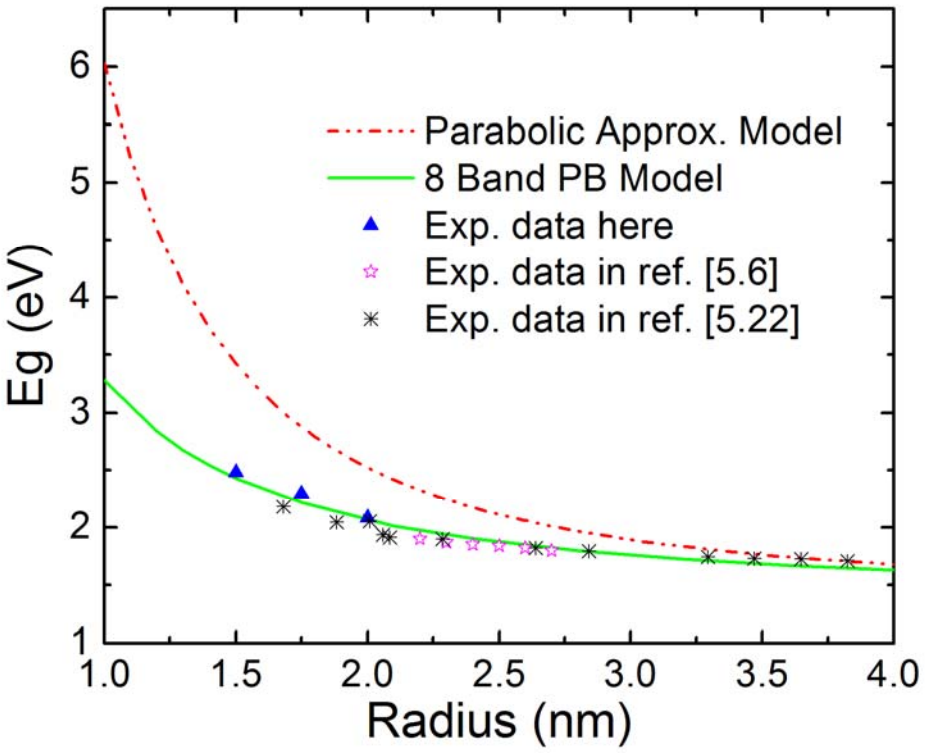

Fig. 5.9 Band gap energy of CdTe QDs calculated by the parabolic model (red doted) and the eight-band effective-mass PB model (blue solid). The solid triangles are the data from the UV-visible absorption spectra (see Fig.5.1).

5.4.2 Theoretical calculation of TPA in CdTe quantum dots

In this section, we model the TPA spectra of CdTe QDs in the very strong confinement regime, *ie*, the dot radii are in the range from 1.0 to 2.0 nm. The wave-functions as well as the energy levels are calculated based on the PB model. Our calculation are conducted with the bulk parameters of CdTe taken from [5.9] except that the bulk band-gap energy used here is 1.47 eV at room temperature [5.23] rather than 1.61 eV at 0 K.

By the Fermi's golden rule, the two-photon generation rate can be expressed as [5.24]:

$$W^{(2)} = \frac{2\pi}{\hbar}\sum_{j=1}^{3}\sum_{v1,v0}\left|\sum_{v2}\frac{\left\langle \psi_{v1}^{c}\left|\frac{A}{mc}\vec{e}\cdot\vec{P}\right|\psi_{v2}^{c\ or\ hj}\right\rangle\left\langle \psi_{v2}^{c\ or\ hj}\left|\frac{A}{mc}\vec{e}\cdot\vec{P}\right|\psi_{v0}^{hj}\right\rangle}{E_{v2}-E_{v0}-\hbar\omega-i\hbar\gamma_{i}}\right|^{2}\delta(E_{v1}-E_{v0}-2\hbar\omega) \tag{5.2}$$

where, ψ is the wave function; c represents the conduction band; h_1, h_2 and h_3 refer to the light-hole, heavy-hole and spin split-off hole bands, respectively; $\frac{A}{mc}\vec{e}\cdot\vec{P}$ is the optical interaction Hamiltonian with $A\vec{e}$ being the vector potential of light with the amplitude A and the polarization of $\vec{e}$; $\vec{P} = -i\hbar\nabla$ is the electron momentum operator; $v0$, $v1$, and $v2$ represent the initial, final, and intermediate states of electron subsystems, respectively; and γ_{v2} is the inverse life time of state $v2$. Each TPA transition here is also involved one interband and one intraband transition as discussed in [5.4, 5.5, 5.17].

Considering that there is size dispersion, $f(R)$, for a given QD system, the TPA coefficient, β, can be calculated by:

$$\beta = 4\hbar\omega\frac{N}{I^{2}}\int dRf(R)W^{(2)} \tag{5.3}$$

where, $f(R)$ is taken as a Gaussian function here, I is the light intensity. Considering the light intensity: $I = \varepsilon_{\omega}^{1/2}\omega^2 A^2 (2\pi c)^{-1}$, the TPA coefficient can be further written as:

$$\beta = \frac{4N(2\pi)^3 c^2}{\varepsilon_{\omega} \cdot \omega^3} \sum_{j=1}^{3} < F_{c,hj} > \tag{5.4}$$

where

$$< F_{c,hj} >= \int dR f(R) \sum_{v1,v0} \left| \sum_{v2} \frac{\left\langle \psi_{v1}^{c} \left| \frac{1}{mc} \vec{e} \cdot \vec{P} \right| \psi_{v2}^{c \text{ or } hj} \right\rangle \left\langle \psi_{v2}^{c \text{ or } hj} \left| \frac{1}{mc} \vec{e} \cdot \vec{P} \right| \psi_{v0}^{hj} \right\rangle}{E_{v2} - E_{v0} - \hbar\omega - i\hbar\gamma_i} \right|^2 \delta(E_{v1} - E_{v0} - 2\hbar\omega) \tag{5.5}$$

From Eqn. (5.4) and $\sigma_{TPA} = \beta\hbar\omega / N$, the TPA cross-section can be given by:

$$\sigma_{TPA} = \frac{4(2\pi)^3 c^2 \hbar}{\varepsilon_{\omega} \cdot \omega^2} \sum_{j=1}^{3} < F_{c,hj} > \tag{5.6}$$

Then, the integral in Eqn. (5.6) is carried out in a numerical way. For a given average size and size dispersion, it should be pointed out that no free parameter is involved in the numerical calculation. The numerical solutions for the TPA coefficient are shown in Fig. 5.10, whereby good agreement is reached between the modeling and the experiment with a few exceptions, which may be largely due to the experimental errors. In Fig. 5.10, the TPA spectra have also been calculated by the parabolic model with the same material parameters. As shown by the dashed line in Fig. 5.10, the TPA spectra calculated with the parabolic model have very big discrepancy with the experimental results, especially for CdTe 510 and CdTe 555. In Fig. 5.10, the first three maximum values for each calculated spectrum of TPA are marked with 1st Max., 2nd Max., and 3rd Max., respectively, starting from the lower

energy end.

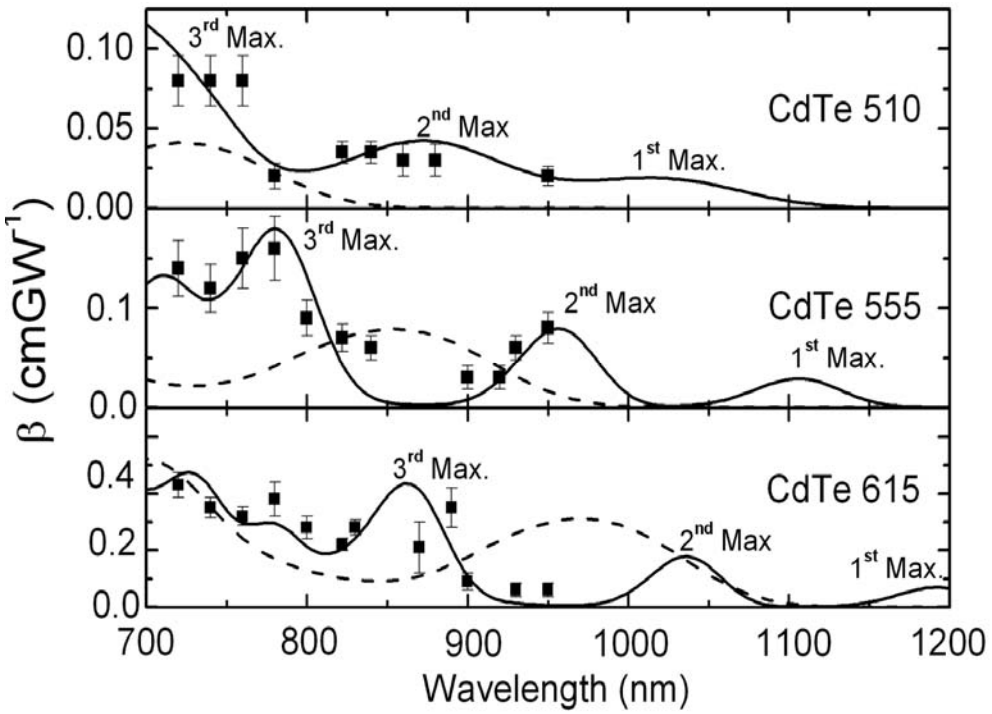

Fig. 5.10 TPA coefficients from the Z-scans (solid squares) compared with the calculated curves by the eight-band PB model (solid curves) and the parabolic model (dashed curves). The size dispersions are taken as 7% for all the calculations.

As mentioned above, the difference between our calculation and theoretical modeling reported in [5.5] is that the mixing between the conduction band and valence bands has been considered in our calculation whereas in [5.5] only the mixing between the heavy- and light-hole bands has been considered. To illustrate the importance of mixing between the conduction band and valence bands in the TPA calculation for smaller QDs, our calculation is also extended to CdTe QDs with a band-gap energy located at 600 nm, as compared to CdTe 600 reported in [5.5]. As shown in Fig. 5.11, compared with the calculation based on the parabolic model which excludes the band mixing, the theoretical calculation in [5.5] predicts larger values which are closer to the experimental measurements in higher energy spectral region. However, there are still many discrepancies. Our calculation, as shown in Fig. 5.11 with the solid curve, predicts higher values in this higher-energy spectral region than those in [5.5] and fits the experimental data better. This improvement in theory implies that the mixing between the conduction and valence bands and the complex structures of the valence bands should play an important role in the strong confinement regime.

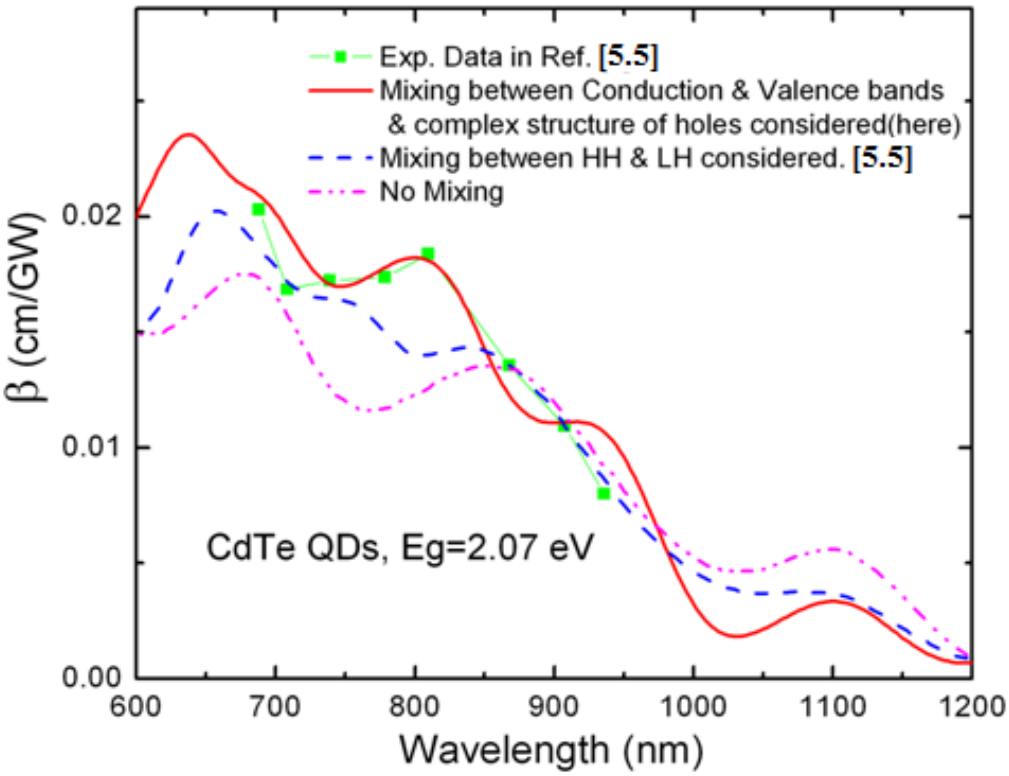

Fig. 5.11 Comparison of the calculated TPA spectra based on eight-band PB modeling (red solid curve), the modeling reported in Ref. 5.5 (blue dashed curve) and the parabolic approximation modeling (magenta dash doted curve), for CdTe QDs with band-gap energy at 600 nm (2.07 eV). The green solid squares are the experimental data reported in Ref. 5.5. The HH and LH stand for heavy hole, and light hole, respectively.

Fig. 5.12 displays the calculated TPA cross-section as a function of both light wavelength and dot diameter, with the size dispersion taken as 7% for all the QD systems. From this figure, two findings can be established, namely, (1) at a given wavelength, the TPA cross-section has an increasing trend with dot size; and (2), this increasing trend is un-monotonous, and is composed of several 'peaks' and 'valleys' for some sizes. In order to illustrate the first point further, the TPA cross-sections at 700 nm, 780 nm and 860 nm are plotted as a function of the dot diameter, as shown in Fig. 5.13. The data can be fitted with $\sigma_{TPA} = A \cdot (2R)^B$, where A = 38, 10 and 0.21, B = 4.7, 5.28 and 7.7 for 700 nm, 780 nm and 860 nm, respectively. Fittings at some other wavelengths show that the B values in the whole spectral range of interest are larger than 3. Since the QD volume is proportional to the cubic of radius, the σ_{TPA} normalized by the volume of QD still increases with QD size for a given wavelength. This is consistent with the conclusion by Ref. [5.5, 5.6].

Fig. 5.14 shows the three maxima in the lower-end spectrum of TPA cross-section as a function of the QD size. As be demonstrated clearly, these cross-sections can not be fit with the empirical expression: $\sigma_{TPA} = A \cdot (2R)^B$. This can be attributed to the complication induced by the fact that the band-gap energy or the maximum in the TPA spectra is a nonlinear function of the dot size. From Fig. 5.14, one can conclude that in the strong confinement regime, most of the maximum values fall into the area which can be outlined by the two curves with B values equal to 3 and 2, respectively. Thus the volume-normalized maximum values are less sensitive to the dot size.

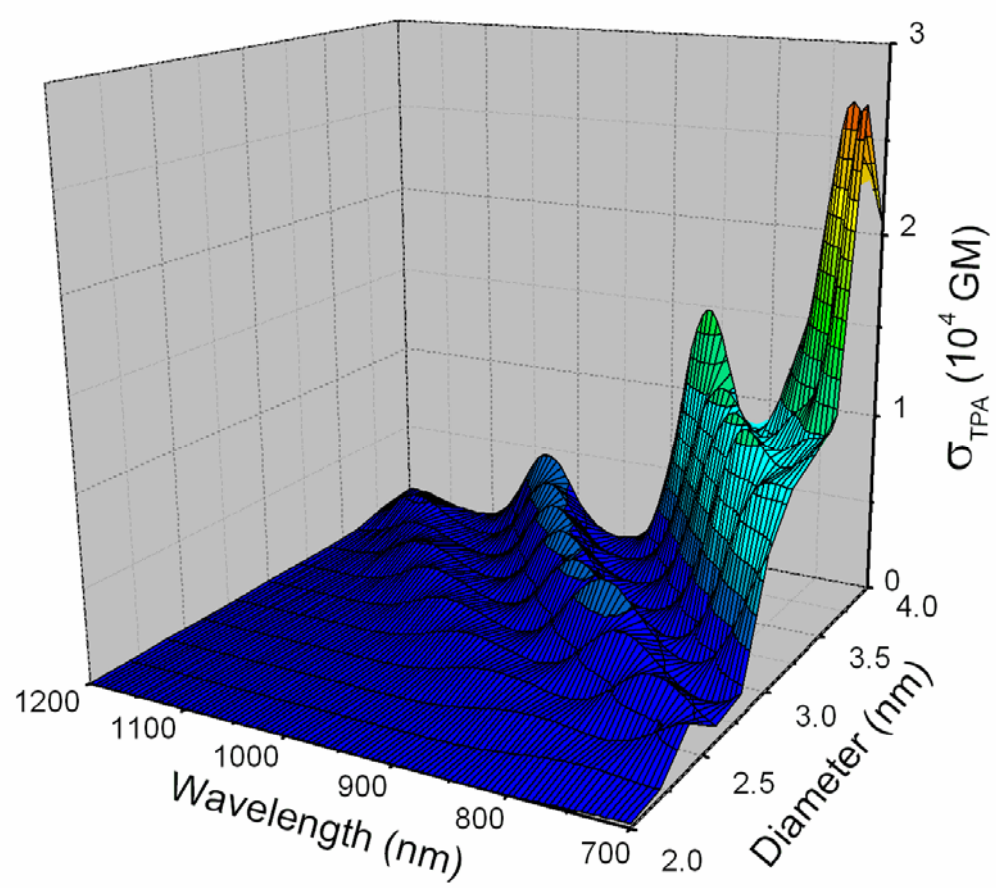

5.12 Calculated TPA cross-section of CdTe QDs by the eight-band PB model as a function of both size and wavelength.

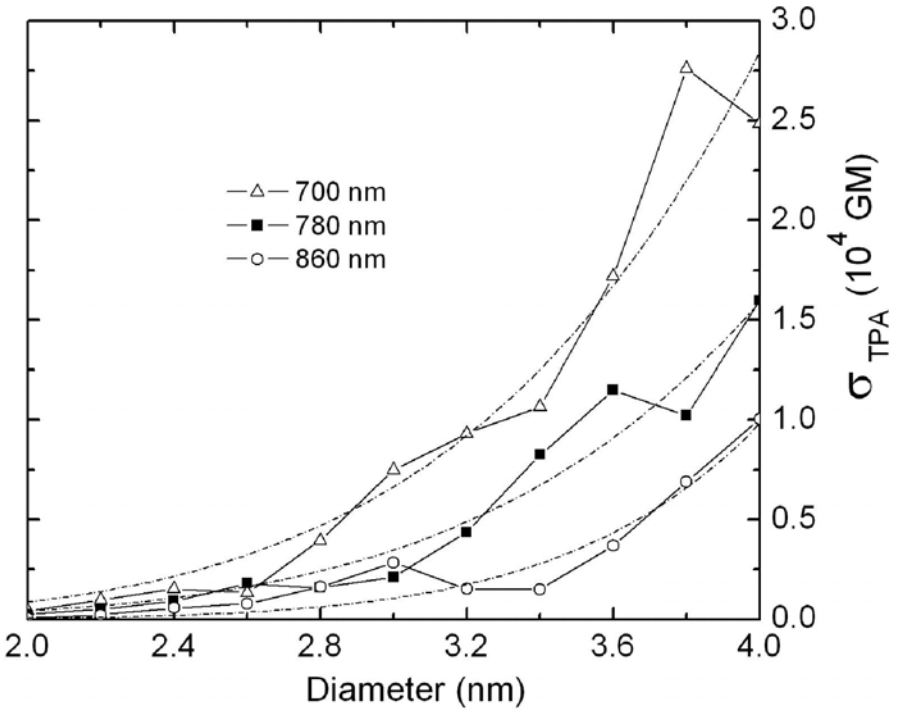

5.13 Calculated TPA cross-section of CdTe QDs by the eight-band PB model as a function of the dot diameter (solid circles) at 700 nm (-Δ-), 780 nm (-■-) and 860 nm (-○-). The dashed curves are fitting curves with equation: $\sigma_{TPA} = A \cdot (2R)^B$, where A is 38, 10 and 0.21 and B is 4.7, 5.28 and 7.7, for 700 nm, 780 nm and 860 nm, respectively.

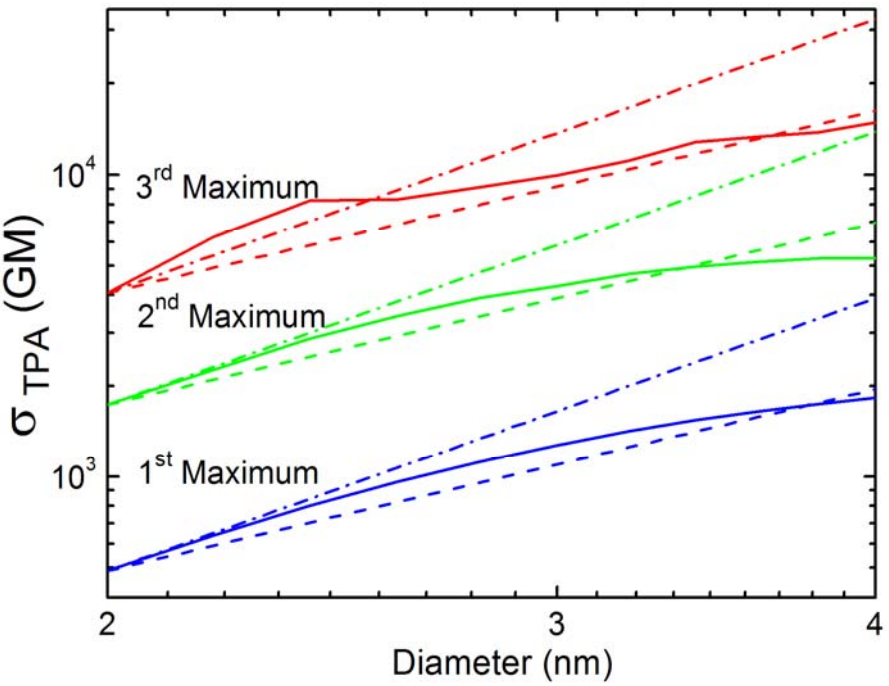

5.14 Calculated TPA cross-sections of CdTe QDs at three maxima in the TPA spectra as a function of the dot size. The solid curves represent the calculated TPA cross-sections, whereas the dashed and dashed-dot lines are the curves proportional to $(2R)^2$, $(2R)^3$, respectively.

As mentioned above, both experimental and theoretical studies show a general increasing trend in the TPA with dot size. It is interesting to find out the factors that contribute to this trend. Since the TPA spectra are composed of many transitions, we may examine the number of transitions as well as the amplitude of each transition as functions of the dot size. In Fig. 5.15, the transitions are drawn within the transition energy range from 700 nm to 1200 nm. From Fig. 5.15 we can see that the number of transitions in this range increase with dot size as mentioned by previous works [5.5, 5.20]. The first ten transitions involved are as follows: 1) $1P_{3/2}(h) \to 1S_{1/2}(e)$; 2) $1P_{1/2}(h) \to 1S_{1/2}(e)$; 3) $1S_{3/2}(h) \to 1P_{1/2}(e)$; 4) $1S_{3/2}(h) \to 1P_{3/2}(e)$; 5) $2P_{3/2}(h) \to 1S_{1/2}(e)$; 6) $2S_{3/2}(h) \to 1P_{3/2}(e)$; 7) $1P^{s}_{3/2}(h) \to 1S_{1/2}(e)$; 8) $1P_{3/2}(h) \to 1D_{5/2}(e)$; 9) $1D_{7/2}(h) \to 1P_{3/2}(e)$; and 10) $1S_{1/2}(h) \to 1P_{1/2}(e)$. Here, the notations for electron and hole levels use standard atomic notations of nQ_J with J the total angular momentum, $Q = S, P, D, \ldots$ is the lowest value of the angular momentum of wave functions, and n is the ordinal number of the level with a given symmetry [5.9].

In order to investigate the change in the amplitude of TPA transition with dot size, the first ten transitions are plotted in Fig. 5.16. As can be seen from Eqns. (5.4) and (5.6), for a given transition, the TPA cross-section σ_{TPA} is composed of a factor of $C = 4(2\pi)^3 c^2 \hbar / (\varepsilon_\omega \cdot \omega^2)$ and $< F_{c,hj} >$. The former is related to the photon frequency; and the latter is dominated by the interband and intraband transition matrix elements. As shown in Fig. 5.16 (a), the $< F_{c,hj} >$ values are flat in the spectral range except for transitions 3 and 8. The changes in the peaks of transitions 3 and 8 may be due to the coherent

intermediate transition involved. The $< F_{c,hj} >$ value thus makes no significant contributions to the increase of TPA with size. However, from Fig. 5.16 (b), except transition 3, σ_{TPA} values are monotonously increased with dot size. Therefore, the main contributor to the increase in the TPA with dot size is the factor of C which is inversely proportional to the square of the photon frequency. As the dot size becomes bigger, the same transition becomes red shifted and hence, has smaller transition frequency. As such, the C value becomes bigger for larger QDs. From the above discussion, we can see that there are two factors which contribute to the TPA increase with dot size: one is the more number of transitions involved for bigger QDs in a certain energy range; and the other is the red shift of the transitions for larger QDs.

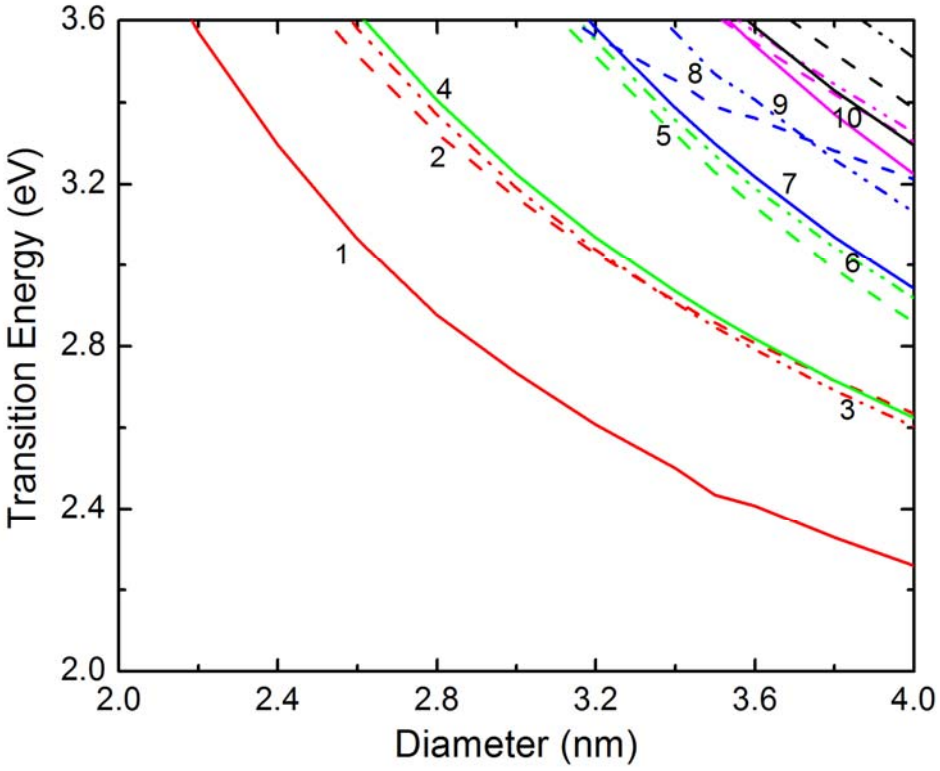

Fig. 5.15 Transition energies vs dot diameter in the transition energy range of 2.0 eV to 3.6 eV (corresponds to a wavelength range from 700 nm to 1200 nm). The first ten transitions are as follows: 1) $1P_{3/2}(h) \rightarrow 1S_{1/2}(e)$; 2) $1P_{1/2}(h) \rightarrow 1S_{1/2}(e)$; 3) $1S_{3/2}(h) \rightarrow 1P_{1/2}(e)$; 4) $1S_{3/2}(h) \rightarrow 1P_{3/2}(e)$; 5) $2P_{3/2}(h) \rightarrow 1S_{1/2}(e)$; 6) $2S_{3/2}(h) \rightarrow 1P_{1/2}(e)$; 7) $2S_{3/2}(h) \rightarrow 1P_{3/2}(e)$; 8) $1P^{s}_{3/2}(h) \rightarrow 1S_{1/2}(e)$; 9) $1P_{3/2}(h) \rightarrow 1D_{5/2}(e)$; and 10) $1D_{3/2}(h) \rightarrow 1P_{1/2}(e)$.

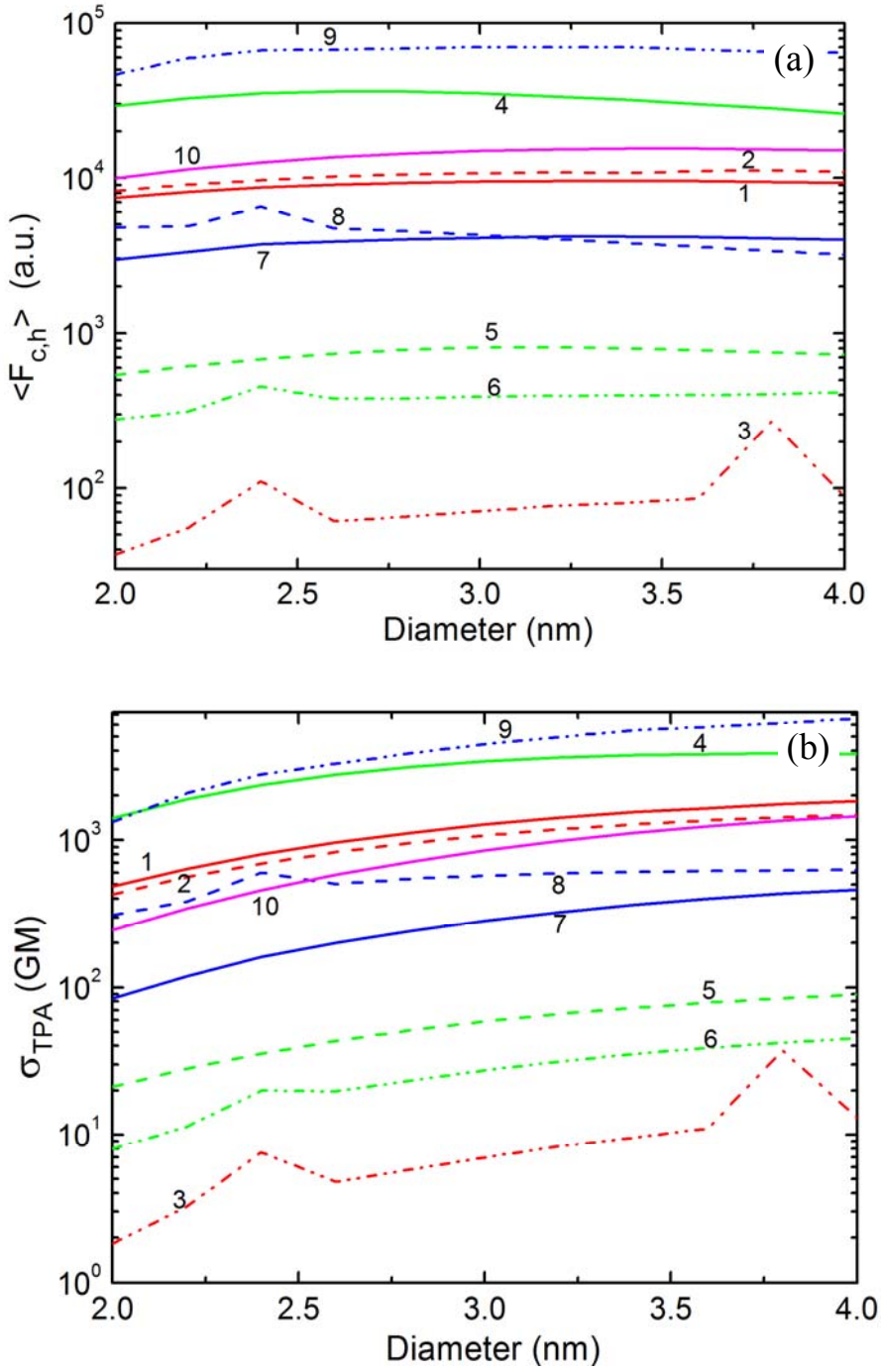

Fig. 5.16 (a) $< F_{c,hj} >$ and (b) σ_{TPA} contributed from the first ten transitions as a function of the dot diameter.

The above calculations have been done with the fixed size dispersion of 7%. To investigate the size dispersion effects, the TPA spectra with different size dispersion have been calculated with our model for an average radius of 2 nm, as shown in Fig. 5.17. From Fig. 5.17 we can see that the TPA coefficient spectra changes in two manners as the size dispersion gets broadening. Firstly, the transition peaks in the TPA spectrum gets less sensitive to the wavelength. This is obvious since each transition has a certain transition energy for one size; while, for many sizes, their transition energies form a broad band. The larger the dispersion is, the broader the band is. In some applications, this less dependence on laser wavelengths is desirable. Secondly, the transition peaks shift to the red side as the size dispersion becomes widening. This is due to the fact, as revealed previously, the larger the size, the greater the TPA. As the size dispersion becomes broader, more QDs of bigger sizes involve and make the spectrum shift to the red side.

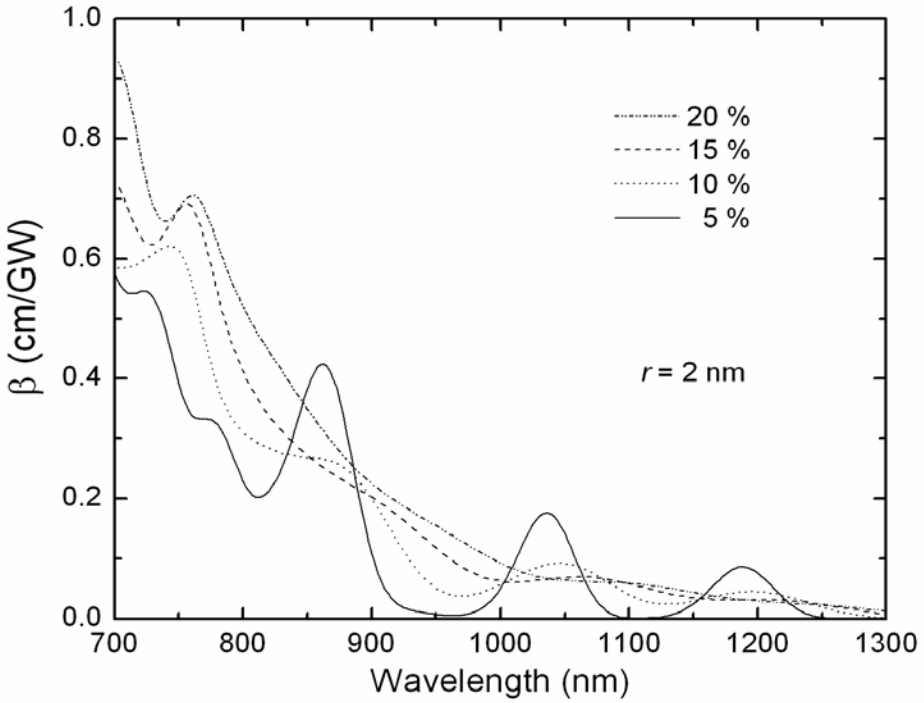

Fig. 5.17 Calculated TPA spectra by the PB model with different size dispersions for an average radius of 2 nm.

5.5 Conclusions

In conclusion, the size dependence of TPA spectra in the strongly confined colloidal CdTe QDs has been unambiguously determined with femtosecond Z-scans. The TPA cross-sections are measured to be increased with dot size and are on the order from 10^{-47} to 10^{-46} $cm^4 \cdot s \cdot photon^{-1}$. The measured TPA cross-sections are compared to the theoretical modeling under an eight-band Pidgeon and Brown effective mass approximation. By taking into account of the conduction-valence band mixing and the complex structures of the valence bands, the theory can give more accurate prediction for TPA of CdTe QDs in the strong confinement regime. The factors that contribute to the increase in the TPA with dot size and the effects of size dispersion on the TPA are discussed.

REFERENCES

[5.1] X. Michalet, F. F. Pinaud, L. A. Bentolila, J. M. Tsay, S. Doose, J. J. Li, G. Sundaresan, A. M. Wu, S. S. Gambhir, and S. Weiss, Science **307**, 538 (2005) and references therein.

[5.2] D. R. Larson, W. R. Zipfel, R. M. Williams, S. W. Clark, M. P. Bruchez, F. W. Wise, and W. W. Webb, Science **300**, 1434 (2003) and references therein.

[5.3] Y. G. Zheng, S. G. Gao, and J. Y. Ying, Adv. Mater. **19**, 376 (2007).

[5.4] L. A. Padilha, J. Fu, D. J. Hagan, and E. W. V. Stryland, Optics express 13, 6460 (2005).

[5.5] L. A. Padilha, J. Fu, D. J. Hagan, E. W. Van Stryland, C. L. Cesar, L. C. Barbosa, C. H. B. Cruz, D. Buso, and A. Martucci, Phys. Rev. B **75**, 075325 (2007).

[5.6] S. C. Pu, M. J. Yang, C. C. Hsu, C. W. Lai, C. C. Hsieh, S. H. Lin, Y. M. Cheng, and P. T. Chou, "The Empirical Correlation Between Size and Two-Photon Absorption Cross Section of CdSe and CdTe Quantum Dots," Small **2**, 1308 (2006).

[5.7] G. H. He, Q. D. Zheng, K. T. Yong, and A. Urbus, Appl. Phys. Lett. **90**, 181108 (2007).

[5.8] C. R. Pidgeon and R. N. Brown, Physical Review **146**, 575 (1966).

[5.9] Al. L. Efros and M. Rosen, Phys. Rev. B **58**, 7120 (1998).

[5.10] E. W. V. Styland, M. A. Woodall, H. Vanherzeele, and M. J. Soileau, Opt. Lett. **10**, 490 (1985).

[5.11] Y. L. Qu, W. Ji, Y. G. Zheng, and J. Y. Ying, Appl. Phys. Lett. **90**, 133112 (2007).

[5.12] M. Sheik-Bahae, A. A. Said, T. H. Wei, D. J. Hagan, and E. W. V. Styland, IEEE, J. Quantum Electronics **26**, 760 (1990).

[5.13] D. Ricard, Ph. Roussignol, and Chr. Flytzanis, Opt. Lett. **10**, 511 (1985).

[5.14] J. W. M. Chon, M. Gu, C. Bullen, and P. Mulvaney, Appl. Phys. Lett. **84**, 4472 (2004).

[5.15] Yu. V. Vandyshev, V. S. DneprovskiĬ, and V. I. Klimov, Sov. Phys. JETP **74**, 144 (1992).

[5.16] H. Shinojima, J. Yumoto, and N. Uesugi, Appl. Phys. Lett. **60**, 298 (1992).

[5.17] A. V. Fedorov, A. V. Baranov, and K. Inoue, Phys. Rev. B **54**, 8627 (1996).

[5.18] K. I. Kang, B. P. McGinnis, Sandalphon, Y. Z. Hu, S. W. Koch, N. Peyghambarian, A. Mysyrowicz, L. C. Liu, and S. H. Risbud, Phys. Rev. B **45**, 3465 (1992).

[5.19] P. C. Sercel and K. J. Vahala, Phys. Rev. B **42**, 3690 (1990).

[5.20] U. Banin, C. J. Lee, A. A. Guzelian, A. V. Kadavanich, and A. P. Alivisatos, W. Jaskolski and G. W. Bryant, Al. L. Efros and M. Rosen, J. Chem. Phys. **109**, 2306 (1998).

[5.21] P. C. Sercel, Al. L. Efros, and M. Rose, Phys. Rev. Lett. **83**, 2394 (1999).

[5.22] W. William Yu, Lianhua Qu, Wenzhuo Guo, and Xiaogang Peng, Chem. Mater. **15**, 2854 (2003).

[5.23] J. Singh, *Physics of Semiconductors and Their Heterostructures*, (McGraw Hill, New York,1993).

[5.24] D. C. Hutchings and E. W. Van Stryland, J. Opt. Soc. Am. B **9**, 2065 (1992).

Chapter VI

CONCLUSIONS AND OUTLOOK

The objectives of the studies presented in this thesis were the investigation of TPA and relaxation in colloidal CdSe and CdTe QDs, with femtosecond Z-scan and pump probe techniques。

The TPA cross-sections for CdSe QDs with 2 nm in diameter are revealed to be around 10^{-47} to 10^{-46} $cm^4 \cdot s \cdot photon^{-1}$, depending on the excitation wavelength in the range from 950 nm to 750 nm. These values are similar to the published computation result based on a simple four-band parabolic model. The Auger constant is revealed to be on the order of $\sim 10^{-30} cm^6 s^{-1}$. Intraband absorption cross-sections are found to be in the range from 10^{-18} to $10^{-17} cm^2$ from 680 to 780 nm. Experimental evidence demonstrates that the Auger recombination or the intraband absorption takes place under the condition that the average electron-hole pair per quantum dot is larger than unity.

The size-dependent TPA cross-sections of colloidal CdTe QDs are measured to range from 10^{-47} to 10^{-46} $cm^4 \cdot s \cdot photon^{-1}$, depending on the wavelength of excitation and the size of CdTe QDs. The TPA measurements are in agreement with theoretical modeling based on a spherical eight-band Pidgen and Brown model. The quantitative modeling reveals clearly that there are two main contributors to the size effect on TPA: one is the increasing density of transitions for increasing size and the other is the red-shift of each

transition for larger size.

The studies presented in this thesis provide useful information for many applications based on two-photon absorption.

To obtain a whole picture of the nonlinear optical properties of QDs, future works on sizes ranging from even more stronger confinement to very weak confinement are needed. On one hand, it is interesting to study the nonlinear optical properties on even smaller QDs where the effective mass approximation does not work. On the other hand the nonlinear optical properties for QDs in very weak confinement regime where the energy level spacing is approaching the thermal energy kT should also be investigated as a bridge between the weak-confined QDs and the bulk semiconductor.